
High precision transverse emittance measurement for novel plasma accelerators at the REGAE Linac

Dissertation

zur Erlangung des Doktorgrades
an der Fakultät für Mathematik, Informatik und Naturwissenschaften
Fachbereich Physik
der Universität Hamburg

vorgelegt von

Max Hachmann

aus Elmshorn

Hamburg

2017

Gutachter der Dissertation:

Dr. Ralph Aßmann
Prof. Dr. Florian Grüner

Zusammensetzung der Prüfungskommission:

Prof. Dr. Günter Sigl
Prof. Dr. Wolfgang Hillert
Dr. Ralph Aßmann
Prof. Dr. Florian Grüner
Dr. Klaus Flöttmann

Vorsitzende/r der Prüfungskommission:

Prof. Dr. Günter Sigl

Datum der Disputation:

3. November 2017

Vorsitzender Fach-Promotionsausschusses PHYSIK:

Prof. Dr. Wolfgang Hansen

Leiter des Fachbereichs PHYSIK:

Prof. Dr. Michael Potthoff

Dekan der Fakultät MIN:

Prof. Dr. Heinrich Graener

Abstract

The small 5 MeV linear accelerator REGAE at DESY produces ultra short and low charge electron bunches, on the one hand to resolve the excitation transitions of atoms temporally by pump-probe electron diffraction experiments and on the other hand to investigate principal mechanisms of laser plasma acceleration. In this context the external injection of the REGAE electron bunch as a probe of the generated plasma wakefield is planned. For both cases a high quality electron beam is required which can be identified with a small beam emittance. A standard magnet scan using a solenoid and a scintillator based detector system has been used for the emittance measurement which is in case of a low charge bunch most sensitive to the beam size determination (RMS or 2nd central moment of a distribution).

The detector system could be characterized and is adapted for transverse beam dynamics studies in terms of sensitivity and spatial resolution. E.g. the detector efficiency could be determined and a theoretical estimation be cross-checked.

To achieve precise and reliable results an image post-processing routine has been developed in order to deal with the noise contribution to the RMS determination. It could be made use of the nature of the noise to define profound noise cuts. As a result highly precise emittance measurements could be performed and the robust post-processing routine could be established.

The second topic of this work considers the assembling and characterization of permanent magnetic solenoids (PMS) for the external injection experiments in context of the upcoming laser plasma acceleration experiments. The demands on the electron beam in order to inject it in a matched manner asked for strong focusing magnets located close to the injection point into the plasma. A sorting algorithm for the piecewise composite PMS has been developed to maintain the field quality. In this context a simple field model and a field quality factor could be described and used for the sorting algorithm. The subsequent magnetic field measurement emphasizes the potential of the sorting algorithm and simultaneously confirms the simple field model. The whole procedure can be easily adapted to other types of permanent magnetic magnets.

Zusammenfassung

Der kleine 5 MeV linear Beschleuniger REGAE am DESY erzeugt ultra-kurze Elektronenpakete mit geringer Ladung, um einerseits die Anregung von Atomen zeitlich durch pump-probe Elektronenbeugung aufzulösen und andererseits prinzipielle Mechanismen der Laser-Plasma-Beschleunigung zu erforschen. In diesem Zusammenhang ist die externe Injektion eines REGAE-Elektronenpakets als Sonde des erzeugten Plasma-Kiefeldes geplant. Für beide Fälle ist eine hohe Elektronenstrahlqualität nötig, die sich durch eine kleine Strahlemittanz auszeichnet. Ein gewöhnlicher Magnetscan unter Zuhilfenahme eines Solenoiden und einem Detektorsystems basierend auf einem Szintillator wurde für die Emittanzmessung, die im Falle geringer Ladungen besonders sensitiv bezgl. der Bestimmung der Strahlgrößen ist (RMS oder zweites zentrales Moment einer Verteilung), genutzt.

Das Detektorsystem konnte charakterisiert werden und ist in puncto Sensitivität und räumlichen Auflösungsvermögens für Studien bzgl. der Strahldynamik geeignet. Z.B. konnte die Detektoreffizienz bestimmt und mit einer theoretischen Abschätzung verglichen werden.

Um präzise und verlässliche Ergebnisse zu erlangen, wurde eine Nachbearbeitungs-routine entwickelt, die den Rauschanteil bei der Bestimmung des RMS berücksichtigt. Es konnte die Natur des Rauschens genutzt werden, um fundierte Schnitte des Rauschanteils vorzunehmen. Dadurch konnten äußerst präzise Emittanzmessungen durchgeführt werden und die robuste Nachbearbeitungsroutine etabliert werden.

Das zweite Thema dieser Arbeit befasst sich mit dem Zusammensetzen und Charakterisieren von permanent magnetischen Solenoiden (PMS) für die Injektionsexperimente im Kontext der kommenden Laser-Plasma-Beschleunigungsexperimente. Die Anforderungen an den Elektronenstrahl, um ihn abgestimmt zu injizieren, verlangt nach stark fokussierenden Magneten, die sich nahe des Injektionspunktes in das Plasma befinden müssen. Ein Sortieralgorithmus für die stückweise zusammengesetzten PMS wurde entwickelt, um die Feldqualität zu gewährleisten. In diesem Zusammenhang wurde ein einfaches Feldmodell und ein Qualitätsfaktor des Feldes eingeführt und für den Sortieralgorithmus genutzt. Die darauf folgende Magnetfeldmessung betont das Potential des Sortieralgorithmus und bestätigt gleichzeitig das Feldmodell. Die gesamte Prozedur kann einfach auf andere Arten von permanent magnetischen Magneten angewandt werden.

Contents

Abstract	iii
Contents	vi
1 Introduction	1
1.1 Relativistic Electron Gun for Atomic Exploration (REGAE)	3
1.2 The LAOLA Experiment at REGAE	9
2 Fundamental considerations	13
2.1 Basics of beam characterization and dynamics	13
2.1.1 Full 6-dimensional phase space and its subspaces	14
2.1.2 Beam dynamics and optics	17
2.1.3 RMS emittance conservation	24
2.1.4 Emittance measurement via a magnet scan	26
2.2 Scintillator based particle detectors	27
2.2.1 Scintillators	27
2.2.2 CCD based image sensors	30
2.3 Laser Plasma Acceleration (LPA)	31
3 Transverse beam diagnostic for ultra-low bunch charges at REGAE	35
3.1 Detector system (D1) at REGAE	36
3.1.1 Andor iXon3 EMCCD cameras	37
3.1.2 Hamamatsu Fiber Optic Scintillator (FOS)	41
3.1.3 REGAE detector system efficiency	46
3.2 Image post-processing	50
3.2.1 Theoretical description of noise	52
3.2.2 Estimation of RMS error due to intensity cuts	58
3.2.3 Beam halo at the REGAE detector D1	64
3.3 Investigation of beam halo	67
3.3.1 Beam based investigations	68

Contents

3.3.2	FOS investigations in the laboratory	72
3.3.3	EGS5 simulations	76
3.3.4	Conclusion	91
4	Development of an electron beam optics for the external injection experiment at REGAE	93
4.1	Permanent Magnetic Solenoids	94
4.1.1	Design	94
4.1.2	Field description and sorting algorithm	96
4.1.3	Field measurement	103
4.2	ASTRA simulations of the external injection into a plasma wakefield	110
4.2.1	Adiabatic matching of an electron bunch into a laser plasma wakefield	110
4.2.2	Electron optics to focus into a plasma wakefield at REGAE .	113
5	Transverse Emittance Measurements and Simulations of a low charge electron bunch at REGAE	119
5.1	Emittance measurements at REGAE	120
5.1.1	Standard measurement via a solenoid scan	120
5.1.2	Emittance measurements of a collimated electron beam . . .	123
5.2	Comparison of ASTRA simulations and an emittance measurement .	125
5.2.1	Machine setup	126
5.2.2	Beam transport	131
5.2.3	Magnet scan	135
5.3	Long-term observations	140
6	Conclusion and Outlook	145
	List of Figures	153
	List of Tables	163
	Bibliography	167
	Acknowledgments	178

1

Introduction

Laser Plasma Acceleration (LPA) is a novel and fast developing particle acceleration technique. The idea of laser-driven plasma oscillation has been published already in 1979 by T. Tajima and J. M. Dawson [1]. With the development of laser systems able to produce high energy and ultra short laser pulses, the field of LPA develops and field gradients up to 100 GV/m and higher could be achieved inside a plasma wakefield which is at least three order of magnitudes larger than the gradients of conventional radio-frequency (RF) cavities. Due to the potential of this new acceleration technique several applications are conceivable. Because conventional accelerators almost reached their limits in terms of maximum mean beam energy in a reasonable scales, a very ambitious goal or dream is a next generation particle collider driven by dozens laser wakefield stages [2, 3]. Despite the high field gradients the compactness of this concept is a great feature. For this reason the major goal of the LAOLA¹ cooperation at DESY² is the realization of a table-top free electron laser [4] as part of the LUX project.

The LPA experiments at REGAE³ [5, 6] imbedded as well in the LAOLA cooperation have the goal to inject a well known and controlled electron bunch into a laser driven plasma wakefield. Most experiments are using a self-injection scheme to inject charged particles and subsequently accelerate them. A major breakthrough has been achieved in 2004 [7–9]. The former broad energy spectra of wakefield

¹**LAOLA: Laboratory for Laser- and beam-driven plasma Acceleration**

²**DESY: Deutsches Elektronen-Synchrotron**

³**REGAE: Relativistic Electron Gun for Atomic Exploration**

accelerated electrons could be reduced to a few percent. But still, the injection process relies on statistical scattering of electrons inside the acceleration region of the plasma wake. From such electrons it is difficult to gain information about the exact acceleration process and the shape of the fields. Therefore the externally injected electron bunch shall function as a probe of the wakefield. Diagnosing the injected electron bunch after passing the wakefield offers the opportunity to gain information about the plasma wakefields. Furthermore, from a scan of the wakefield phases a map of the wakefield can be obtained. The injection as well as the experimental implementation of the plasma experiment at REGAE is described in [10]. Further experiments are conceivable and has been proposed. For example the realization of a longitudinal phase space diagnostic [11] where the off-axis transverse electric fields inside a wakefield can be used to streak an electron bunch that consequently maps the longitudinal information to a change of the transverse position. This technique known from conventional beam diagnostic [12] serves the needs of a beam diagnostic for ultra short pulses down to the sub-fs bunch length range.

Within the scope of this work the focus lies on the preparatory studies of the electron probe generated and accelerated by the REGAE accelerator. The goal is the preparation and performance of transverse emittance measurements. The probe for the LPA experiments has to be fully characterized to gain as precise information as possible from the reconstruction of the wakefields. The emittance as a quantity of the beam quality can be used to comprehend the changes of the phase space of the electron bunch during the LPA.

The used method is well known but the circumstances makes it still challenging. On the one side all measurements have been performed for a low-charge electron beam with a high precision and reliability. Technically the diagnostic of a low-charge beam was the most challenging problem. Charges from some hundreds down to a few fC are not usual for common accelerator applications. But for the experiments conducted at the small electron accelerator REGAE they are necessary. The DESY internally compounded detector (see Sec. 3.1) made from commercial accessible components meets all expectations and it enables to resolve even electron distributions of sub 10 fC.

On the other side the method of emittance measurement requires from its theory RMS beam sizes as an input. The experimental determination of the RMS beam size of arbitrary distributions is often assumed to be inconvenient and complicated.

It will be shown that a profound routine based on theoretical description of the disturbances like noise can be formulated and integrated into normal machine operation. The routine proved its reliability in over 100 emittance measurements for quite different machine settings at REGAE.

How to achieve these results and how to overcome the challenges will be presented in this work. It has to be seen in context of the planned experiments at REGAE incorporated in the LAOLA collaboration and is a move towards the realization of its scientific ambitions.

In the following sections of this chapter the linear accelerator (*linac*) REGAE is introduced in detail as well as a short introduction to the planned beamline upgrade for the plasma wakefield experiments is given.

1.1 Relativistic Electron Gun for Atomic Exploration (REGAE)

The Relativistic Electron Gun for Atomic Exploration (REGAE, Fig. 1.1,1.2) at DESY is a small 5 MeV linear accelerator with a bunch charge range of a few to some hundred fC. The beam energy is delivered by a 1.6-cell S-band photo-injector cavity, called *gun*. A Ti-sapphire laser generates electrons from different type of metal cathodes like Molybdenum (Mo) or Gold (Au) and other materials like cesium-telluride (CsTe). The installed cathode is pumped by UV light with a wavelength of 233 nm. In addition to the gun a 4-cell buncher cavity is part of the injector section of REGAE. It is designed for ballistic bunching down to 10 fs [10, 13]. Both cavities are normal conducting, water cooled and fed by *one* klystron. The phases and amplitudes of both cavities can be adjusted with a mechanical phase shifter integrated in the wave guide system. Besides the fs-short electron bunches the beam arrival jitter [14] has to be of the same order as the bunch length, meaning 10 fs. This requires a stable RF system and in addition a stable laser to RF synchronization [15]. Due to the low energy a beam optics consisting of compact, symmetrically focusing solenoids is sufficient. The beam can be transversely adjusted with beam steerers [16]. To measure the beam energy a dipole spectrometer is integrated. It bends the electron beam by 90° and images it on a beam monitor which can be used to determine the mean beam energy and

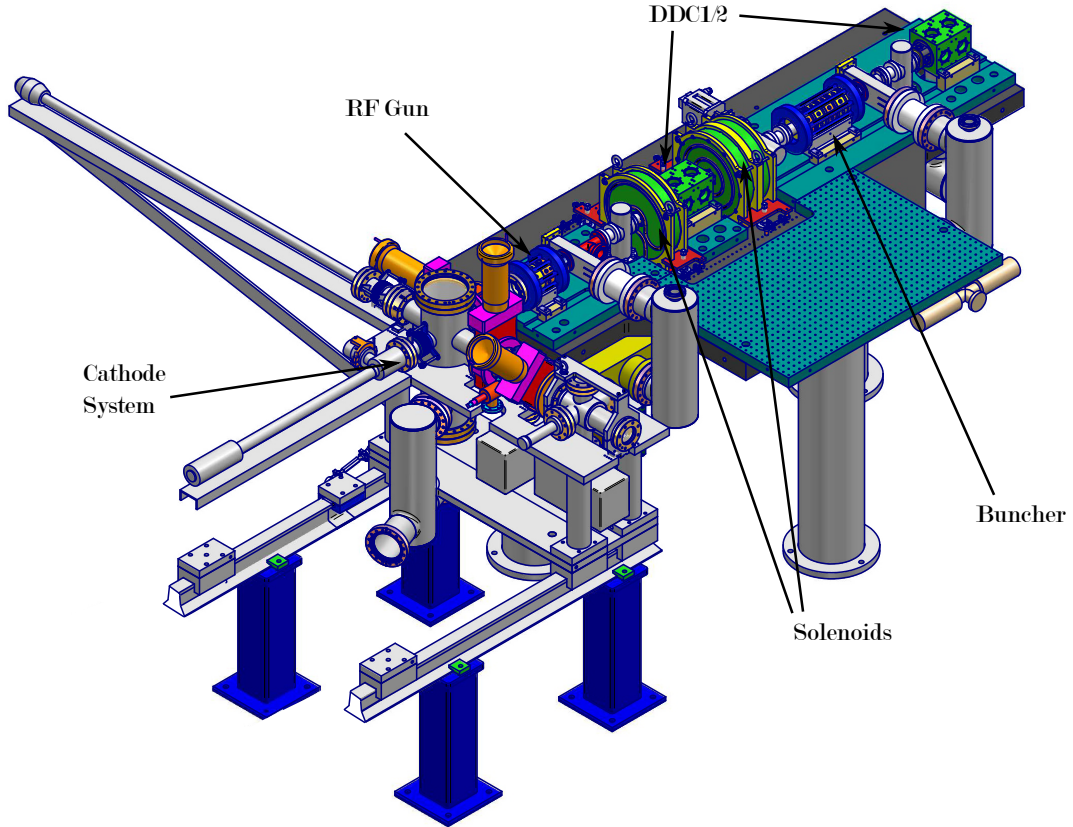


Figure 1.1: Illustration of the injector part of the REGAE accelerator including the cavities (gun, buncher), beam optics, the diagnostic crosses (DDC1/2) and the cathode load-lock system.

energy spread. Furthermore there are two more so called *double diagnostic crosses* (DDC1/2). Each includes a transverse beam monitor, realized with scintillators and CCD cameras (an image intensifier is optional) [17–19] and a Faraday cup to measure the bunch charge [20]. In addition to the irreversible charge measurement with the Faraday cups a non-destructively diagnostic device called *Dark current Monitor* (DaMon) [21] is installed. Because the measurement of low charge diffraction pattern is difficult a detector system with a high sensitivity and a sufficient spatial resolution has been developed (Sec. 3.1) and is located at the very end of the beamline.

The machine is built for two types of experiments: first a time-resolved electron diffraction experiment in order to make atomic transitions 'visible' [22–24] and secondly investigations of new plasma-wakefield acceleration schemes [10, 25]. Both

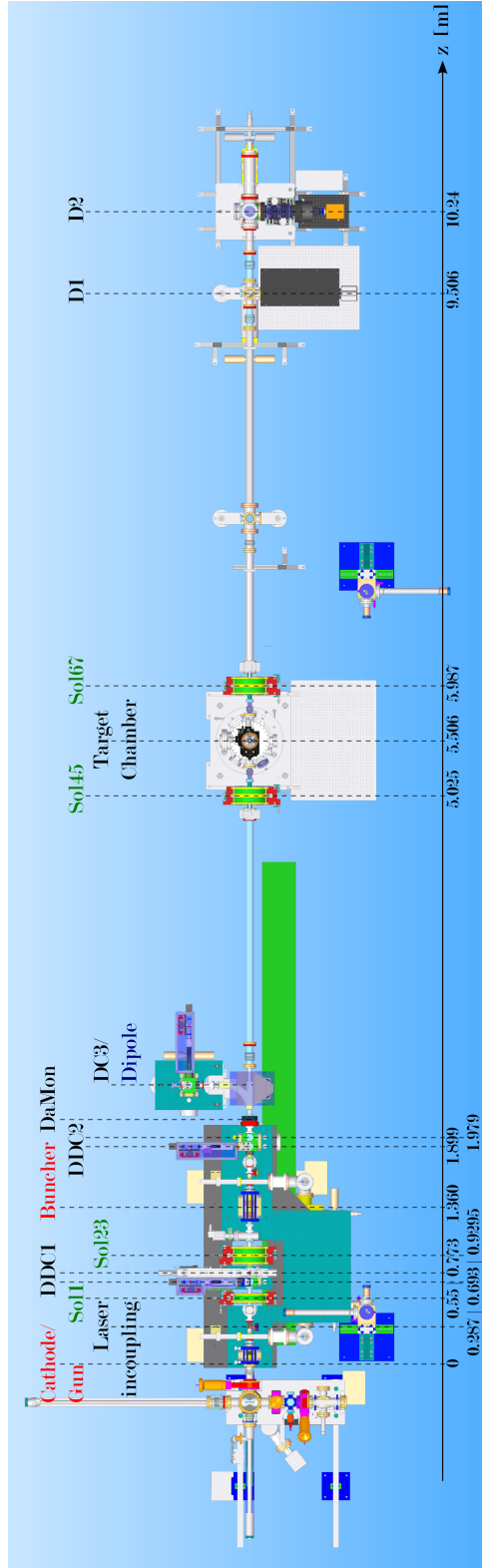


Figure 1.2: Illustration of the current REGAE beamline including all relevant machine devices. The center positions of each device along the beamline are depicted as well. **Sol:** Solenoid, **DC:** Diagnostic Cross, **DDC:** Double Diagnostic Cross, **D:** Detector system, **DaMon:** Dark current Monitor.

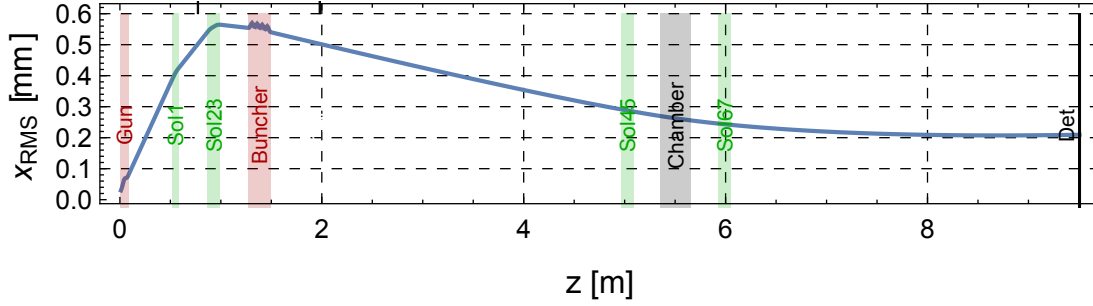
experiments require a low transverse beam emittance down to 10π nmrad (normalized emittance). Hence, there are two challenges: generate such a high quality and low-charge electron bunch and measure its quantities with high precision.

The design machine and beam parameters are presented in the following *design run* - simulated with ASTRA⁴ [26]. The most important machine, cathode laser and beam parameters are listed in Tab. 1.1. The tracked electron beam is shown in Fig. 1.3. Only the horizontal and longitudinal directions are shown. Due to the symmetrical beam optics and identical laser pulse parameters in both transverse directions only the horizontal direction is depicted without any loss of generality. The beam optics is mainly realized with so called 'double' solenoids (see Sec. 2.1.2), only the first solenoid is a 'single' or ordinary solenoid which indeed introduces a net rotation to the electron beam. But due to the symmetric beam a visible effect cannot be recognized during the beam tracking. The first solenoid Sol1 is placed right behind the gun to 'capture' the divergent electron beam from the gun cavity and reduces its spatial growth. Because solenoids have principally a non-linear field, the assumption of a linear field only holds in the vicinity of the longitudinal field axis. Therefore the preferred setup of the beam optics is to keep the beam size especially at position of the solenoids small (see Fig. 1.3, **a**). The transverse emittance stays almost constant from the gun to the exit of the buncher cavity. After passing it the beam is focused in the transverse as well as in the longitudinal directions. This causes space charge forces which, due to their non-linear nature, increases the transverse emittance. Especially the longitudinal focus forces this emittance growth. Therefore, after the longitudinal focus the transverse emittance growth stops again. The emittance at position of the target (target for diffraction experiments as well as the LPA experiments) is still pretty small. The transverse as well as the longitudinal emittance are already defined by the laser pulse parameters right at the photo cathode. During the electron transport the emittance is only growing. For the *design run* the laser parameters have been optimized in terms of laser spot size and length at the cathode. A smaller laser spot yields in principle a smaller transverse emittance but at some point the space charge forces are too large and counteract the shrinking emittance and consequently the emittance starts to grow again.

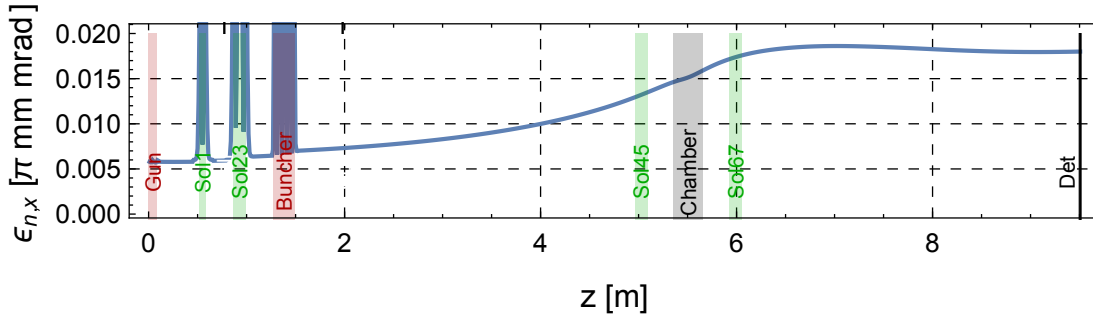
The longitudinal focusing is induced by the buncher cavity. Due to the ballistic bunching [13] the bunch can be focused down to less than 10 fs. It reaches

⁴ASTRA: **A** Space Charge **T**racking **A**lgorithm

a)



b)



c)

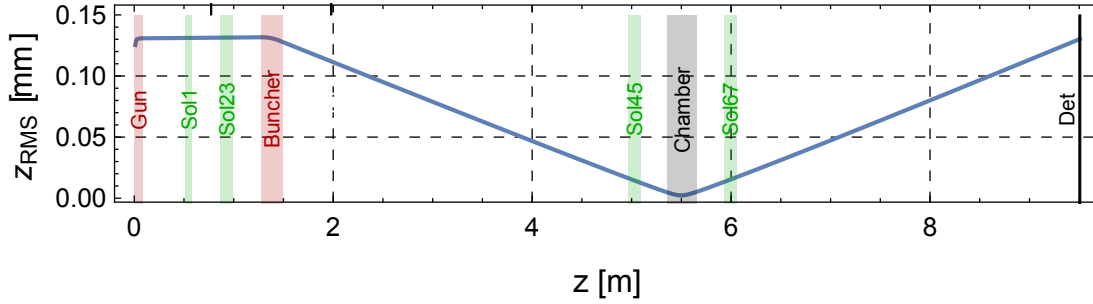


Figure 1.3: Tracking different beam parameters from the cathode to the detector *Det*: a) RMS beam size, b) norm. RMS emittance, c) RMS bunch length. The horizontal direction is plotted representatively. The various beam optics relevant elements are indicated by colored blocks. Cavities are *red*, solenoids are *green* and collimators are *black*. Their width is correctly scaled to the real objects dimension.

the minimal bunch length at the position of the target. Higher order field effects prevent an even shorter electron bunch. But there exists methods to reduce the bunch length to a sub-fs level. An almost common method is the correction of the higher field components imprinted in the longitudinal phase space with a higher harmonic cavity. Proposed for REGAE by K. Flöttmann in [27]. A more sophisticated method has been proposed and published by B. Zeitler in [10, 13]. This concept copes without any additional higher harmonic cavity. Just the right adjustment of the phases and amplitudes of the existing cavities is needed to correct the higher order phase space curvature and to achieve a sub-fs bunch length. The *design run* is the reference for the performed emittance measurements.

Table 1.1: Relevant design parameters for the REGAE accelerator including machine, laser and electron beam parameters. All parameters are extracted from the REGAE *design run*. The laser parameters are given at the photo cathode. The electron beam parameters are given at the target position at $z = 5.5$ m.

Parameter	Value
Gun gradient	$\text{Amp}_{\text{Gun}} = 110 \text{ MV/m}$
Buncher gradient	$\text{Amp}_{\text{Bun}} = 25 \text{ MV/m}$
Laser wave length	$\lambda = 233 \text{ nm}$
Laser focus size	$r_{\text{RMS}} = 7 \text{ }\mu\text{m}$
Laser pulse length	$t_{\text{RMS}} = 0.5 \text{ ps}$
Kin. energy	$E_{\text{kin}} = 5.1 \text{ MeV}$
Lorentz factor	$\gamma = 11.0$
Bunch charge	$Q \simeq 10 \text{ fC to } 500 \text{ fC}$
Norm. emittance	$\epsilon_{n,x} = 0.015 \pi \text{ mm mrad}$
Min. bunch length	$z_{\text{RMS}} = 2.3 \text{ }\mu\text{m} \hat{=} 7.7 \text{ fs}$

1.2 The LAOLA Experiment at REGAE

To realize the LPA experiments at REGAE the beamline needs to be redesigned extensively. Only the injector section (illustrated in Fig. 1.1), stays untouched. A schematic illustration is shown in Fig. 1.4. The high power laser, called ANGUS, is coupled in closely behind the buncher cavity. The electron bunch needs to pass the holey incoupling mirror. The electron beam and laser pulse are co-propagating from there on. Due to the huge gas load, generated by the gas target, a differential pumping section is integrated. The aperture of the beamline is shrinking towards the new target chamber bit by bit. The standard REGAE beam optics are almost untouched just slightly shifted in position and it is extended by a quadrupole doublet to adapt to higher mean beam energies. The doublet is located around Sol67 as close as possible to the target chamber. Not visible at Fig. 1.4 is a *transverse deflecting structure* (TDS) [12] which is directly located behind the target chamber. It will be used to image the longitudinal phase space distribution of the electron bunch. The main change in comparison to the actual REGAE setup is the shift of the dipole spectrometer to a place behind the target chamber. It is obviously necessary to measure the beam energy and energy spread of the outcoupled electron beam from the plasma wakefield. For the outcoupling of the high power laser is again a holey mirror installed. The electron bunch has to pass this mirror to reach the dipole spectrometer and further beam diagnostics.

The injection of a REGAE electron beam into the plasma wakefield requires another update of the transverse beam optics. As shown later on really small beta functions are required at the injection point. In order to realize this in-vacuum permanent magnetic solenoids (PMS) have been designed [28] and assembled to reach the demands of the experiment. The required beta function at the injection point is on the range of 10 mm. This is even challenging at REGAE with its small transverse emittance. But it will be shown that this is feasible with the new beam optics. The PMS are located inside the new target chamber on highly precise movers to achieve a μm alignment precision. The PMS are introduced in detail in Sec. 4.1.

The whole experiment relies on a pretty crucial property, namely the stability. Stability means in this context every kind of stability, including the synchronization of the REGAE accelerator and the high power laser ANGUS but as well the pointing stability of both sources. The required stability of each system is already pretty challenging in addition these two systems, located in different buildings, has to

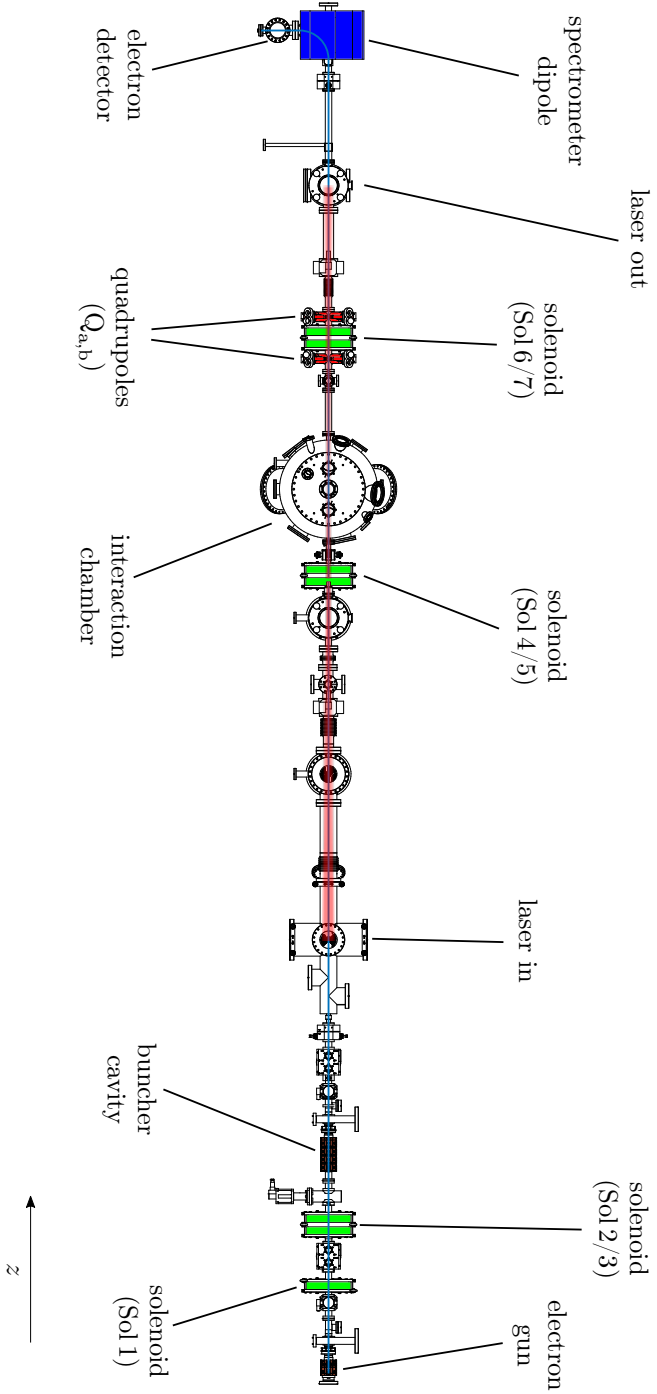


Figure 1.4: Overview of the REGAE beamline adapted to the LPA experiment. Up to the buncher cavity the beamline is unchanged. Sol45 is slightly shifted upstream and Sol67 a bit further downstream. The *interaction chamber* is new and houses beside the new gas target for the LPA experiment new beam optics devices - the permanent magnetic solenoids (PMS). In addition to the conventional solenoids a quadrupole doublet will be installed to cope with higher energy electrons accelerated during the LPA process. The dipole spectrometer is shifted from its original place, close behind the buncher, to the end of the LAOLA@REGAE beamline section. The in- as well as out-coupling of the high power ANGUS laser is depicted as well. (Figure by courtesy of B. Zeitler, from [10])

be synchronized. M. Titberidze developed a unique synchronization setup for this experiment [29] which meets the required specifications. The mechanisms of the LPA are introduced in Sec. 2.3 and the injection process is described in Sec. 4.2. It includes the analytical description of the beam dynamics inside the plasma as well as the merging of the analytical plasma model and an ASTRA simulation of REGAE.

2

Fundamental considerations

The intention of this chapter is the introduction of required fundamentals for this work. It starts with a basic introduction of beam dynamics and the description of particle bunches. It is the base of the later presented emittance measurements but also of the sophisticated image post-processing routine and the associated studies. In order to achieve highly precise emittance measurements an outstanding detector system is needed. The basic components and their functionality are introduced and explained. The last section is dedicated to the plasma wakefield acceleration and its principal mechanisms. The acceleration and focusing scheme is revealed and analytically described.

2.1 Basics of beam characterization and dynamics

To characterize particle distributions as well as their motion an adequate formalism and theory is needed. This section is geared to [30, 31] and intended to give a short overview of the analytical tools which are required to describe as well as to manipulate the transverse phase-space of charged particle distributions. Especially, the characterization of particle distributions is of particular interest for this work. The emittance as an invariant of the motion and a measure of the beam quality is a necessary quantity to describe the beam motion. Because it cannot be measured directly a common method for an indirect measurement is introduced. All required steps to provide such a method will be introduced. Not every step is presented

in all details but all necessary concepts are illustrated. One important matter of fact to theoretically describe charged particle ensembles is emphasized over and over again. The presented theory holds for RMS beam quantities. Beside the introduction of the RMS or 2nd central moment, it will be shown that it is the RMS emittance which is an invariant of the motion.

2.1.1 Full 6-dimensional phase space and its subspaces

Speaking about the emittance of an arbitrary particle distribution often the normalized two-dimensional transverse RMS emittance in Cartesian coordinates is meant. This can be helpful and instructive in most cases but it does not show the complete picture.

In order to motivate the necessity to describe the full phase space volume called emittance it is helpful to start with a single particle and then generalize for a whole particle ensemble. The motion of a single particle can be fully described if its position and velocity components are known at one point in time. In Cartesian coordinates these six parameters can be combined to one vector

$$\mathbf{X}^T = \left(x \quad p_x \quad y \quad p_y \quad \delta z \quad \delta p_z \right), \quad (2.1)$$

where x , y and δz are the horizontal, vertical and longitudinal position and p_x , p_y and δp_z the corresponding momenta. The main direction of motion shall be z without any loss of generality. The δ of the longitudinal components δz and δp_z indicates a relative position or momentum with respect to a co-moving position z or a reference momentum p_z , respectively. \mathbf{X} defines the phase space where a particle exists and later on the whole ensemble.

To characterize an ensemble of particles with an arbitrary distribution it is necessary to describe the motion of the whole ensemble with quantities which are related to the complete ensemble and not to its individual particles. For this purpose the 1st moment and 2nd central moment of an particle ensemble are introduced. Assuming N particles forming a 'bunch' where every particle can be described by a vector \mathbf{X}_i (Eq. 2.1) with $i = 1, \dots, N$. The first and second central moment of each component of \mathbf{X} is denoted by $\langle \rangle$. The 1st moment describes the expected value of the distribution whereas the 2nd central moment its spread. The distribution is defined in a co-moving frame which travels along the longitudinal direction. The reference position and momentum are defined as the average longitudinal bunch position $\langle z \rangle$ and the average longitudinal momentum $\langle p_z \rangle$ which are equal to the

former mentioned position z and momentum p_z . The square root of the 2nd central moment is also called *root-mean square* (RMS). For a continuous 2-dimensional distribution $\rho(x, y)$ the 2nd moment in x -direction is defined as

$$\langle x^2 \rangle = \frac{\int x^2 \rho(x, y) dx dy}{\int \rho(x, y) dx dy} - \left(\frac{\int x \rho(x, y) dx dy}{\int \rho(x, y) dx dy} \right)^2 \quad (2.2)$$

and consequently $\sqrt{\langle x^2 \rangle} = x_{\text{RMS}}$. Furthermore, it can be defined for a discrete distribution, often given by a pixel detector device, as well

$$\langle x^2 \rangle = \frac{\sum_{i=1}^N x_i^2}{N} - \left(\frac{\sum_{i=1}^N x_i}{N} \right)^2. \quad (2.3)$$

The second term in Eq. 2.2 as well as in Eq. 2.3 is the square of the first moment of the ensemble and 'centers' the calculation of the 2nd moment to its barycenter. Here, the 2nd moment of the position is exemplarily shown. In addition to the moments the correlation between two variables like x and p_x can be expressed in a similar way:

$$\langle xp_x \rangle = \frac{\sum_{i=1}^N x_i p_{x,i}}{N} - \frac{\sum_{i=1}^N x_i}{N} \frac{\sum_{i=1}^N p_{x,i}}{N}. \quad (2.4)$$

Later on the validity of using the central moments to describe the dynamics of an ensemble in the environment of an accelerator will be shown.

On the basis of *Liouville's theorem* [32] it can be shown that the phase space volume dV occupied by N particles in phase space is a constant of motion

$$\frac{dV}{dt} = 0, \quad (2.5)$$

as long as particle-particle interactions are excluded and a Hamiltonian system underlies the motion. The phase space volume is directly proportional to the RMS *emittance* as long as only linear transformations are applied to the particle distribution. In this sense the usage of the RMS restricts Liouville's theorem even more. The emittance is defined by means of the Σ -*matrix* (or *beam matrix*) and the central moments of the particle distribution as follows:

$$\Sigma = \begin{pmatrix} \langle x^2 \rangle & \langle xp_x \rangle & \langle xy \rangle & \langle xp_y \rangle & \langle x \delta z \rangle & \langle x \delta p_z \rangle \\ \langle p_x x \rangle & \langle p_x^2 \rangle & \langle p_x y \rangle & \langle p_x p_y \rangle & \langle p_x \delta z \rangle & \langle p_x \delta p_z \rangle \\ \langle y x \rangle & \langle y p_x \rangle & \langle y^2 \rangle & \langle y p_y \rangle & \langle y \delta z \rangle & \langle y \delta p_z \rangle \\ \langle p_y x \rangle & \langle p_y p_x \rangle & \langle p_y y \rangle & \langle p_y^2 \rangle & \langle p_y \delta z \rangle & \langle p_y \delta p_z \rangle \\ \langle \delta z x \rangle & \langle \delta z p_x \rangle & \langle \delta z y \rangle & \langle \delta z p_y \rangle & \langle \delta z^2 \rangle & \langle \delta z \delta p_z \rangle \\ \langle \delta p_z x \rangle & \langle \delta p_z p_x \rangle & \langle \delta p_z y \rangle & \langle \delta p_z p_y \rangle & \langle \delta p_z \delta z \rangle & \langle \delta p_z^2 \rangle \end{pmatrix} \quad (2.6)$$

where every element is defined as

$$\Sigma_{jk} = \langle \mathbf{x}_j \mathbf{x}_k \rangle \quad \text{with } j, k = 1, \dots, 6. \quad (2.7)$$

Furthermore, it is important to notice that $\Sigma_{jk} = \Sigma_{kj}$. The normalized 6D emittance ϵ_{6D} is defined by the determinant of the Σ -matrix:

$$\epsilon_{n,6D} = \frac{1}{(m_0 c)^3} \sqrt{\det \Sigma}. \quad (2.8)$$

If there is no coupling between the different transverse as well as longitudinal planes, which is a good assumption for most accelerator sections, the Σ -matrix (Eq. 2.6) reduces to a block-diagonalized matrix, namely the dash-framed elements. All off-diagonal elements are consequently equal to zero. The determinant of each block on the other side describes the normalized emittance of the corresponding 2-dimensional plane:

$$\begin{aligned} \epsilon_{n,x} &= \frac{1}{m_0 c} \sqrt{\langle x^2 \rangle \langle p_x^2 \rangle - \langle x p_x \rangle^2}, \\ \epsilon_{n,y} &= \frac{1}{m_0 c} \sqrt{\langle y^2 \rangle \langle p_y^2 \rangle - \langle y p_y \rangle^2}, \\ \epsilon_{n,z} &= \frac{1}{m_0 c} \sqrt{\langle \delta z^2 \rangle \langle \delta p_z^2 \rangle - \langle \delta z \delta p_z \rangle^2}. \end{aligned} \quad (2.9)$$

Here, exemplarily for all other directions, the conversion into different expressions of the emittance is shown for the horizontal direction. From the normalized emittance the geometrical emittance ϵ_x can be derived

$$\epsilon_x = \frac{m_0 c}{\langle p_z \rangle} \epsilon_{n,x}. \quad (2.10)$$

Dragging the average longitudinal momentum $\langle p_z \rangle$ inside the square root the momenta can be replaced by the divergence x' :

$$x' = \frac{p_x}{\langle p_z \rangle}. \quad (2.11)$$

This is a good approximation as long as the energy spread is small. The found expression for the emittance is the often used *trace space emittance*

$$\epsilon_x = \sqrt{\langle x^2 \rangle \langle x'^2 \rangle - \langle x x' \rangle^2}. \quad (2.12)$$

At this point it is important to emphasize again that the different expressions of the emittance are all RMS emittances but only the normalized emittance is a constant of the ensemble motion.

Often the 2nd central moments (e.g. $\langle x^2 \rangle$ or $\langle x'^2 \rangle$) are replaced by the standard deviations of a Gaussian distribution. Indeed, the handling of a Gaussian distribution is more comfortable but from a theoretical point of view it is not required and all statements which have been done and will be done in the following concerning the calculation and measurement methods for the emittance are valid for arbitrary particle distributions. A Gaussian distribution is not a fundamental assumption which is required for the description of a particle ensemble and its motion. The more general description is obtained by RMS quantities. All issues concerning the calculation of the RMS beam size are described and discussed in detail in Sec. 3.2. In addition to the 2-dimensional emittances the 4-dimensional transverse emittance will be of interest. It is equal to the determinant of the 4×4 sub-matrix containing the transverse elements of the Σ -matrix in Eq. 2.6:

$$\Sigma_{4D} = \begin{pmatrix} \langle x^2 \rangle & \langle x p_x \rangle & \langle x y \rangle & \langle x p_y \rangle \\ \langle p_x x \rangle & \langle p_x^2 \rangle & \langle p_x y \rangle & \langle p_x p_y \rangle \\ \langle y x \rangle & \langle y p_x \rangle & \langle y^2 \rangle & \langle y p_y \rangle \\ \langle p_y x \rangle & \langle p_y p_x \rangle & \langle p_y y \rangle & \langle p_y^2 \rangle \end{pmatrix},$$

$$\epsilon_{4D} = \frac{1}{(m_0 c)^2} \sqrt{\det \Sigma_{4D}}. \quad (2.13)$$

2.1.2 Beam dynamics and optics

The particle transport in an accelerator can be described analytically. This section will introduce the basics of linear beam optics as well as the solenoid as a beam focusing device in detail due to its importance for the beam optics at REGAE.

Matrix formalism

At this point only a short introduction and overview of linear beam optics will be given. It is geared to [33, 34]. Furthermore, because REGAE is a *linear accelerator* (linac) with no regular dispersive elements and only a small energy spread, effects like chromaticity will be neglected. The equation of motion of a charged particle, only influenced by linear fields or freely drifting, which moves along the longitudinal

coordinate z , is a second-order linear ordinary differential equation

$$x'' + K(z)x = 0, \quad (2.14)$$

where $K(z)$ e.g. is the focusing strength of magnets. $K(z)$ is equal to zero for any drift section. x'' is the second derivative of the horizontal coordinate with respect to z . The solution is a linear combination of independent *cosine*- and *sine*-like solutions

$$x(z) = x_0 C(z) + x_0' S(z). \quad (2.15)$$

This equation can be expressed as a linear transformation

$$\mathbf{X} = \begin{pmatrix} C(z) & S(z) \\ C'(z) & S'(z) \end{pmatrix} \cdot \mathbf{X}_0, \quad (2.16)$$

where the matrix is called *transfer matrix* \mathbf{M} and \mathbf{X} and \mathbf{X}_0 are the particle's properties - the position x and divergence x' with respect to the longitudinal axis z :

$$\mathbf{X}^\top = \begin{pmatrix} x & x' \end{pmatrix}. \quad (2.17)$$

A general solution for the transfer matrix \mathbf{M} can be found.

$$\mathbf{M}(z) = \begin{pmatrix} \cos(\sqrt{K(z)}z) & \frac{1}{\sqrt{K(z)}} \sin(\sqrt{K(z)}z) \\ -\sqrt{K(z)} \sin(\sqrt{K(z)}z) & \cos(\sqrt{K(z)}z) \end{pmatrix}. \quad (2.18)$$

There are some useful examples for transfer matrices of special devices or sections. For a simple drift the focal strength is zero and the transfer matrix simplifies to

$$\mathbf{M}_D = \begin{pmatrix} 1 & l \\ 0 & 1 \end{pmatrix}, \quad (2.19)$$

using the small-angle approximation and l as the drift distance. Another important and useful approximation mainly for high energy particles, is the *thin lens* approximation for magnets. If the focal length f is much longer than the magnet's length l , the particle position inside a magnet is approximately constant and the

matrix element M_{12} can be assumed to be zero and z tends to zero. Applying these assumptions to Eq. 2.18 yields

$$\begin{aligned} \mathbf{M}_{\text{tl}} &= \begin{pmatrix} 1 & 0 \\ -Kl & 1 \end{pmatrix} \\ &= \begin{pmatrix} 1 & 0 \\ -1/f & 1 \end{pmatrix}, \end{aligned} \quad (2.20)$$

where the small-angle approximation has been applied at first to M_{21} and afterwards $-Kl$ has been replaced by the focal length $-1/f$.

To fulfill the conservation of the phase space area it is necessary that all transfer matrices satisfy

$$\det \mathbf{M} = 1. \quad (2.21)$$

The matrix formalism is distinctly separating the beam optics, represented by the transfer matrix, and the initial and final beam parameters \mathbf{X}_0 and \mathbf{X} . As long as the beam optics is known a transfer matrix can be formulated and the evolution of an arbitrary particle distribution can be calculated at every position along the transfer beamline.

Using the matrix formalism and the trivial transformations (see [35, 36])

$$(x_{\text{RMS}})' = \frac{\delta}{\delta z} \langle x^2 \rangle^{1/2} = \frac{\langle xx' \rangle}{\langle x^2 \rangle^{1/2}} \Rightarrow \langle xx' \rangle = x_{\text{RMS}} (x_{\text{RMS}})'$$

and

$$\epsilon_x = \sqrt{\langle x^2 \rangle \langle x'^2 \rangle - \langle xx' \rangle^2} \Rightarrow \langle x'^2 \rangle = \frac{\epsilon_x^2}{x_{\text{RMS}}^2} + (x_{\text{RMS}})'^2,$$

it is possible to analytically describe the evolution of the beam size along a transfer line. The so found *envelope equation* can be written as

$$x_{\text{RMS}}^2(z) = \begin{pmatrix} M_{11}^2 & 2 M_{11} M_{12} & M_{12}^2 \end{pmatrix}^\top \begin{pmatrix} a_1 \\ a_2 \\ a_3 \end{pmatrix} \quad (2.22)$$

$$\begin{aligned} \text{with } a_1 &= x_{0,\text{RMS}}^2, \\ a_2 &= x_{0,\text{RMS}}(x_{0,\text{RMS}})', \\ a_3 &= \frac{\epsilon_x^2}{x_{0,\text{RMS}}^2} + (x_{0,\text{RMS}})'^2, \end{aligned}$$

where $x_{0,\text{RMS}}$ and $(x_{0,\text{RMS}})'$ denote the initial beam conditions. $(x_{\text{RMS}})'$ is the derivative of the beam envelope and describes its slope.

Courant-Snyder invariant

Without going too much into details a different formulation of the invariant of the motion of a particle distribution will be introduced in this subsection. It follows the famous description of E. D. Courant and H. S. Snyder [37]. It is the common phrasing for circular accelerators or storage rings where it is really helpful and required. For linacs these formulations are valid as well but not necessarily required. In the following all statements are referred to ring accelerators. Speaking about ring accelerators it is common to switch from the longitudinal coordinate z to the orbit coordinate s . At the end of this section the made statements are put in the context of linacs.

The *Courant-Snyder invariant* is a different expression for the phase-space volume conservation and is defined as

$$\epsilon^2 = \gamma x^2 + \alpha x x' + \beta x'^2. \quad (2.23)$$

Because the emittance ϵ , here the *trace space emittance*, is a constant of motion, necessarily the right hand side of the equation has to be constant as well. In case the mean beam energy changes the Courant-Snyder invariant (Eq. 2.23) has to be scaled with the inverse *Lorentz factor* γ^{-1} to stay valid. Furthermore, the *optical functions* $(\beta(s), \alpha(s), \gamma(s))$ can be introduced. They are periodic and defined at each position s only by the beam optics of the accelerator. The evolution of the phase space is fully described if the beta functions are known. If the emittance is known as well, the full phase space at every position and revolution inside the ring accelerator is known. The transfer matrix \mathbf{M} can be formulated with help of the optical functions as:

$$\mathbf{M}(s) = \begin{pmatrix} 1 & 0 \\ 0 & 1 \end{pmatrix} \cos \mu + \begin{pmatrix} \alpha(s) & \beta(s) \\ -\gamma(s) & -\alpha(s) \end{pmatrix} \sin \mu, \quad (2.24)$$

which is called the *Courant-Snyder-Matrix*. Because \mathbf{M} has to fulfill Eq. 2.21 the optical functions have to satisfy $\beta\gamma - \alpha^2 = 1$. μ is a phase function and independent of s . Nevertheless the phase difference between two positions s_0 and s_1 inside the

ring accelerator is called *phase advance* Φ and is defined as:

$$\Phi = \int_{s_0}^{s_1} \frac{1}{\beta(s)} ds. \quad (2.25)$$

A change of the phase advance between these two positions means a change of the transfer matrix itself between these two positions.

In case of a linac the particles move along the beam line only ones and the optical functions are not periodical anymore. But they are still valid as long as the initial optical functions are known.

Furthermore the phase space area can be described by the optical functions as an ellipse whose area is proportional to the emittance. Fig. 2.1 illustrates how the phase space ellipse is connected with the 2nd moment of the particle distribution as well as the optical functions. Summarized the optical functions can be obtained from the beam matrix (Eq. 2.6, horizontal sub-phase-space) and the emittance as follows:

$$\Sigma_{\mathbf{x}} = \begin{pmatrix} \langle x^2 \rangle & \langle xx' \rangle \\ \langle xx' \rangle & \langle x'^2 \rangle \end{pmatrix} = \epsilon_x \begin{pmatrix} \beta_x & -\alpha_x \\ -\alpha_x & \gamma \end{pmatrix}. \quad (2.26)$$

In addition α and γ can be expressed by β as

$$\begin{aligned} \alpha &= -\frac{\beta'}{2}, \\ \gamma &= \frac{1 + \alpha^2}{\beta}. \end{aligned} \quad (2.27)$$

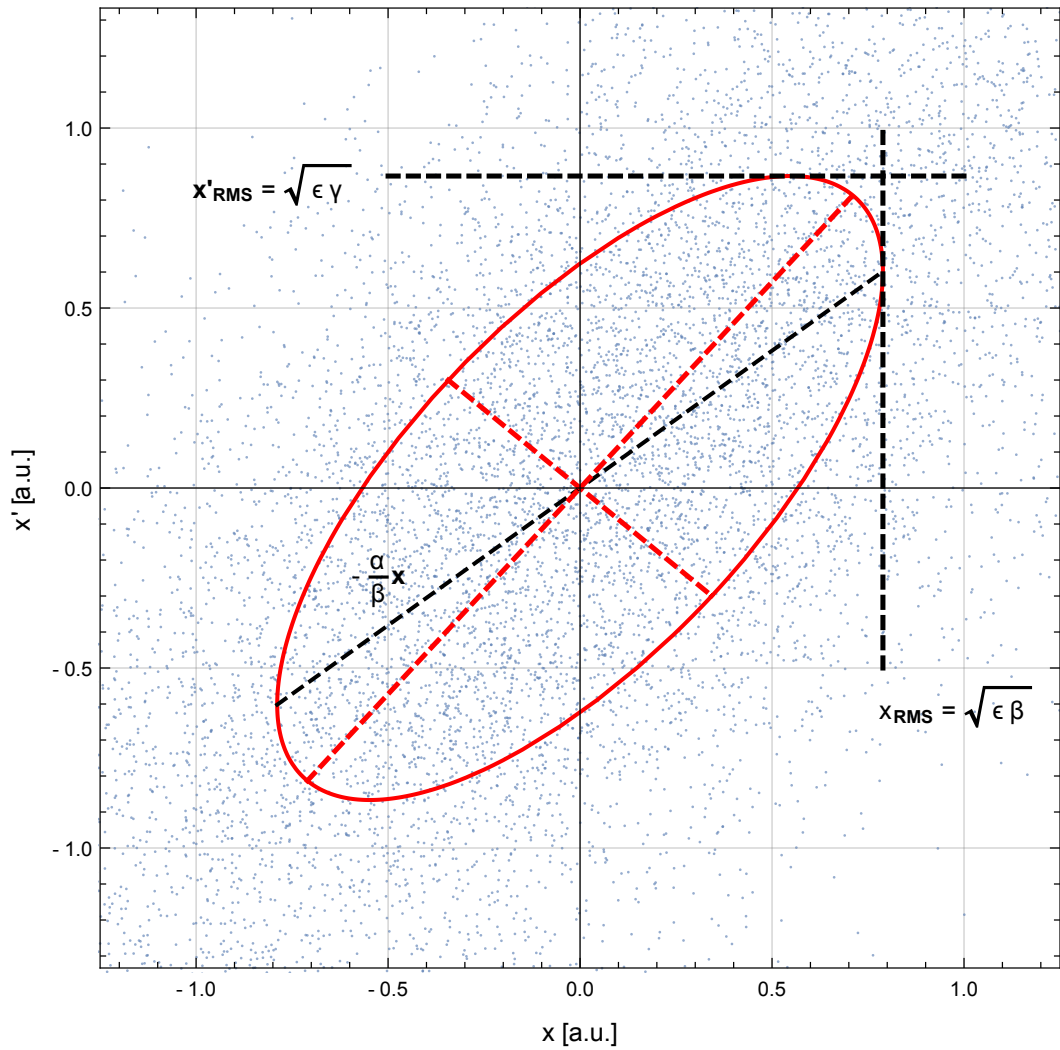


Figure 2.1: Schematic phase space ellipse and illustration of the related beam parameters and optical functions, respectively. The particle distribution is depicted by the blue dots.

Characterization of the magnetic field of a solenoid

This section is meant to recap the characteristics of the magnetic field of a solenoid magnet which has been described in [35, 36, 38]. First of all, the rotationally

symmetric field of a solenoid can be expanded in a polynomial series [34]:

$$\begin{aligned} B_z(z, r) &= B_{z,0}(z) - \frac{r^2}{4} \frac{d^2}{dz^2} B_{z,0}(z) + \frac{r^4}{64} \frac{d^4}{dz^4} B_{z,0}(z) \dots, \\ B_r(z, r) &= -\frac{r}{2} \frac{d}{dz} B_{z,0}(z) + \frac{r^3}{16} \frac{d^3}{dz^3} B_{z,0}(z) - \frac{r^5}{384} \frac{d^5}{dz^5} B_{z,0}(z) \dots \end{aligned} \quad (2.28)$$

At REGAE not only single solenoids but as well double solenoids are in use. A double solenoid is a combination of two single solenoids with opposite field polarities. By means of the integrals of the on-axis longitudinal field different properties can be calculated. The field integrals are defined as follows:

$$F_n = (B_{z,max})^n \int_{-\infty}^{\infty} b_{z,0}(z)^n dz, \quad (2.29)$$

where $B_{z,max}$ is the maximal longitudinal field and $b_{z,0}(z)$ is the normalized on-axis longitudinal field. The motion of a charged particle through a solenoid is described by coupled equations of motion. The azimuthal motion induced by the radial field component couples to the longitudinal field which causes the radial focusing. The first field integral F_1 is proportional to the *Larmor angle* meaning the effective rotation angle introduced by a solenoidal field to the beam. The Larmor angle of a double solenoid is zero due to the different field polarities. The introduced Larmor angle in the first part is compensated in the second part.

The second field integral defines the focal length f :

$$f(B_{z,max}) = \left[\left(\frac{q}{2 \langle p_z \rangle} \right)^2 F_2 \right]^{-1} \quad (2.30)$$

with the elementary charge q and the average longitudinal momentum $\langle p_z \rangle$.

A calibration measurement is important to convert the applied electrical current into a magnetic field. The calibration for the single and the double solenoid is:

$$B_{z,max}(I_{sol}) [T] = 0.0005 + 0.0211 I_{sol} [A]$$

For the focus strength the second field integral has been measured. These are the results for the single and double solenoid:

$$\begin{aligned} F_2(I_{sol}) [T^2m] &= 0.2 \cdot 10^{-5} + 1.9 \cdot 10^{-5} I_{sol}^2 [A^2], & (\text{single solenoid}) \\ F_2(I_{sol}) [T^2m] &= 0.5 \cdot 10^{-5} + 3.6 \cdot 10^{-5} I_{sol}^2 [A^2]. & (\text{double solenoid}) \end{aligned}$$

Assuming the thin lens approximation (Eq. 2.20) the transfer matrix for each electrical solenoid can be calculated depending on the current I_{sol} . In case of the double solenoid the transfer matrix has not just been approximated by a thin lens but instead by two thin lenses connected with a short drift as:

$$\begin{aligned} \mathbf{M}_{\text{dtl}} &= \mathbf{M}_{\text{tl}} \cdot \mathbf{M}_{\text{D}} \cdot \mathbf{M}_{\text{tl}} \\ &= \begin{pmatrix} 1 & 0 \\ -\frac{1}{f_{\text{tl}}} & 1 \end{pmatrix} \cdot \begin{pmatrix} 1 & l_{\text{D}} \\ 0 & 1 \end{pmatrix} \cdot \begin{pmatrix} 1 & 0 \\ -\frac{1}{f_{\text{tl}}} & 1 \end{pmatrix} \\ &= \begin{pmatrix} 1 - l_{\text{D}}/f_{\text{tl}} & l_{\text{D}} \\ (l_{\text{D}} - 2f_{\text{tl}})/f_{\text{tl}}^2 & 1 - l_{\text{D}}/f_{\text{tl}} \end{pmatrix}. \end{aligned} \quad (2.31)$$

l_{D} is the drift distance between the two thin lenses which are located at the geometrical center of each single solenoid in the double solenoid. The distance is equal to 0.075 m in case of REGAE's double solenoids (namely: Sol23, Sol45, Sol67 (see Fig. 1.2)). The focus strength of the double solenoid is evenly split between both solenoids. Therefore, the focus lengths of the single thin lens (tl) and the double thin lens (dtl) are related as follows:

$$2f_{\text{dtl}} = f_{\text{tl}}.$$

2.1.3 RMS emittance conservation

It will be shown that the RMS emittance holds under a linear transformation. Using the matrix formalism an arbitrary linear transformation can be written as:

$$\mathbf{X} = \mathbf{M} \cdot \mathbf{X}_0, \quad (2.32)$$

where $\mathbf{X}^{\text{T}} = (x \ p_x)$. The transfer matrix is defined as

$$\mathbf{M} = \begin{pmatrix} M_{11} & M_{12} \\ M_{21} & M_{22} \end{pmatrix}. \quad (2.33)$$

It is necessary to prove that the initial RMS emittance $\epsilon_{x,0}$ is equal to the final RMS emittance ϵ_x . The emittance is defined as shown in Eq. 2.9. The linear transformations of a single particle can be obtained from Eq. 2.32, here e.g. the transformation of the position x (analogously for the momentum p_x):

$$x_i = M_{11} x_{0,i} + M_{12} p_{x,0,i}. \quad (2.34)$$

Obviously is the 2nd central moment associative, distributive and commutative as well which will be used in the following as soon as the moments are calculated. The 2nd central moment of the position x is

$$\langle x^2 \rangle = M_{11}^2 \langle x_0^2 \rangle + M_{11} M_{12} \langle x_0 p_{x,0} \rangle + M_{12}^2 \langle p_{x,0}^2 \rangle. \quad (2.35)$$

The product of $\langle x^2 \rangle$ and $\langle p_x^2 \rangle$ is

$$\begin{aligned} \langle x^2 \rangle \langle p_x^2 \rangle &= M_{11}^2 M_{21}^2 \langle x_0^2 \rangle^2 + M_{12}^2 M_{22}^2 \langle p_{x,0}^2 \rangle^2 \\ &\quad + 4 M_{11} M_{12} M_{21} M_{22} \langle x_0 p_{x,0} \rangle^2 \\ &\quad + 2 M_{11} M_{21} (M_{12} M_{21} + M_{11} M_{22}) \langle x_0^2 \rangle \langle x_0 p_{x,0} \rangle \\ &\quad + 2 M_{12} M_{22} (M_{12} M_{21} + M_{11} M_{22}) \langle p_{x,0}^2 \rangle \langle x_0 p_{x,0} \rangle \\ &\quad + (M_{11}^2 M_{22}^2 + M_{12}^2 M_{21}^2) \langle x_0^2 \rangle \langle p_{x,0}^2 \rangle. \end{aligned} \quad (2.36)$$

And the squared correlation of the position and the momentum is as straight forward as the previous:

$$\begin{aligned} \langle x p_x \rangle^2 &= \langle (M_{11} x_0 + M_{12} p_{x,0}) (M_{21} x_0 + M_{22} p_{x,0}) \rangle^2 \\ &= M_{11}^2 M_{21}^2 \langle x_0^2 \rangle^2 + M_{12}^2 M_{22}^2 \langle p_{x,0}^2 \rangle^2 \\ &\quad + (M_{11} M_{22} + M_{12} M_{21})^2 \langle x_0 p_{x,0} \rangle^2 \\ &\quad + 2 M_{11} M_{21} (M_{12} M_{21} + M_{11} M_{22}) \langle x_0^2 \rangle \langle x_0 p_{x,0} \rangle \\ &\quad + 2 M_{12} M_{22} (M_{12} M_{21} + M_{11} M_{22}) \langle p_{x,0}^2 \rangle \langle x_0 p_{x,0} \rangle \\ &\quad + 2 M_{11} M_{12} M_{21} M_{22} \langle x_0^2 \rangle \langle p_{x,0}^2 \rangle. \end{aligned} \quad (2.37)$$

Combining Eq. 2.36 and Eq. 2.37 to calculate the emittance shows that the RMS emittance is conserved under linear transformation.

$$\begin{aligned} \epsilon_x^2 &= \langle x^2 \rangle \langle p_x^2 \rangle - \langle x p_x \rangle^2 \\ &= (M_{11}^2 M_{22}^2 + M_{12}^2 M_{21}^2 - 2 M_{11} M_{12} M_{21} M_{22}) \langle x_0 p_{x,0} \rangle^2 \\ &\quad - [(M_{11}^2 M_{22}^2 + M_{12}^2 M_{21}^2 - 2 M_{11} M_{12} M_{21} M_{22}) \langle x_0^2 \rangle \langle p_{x,0}^2 \rangle] \\ &= (\langle x_0^2 \rangle \langle p_{x,0}^2 \rangle - \langle x_0 p_{x,0} \rangle^2) \underbrace{(M_{11} M_{22} - M_{21} M_{12})^2}_{\det \mathbf{M}} \\ &= \epsilon_{x,0}^2. \end{aligned} \quad (2.38)$$

For the last simplification the property of the determinant of the transfer matrix \mathbf{M} (Eq. 2.21) has been used.

The whole beam optics theory holds for RMS quantities and therefore the RMS should always be the favored choice. The practical drawbacks of RMS values will be discussed in later chapters.

2.1.4 Emittance measurement via a magnet scan

A commonly used method to determine the transverse emittance of an electron bunch is a magnet scan [39, 40]. Here, the phase advance (Eq. 2.25) between a magnet and a downstream position is changed by varying the magnet's current or magnetic field, respectively. Analyzing the beam size at the downstream position as function of the focusing strength yields the emittance. Alternatively, it is possible to measure the beam size at different positions without any additional change of the optics. At REGAE the first method is used and will be presented in the following.

The beam envelope equation (Eq. 2.22) can be used to describe the beam size depending on the magnet strength at the position of the screen. The measured beam sizes and the corresponding transfer matrices can be introduced to the envelope equation. With the method of least-squares [41] the beam emittance and the initial beam parameters can be determined. The method is fully explained and discussed in [35]. The method is utilizing errors of the measured quantities as well which means errors of the beam size determination. If errors are taken into account the fitness quantity $\bar{\chi}^2$ (called *reduced chi-squared*) [42] can be derived. It is defined as

$$\bar{\chi}^2 = \frac{\chi^2}{N - n - 1}, \quad (2.39)$$

where χ^2 is the sum of all quadratic deviations weighted by their errors. N is the sample number and n the number of free parameters. $N - n - 1$ is equivalent to the degrees of freedom. For the emittance measurement the sample number N has to be at least 5 because there are 3 free parameters $(x_{0,\text{RMS}}, (x_{0,\text{RMS}})', \epsilon_x)$, the initial beam parameters and the emittance. $\bar{\chi}^2 \approx 1$ indicates a good fit with a high likeliness. To determine the normalized emittance the kinetic energy of the electron beam has to be known.

The introduced beam optics model is not taking space charge into account but due to the low bunch charges at REGAE it can be neglected in most sections of the machine. Especially in sections used to measure the emittance strong foci which would enhance the space charge forces. Further models including space charge effects are described in [35, 36, 43]. But an experimental proof could not be adduced at REGAE until now.

It will be shown that this measurement method works pretty well at REGAE. And again, it is important that this method holds for RMS beam sizes. Often

Gaussian fits of the beam projections are used to determine the standard deviation which is not necessarily the RMS beam size. The introduced method to determine the emittance is based on the change of the phase advance and the subsequent measurement of the beam size. The beam size is the width of the projection of the spatial coordinate of the phase space. The change of the phase advance is rotating the phase space. Approximated Gaussian profile fits do not follow the theoretical model in general. So that this approach of an emittance measurement does not meet the requirement of a precise determination of the emittance. Hence, it should be given preference to the determination of the RMS beam size. Of course, using a fit routine to determine the beam size has a distinct advantage: It is far less sensitive to any kind of disturbing signals which are technically unavoidable like noise. Therefore, a post-processing routine for images will be introduced to avoid the influence of noise on the RMS beam size calculation.

2.2 Scintillator based particle detectors

There is a huge variety of different kinds of scintillators which can be used to detect all kinds of charged or not-charged particles as well as photons of different energies. The focus of this section lies on the detection of electrons. Via fluorescence the electrons' kinetic energy can be 'converted' to light in the visible wavelength range. In addition to the scintillator a device is necessary to detect the emitted light. Commercially available cameras can have different detection devices. Here, the *charge-coupled device* (CCD) will be explained. The combination of a scintillator screen and a CCD camera is a widely used detection system (e.g. at REGAE) and one of the simplest ways to detect electrons.

2.2.1 Scintillators

In the last decades a broad range of materials has been discovered which can be used as a scintillator to convert the kinetic energy of electrons into light. There are organic as well as inorganic materials. Their field of application could be pretty different. For each application there are different demands a scintillator has to fulfill. The following properties are important for an ideal scintillator used as a part of a beam profile monitor [44]:

- conversion of kinetic energy to detectable light with a high efficiency,

- the material should be transparent to the emitted wavelength and the emitted spectrum should be compatible to the photon detector,
- the decay time has to be short for pulsed electron sources like most accelerators,
- the material should have a practical handling (low hygroscopy, vacuum and radiation stability),
- and of course the costs.

The spatial resolution of a scintillator depends on the transparency as well as indirectly on the light yield of the material. With a higher light yield a thinner scintillator could be sufficient which means effects like electron as well as light scattering can be reduced and the spatial resolution is increased. For some scintillator materials the light yield is proportional to the kinetic energy of particles hitting the scintillator. This property can be used to set up a scintillator spectrometer. This specific aspect has not a high priority compared to former mentioned aspects. Of particular importance for this thesis are the inorganic scintillators. Inorganic scintillators are insulators or semiconductors. The scintillation process depends on the crystal lattice of the material and its energy states (Fig. 2.2). In a pure crystal the only allowed excitation is from a lower band, called *valence band*, to an upper band, called *conduction band*. In the valence band the electrons are bound whereas in the conduction band the electrons have enough energy to migrate freely. Between these two bands is a forbidden band where electrons can never be found. By absorption of energy an electron can be excited from the valence band to the conduction band. Due to recombination of an electron into the valence band a photon is emitted. This process is inefficient and the emitted photon has most likely (due to the material) a high energy and does not lie in the visible range. In order to improve the efficiency of the scintillation process the pure material is doped with another species, called *activator*. If the activator is well chosen the transition from an excited state towards its ground state allows emission of light in the visible range. As a result of the modification of the band structure, energy states exist in the forbidden gap (Fig. 2.2) that ease the de-excitation of an electron back to the valence band. The whole process can be illustrated as the dynamics of an electron-hole pair created by the excitation due to the incident electrons. The positive hole will quickly recombine with a ground-state electron

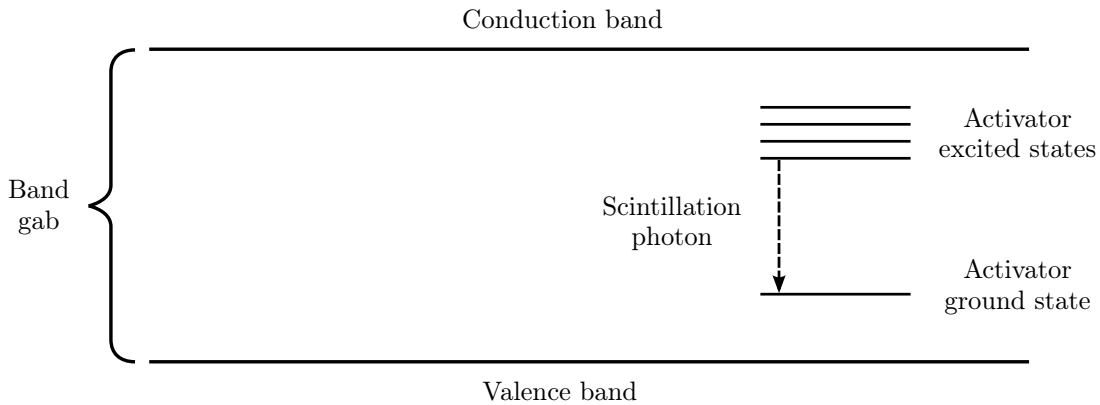


Figure 2.2: Energy band structure of an activated crystalline scintillator.
(From G. F. Knoll [44])

of an activator which will leave an ionized activator. A freely migrating electron in the valence band is able to drop into the activator site. As long as the formed activator state is an excited configuration which allows a transition down to the ground state, a de-excitation will quickly proceed and with a high probability emit a photon. A typical lifetime of such an excited state is 30 ns to 500 ns. In contrast the migration time of an electron is much shorter with the result that the excited states are formed almost at once and therefore the half-life, or *decay time*, of all excited activator states is a characteristic of the scintillation light.

But just a few inorganic scintillators have only a single decay time, more often the decay time is more complex. For example, transitions from some excited states to the ground state can be forbidden and an additional amount of energy is required to reach the ground state. The source of energy could be thermal which can extend the decay time dramatically. This process is called *phosphorescence* and the 'long-time' decay component is often called *afterglow*.

Another possibility is the *quenching*. It means that an electron is captured at an activator site and transits without any radiation from an excited state to the ground state. This mechanism reduces the conversion rate of the particle energy to scintillation light yield.

As already mentioned the transparency of the scintillator material to the emitted light is important. In a pure crystal a certain amount of the emitted photons would be directly absorbed again because the emission and absorption spectrum

are overlapping. On the other hand, the emission spectrum on the activator side is shifted relative to the absorption spectrum of the bulk of the crystal and the light yield is higher.

Of particular interest is the alkali halide cesium-iodide doped with thallium (CsI(Tl)) which is used for the REGAE detector system. It has some advantages over other scintillator materials of this type e.g. sodium-iodide (NaI). It is less brittle and can be bent into various shapes without fracturing. Furthermore it is less hygroscopic than NaI. Only high humidity or direct contact with water can deteriorate the material. Another useful property is: it can be grown on patterned substrates. This allows to grow small columns where every single column behaves like an optically isolated scintillator. The microstructure reduces the lateral spread of the emitted photons and a better spatial resolution can be achieved. More details are presented in Sec. 3.1.2.

2.2.2 CCD based image sensors

The CCD, firstly presented by W. S. Boyle and G. E. Smith [45], is a device to store and shift electrical charges from the device to an area where the charge can be manipulated like being digitized. A common application of a CCD chip is the usage as an image sensor. Here, every pixel of the active area of the sensor is represented by a *metal-oxide-semiconductor* (MOS) capacitor. The schematic layout and function is illustrated in Fig. 2.3. The MOS consists of a silicon substrate, a silicon dioxide layer and polycrystalline silicon layer on top. Because the silicon dioxide layer is a dielectric material the structure has the functionality of a capacitor. Assuming a p-doped semiconductor (silicon) applying a positive voltage V_G from the gate to the body creates a depletion layer inside the semiconductor which is free of any carriers. If the voltage is high enough a thin *inversion* layer is formed at the semiconductor-insulator interface. As soon as the density of electrons in the inversion layer is equal to the density of holes in the body the threshold voltage is reached. In this state the MOS can be expose to light. The light generates electron-hole pairs proportional to its intensity inside the depletion layer. Due to the electric field they will be separated and the electrons move toward the surface and the holes toward the substrate. The charge is accumulated during the exposure time or until the thermal equilibrium is reached which is called to be a full well. Therefore the capacity of storing electrons is called *well depth*.

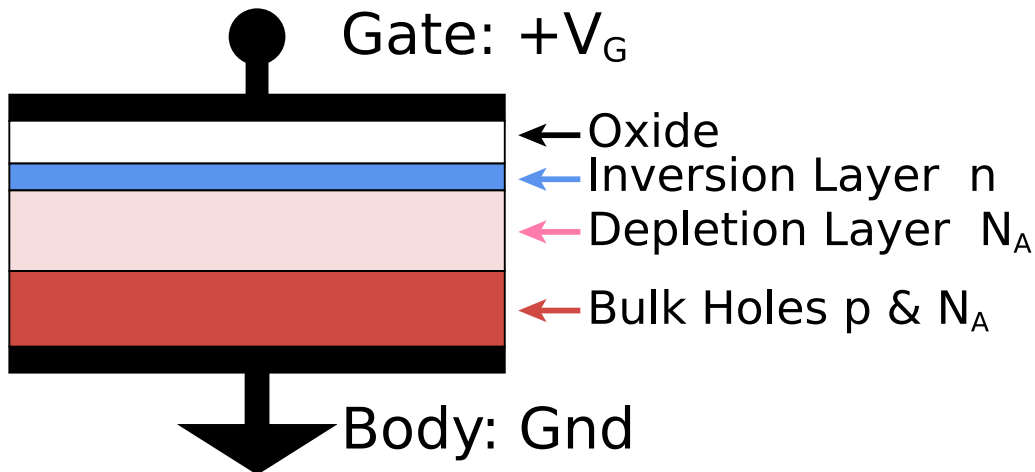


Figure 2.3: Schematic illustration of a metal-oxide-semiconductors (MOS) capacitors. N_A denotes the density of the acceptors and p the density of the holes. In the depletion layer are no holes, whereas in the bulk $N_A = p$. Figure originates from [46].

The actual CCD is controlling the charge transportation. By applying different voltages to certain arrays of electrodes the charge flow can be controlled and stored charge can be shifted to the next array. In case of an image sensor the array is often 2 dimensional. The closest pixel row will then be shifted to the readout device which is connected to the CCD and subsequently all remaining rows are shifted closer to the readout device. By repetition the whole pixel array can be read out and afterwards cleared for the next exposure. If the charge is not generated by an incident photon but instead thermally the contribution to the signal is called *dark current*. It can be reduced by cooling the CCD. Another source of noise is the shifting of the charge from one array to another.

2.3 Laser Plasma Acceleration (LPA)

This section motivates the plasma acceleration scheme and summarizes the most important results of LPA which are required for this work. More detailed studies and descriptions of this field and especially for a REGAE-like or specific REGAE case can be found in [10, 25]. Due to the LPA experiment new demands for the transverse optics have occurred. Introducing the general mechanisms of the linear regime of the LPA results in constraints for the transverse optics. In a later chapter

simulations with the new transverse beam optics will be presented which fulfill these constraints.

But first of all the basic mechanism of exciting a plasma oscillation is presented. Forcing a charge separation in a plasma creates a region of high electrical field gradients which can be used to accelerate electrons in a controlled manner. As a driver to generate regions of high field gradient charged particle bunches with a high beam current as well as short high power laser pulses are used. Here, the focus lies on the laser based scheme.

The so called *ponderomotive force*, a nonlinear second order force pushes the plasma electrons away from their rest position but in good approximation not the much heavier protons or atoms. The ponderomotive force is given by

$$\mathbf{F}_p = -\frac{m_e c^2}{2} \nabla a^2, \quad (2.40)$$

where $a = e A / (m_e c^2)$ is the normalized vector potential. Depending on the normalized vector potential a_0 two different regimes of LPA can be entered. For $a_0 \geq 1$ the *non-linear regime* is entered. Here, the transverse deflection of the plasma electrons due to the electrical field component is strong enough so that the electrons reach an area of less laser intensity in less than a half period of the laser oscillation. Because the repulsing force is smaller a net deflection remains. In parallel to this process the transverse motion couples to the magnetic field component of the laser field. The magnetic field causes an additional longitudinal motion of the electrons. Only if the laser intensity change is fast enough during the longitudinal deflection a net deflection remains in the longitudinal direction. For short laser pulses the intensity changes even fast enough for a normalized vector potential smaller than 1.

Therefore, even for $a_0 \ll 1$ a longitudinal net deflection of the plasma electrons is achieved which causes a density modulation of the plasma. An oscillation is excited and the required regions of high electrical field gradients are generated. The laser field deflects the plasma electrons in transverse direction as well, otherwise the longitudinal oscillation would not occur, but due to the lower a_0 there is no net deflection. The regime of $a_0 \ll 1$ is called the *linear regime* and the excited plasma wakefields have in good approximation a sinusoidal shape which can be analytically described and solved for all three dimensions. Furthermore it is the targeted aim of the REGAE experiments to operate in the linear regime. The characteristic length scale of a plasma wakefield period is given by the *plasma period*

λ_p and can be expressed as

$$\lambda_p = \frac{2\pi c}{\omega_p},$$

$$\omega_p = \sqrt{\frac{ne^2}{m_e \epsilon_0}},$$

where ω_p is the *plasma frequency* and n is the *plasma density*.

Assuming a linearly polarized, Gaussian shaped laser pulse the normalized vector potential is

$$\mathbf{a}(r, \xi) = \frac{1}{\sqrt{2}} a(z) \exp\left(-\frac{r^2}{w(z)^2}\right) \exp\left(-\frac{\xi^2}{4\sigma_{z,1}^2}\right) \cos(k_1 \xi) \hat{\mathbf{e}}_x \quad (2.41)$$

in the linear regime. Here, the transverse coordinates x and y have been reduced to the radial coordinate $r = \sqrt{x^2 + y^2}$ and the longitudinal coordinate z has been transformed to the co-moving coordinate $\xi = z - v_g t$, where v_g is the laser group velocity. Furthermore the laser pulse length $\sigma_{z,1}$ and the laser wave number k_1 have been introduced to describe the laser vector potential \mathbf{a} . The laser beam waist $w(z)$ describes the laser beam evolution from its focus and $a(z)$ is the amplitude of the vector potential.

For the wakefield in the linear regime the following expressions can be found:

$$E_z(r, \xi) = \frac{m_e c^2 k_p^2 \sigma_{z,1}}{2e} \sqrt{\frac{\pi}{2}} a(z)^2 \exp\left(-\frac{k_p^2 \sigma_{z,1}^2}{2} - \frac{2r^2}{w(z)^2}\right) \cos(k_p \xi) \quad (2.42)$$

$$E_r(r, \xi) = -r \frac{2m_e c^2 k_p \sigma_{z,1}}{e} \sqrt{\frac{\pi}{2}} \frac{a(z)^2}{w(z)^2} \exp\left(-\frac{k_p^2 \sigma_{z,1}^2}{2}\right) \sin k_p \xi. \quad (2.43)$$

The fields are illustrated in Fig. 2.4. E_z and E_r have a relative phase shift of $\pi/2$. The on-axis focusing strength $K(\xi)$, in dependence on the relative longitudinal position ξ , can be determined by deriving $E_r(r, \xi)$ with respect to r :

$$K(\xi) = \frac{e}{\gamma m_e c^2} \left. \frac{\delta E_r}{\delta r} \right|_{r=0} = -\frac{2k_p \sigma_{z,1}}{\gamma} \sqrt{\frac{\pi}{2}} \frac{a(z)^2}{w(z)^2} \exp\left(-\frac{k_p^2 \sigma_{z,1}^2}{2}\right) \sin k_p \xi. \quad (2.44)$$

The lowest plot in Fig. 2.4 compares the accelerating abilities of the longitudinal field with the focusing abilities of the radial field. The overlap of the focusing and accelerating phases is only $\pi/2$ and can be used for electron acceleration.

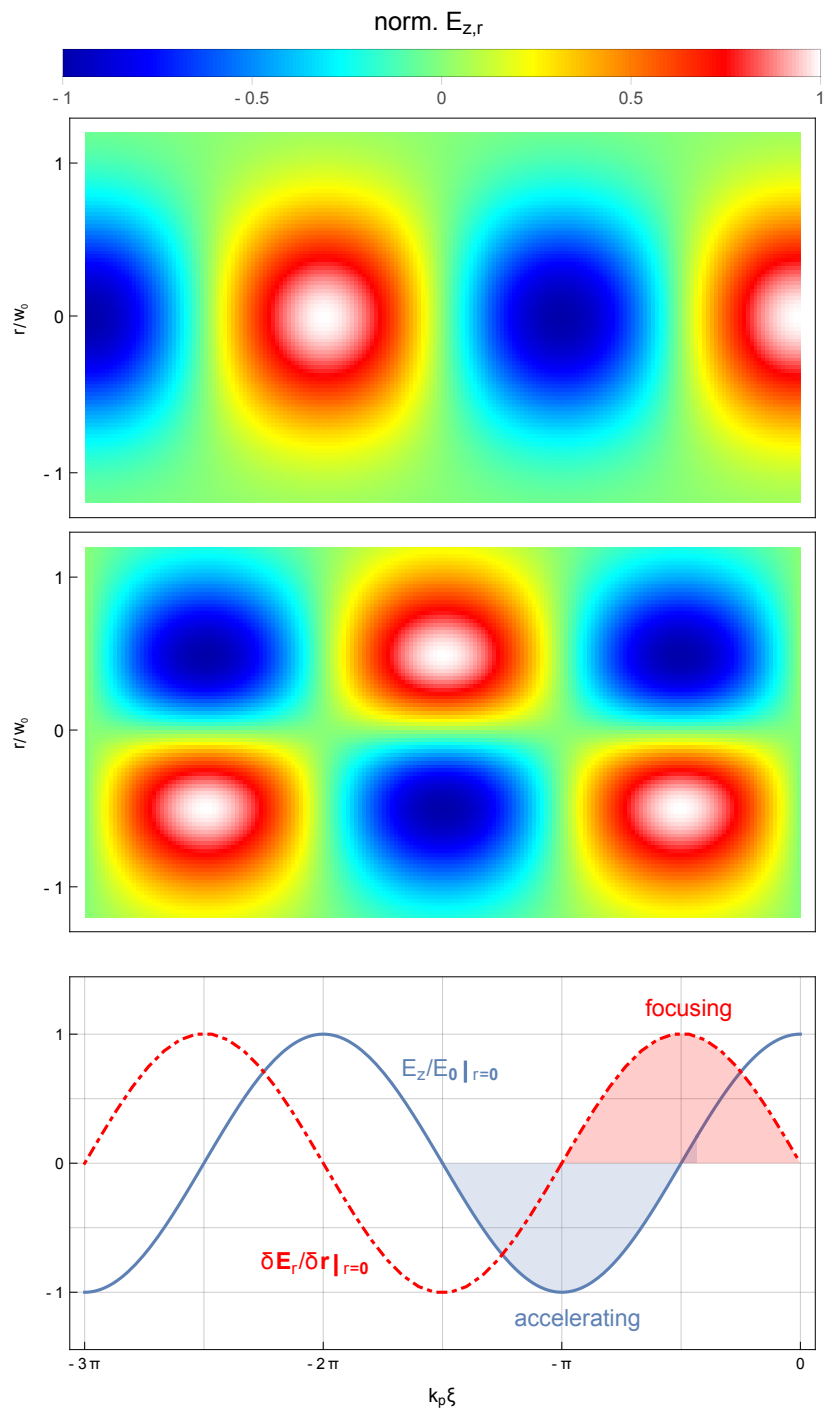


Figure 2.4: Illustration of plasma wakefield. components close to the longitudinal axis. The laser pulse is at $k_p \xi = 0$ but not illustrated in these plots.

Transverse beam diagnostic for ultra-low bunch charges at REGAE

This chapter is dedicated to the REGAE detector system which is the most important transverse measuring device for a broad spectrum of experiments and beam diagnostics as the transverse beam emittance measurement at REGAE. It combines a high light yielding scintillator which achieves due to its construction still a reasonable resolution and a high sensitive EMCCD camera. Both components as well as the overall performance will be described in detail in the first section of this chapter. The high qualitative manufacturing and the technical feasibility to reduce noise to a minimum enables the camera to resolve even smallest bunch charges down to a few fC. These capabilities offer the possibility to evaluate beam images with respect to the beam size in a reliable and precise kind. The RMS beam size is the crucial quantity to calculate the beam emittance by means of the introduced measuring method (Sec. 2.1.4).

Nevertheless there are still disruptive sources of noise which will be part of the second section. Especially, noise induced by the detector system itself and by the nature of electron emissions will be discussed. One important realization is the dominance of the fundamental *shot-to-shot* fluctuation of electron emissions in contrast to the detector camera induced noise. Therefore a fundamental description of the electron fluctuations or respectively the related photon emission in the detector system is required.

During the operation of REGAE a distinct beam halo broadening the beam profile has been observed. The last section of this chapter treats the investigations done to identify the source of this halo. Its origin has been revealed by different measurements at REGAE and in the laboratory as well as by means of simulations. As a result it is reasonable to handle the halo as an artifact of the detector system which has to be neglected to get realistic beam size results. The method to treat the halo is reliable and influences the common beam diagnostic routine only minimally.

The correct treatment of different sources of disturbance offers the possibility to calculate highly reliable beam sizes from almost arbitrary beam profiles. The introduced routines have proved a high stability during the work at REGAE. The results of the emittance measurements presented in Chap. 5 are established on the investigations of this chapter. Their precision could only be achieved due to the detailed description of different sources of noise, the profound handling of the beam halo and of course a superb detector system with its ability to reduce technical sources of noise to a minimum.

3.1 Detector system (D1) at REGAE

The D1 detector system has been designed and integrated at REGAE by H. Delsim-Hashemi¹. It is the main tool to diagnose transverse beam parameters of the electron beam with a high sensitivity, spatial resolution and an adequate frame rate. D1 combines a scintillator, light optic and CCD camera and is meant to measure diffraction patterns at the very end of the REGAE accelerator (see Fig. 1.2). Due to its capabilities and position it is perfectly suited for all kind of transverse beam diagnostic applications as well.

It contains a cesium-iodide thallium-doped (CsI(Tl)) scintillator. As a specialty the CsI(Tl)-crystals are grown onto a Fiber Optic Plate (FOP) which increases the spatial resolution of the scintillator and consequently of the whole detector setup. This element is called Fiber Optic Scintillator (FOS). It has been manufactured by Hamamatsu Photonics [47]. In order to detect the emitted light of the FOS an Andor iXon3 camera with a charge sensitive Electron-Multiplying CCD (EMCCD) element [48] is installed. The pixel size of the CCD is 13 μm and the size of each fiber of the FOS is $\sim 6 \mu\text{m}$. The overall spatial resolution of this detector system is

¹hossein.delsim-hashemi@desy.de

$\sim 16 \mu\text{m}$ due to the light optic merging the scintillator and camera. This resolution is sufficient for all kind of experiments performed at REGAE and especially for all presented measurements and results of this thesis. Due to the parameter range of the accelerator the beam dynamics does not allow strongly focused electron bunches at this position. One of the smallest measured beam sizes at D1 is still $\sim 50 \mu\text{m}$.

A schematic layout of the detector system is shown in Fig. 3.1. The FOS is orientated perpendicular to the beam propagation. To avoid high-energy photons or electrons hitting the EMCCD camera a mirror reflects the visible light emitted by the FOS under 90° in direction of the camera. Furthermore a lead shielding is placed close to the camera to avoid scattered high-energy photons from the front of the accelerator hitting the CCD. An Aluminum cover, directly coated onto the FOS reflects the emitted light of the FOS back in direction of the mirror. The whole setup is light-tight. D1 is optimized to achieve a high charge sensitivity on the one hand and still a reasonable spatial resolution on the other hand. Tests done with this setup have shown that it is able to detect single electrons [49].

The following subsections introduce the camera as well as the FOS in detail. Finally the detector efficiency will be theoretically estimated and could be verified by a measurement.

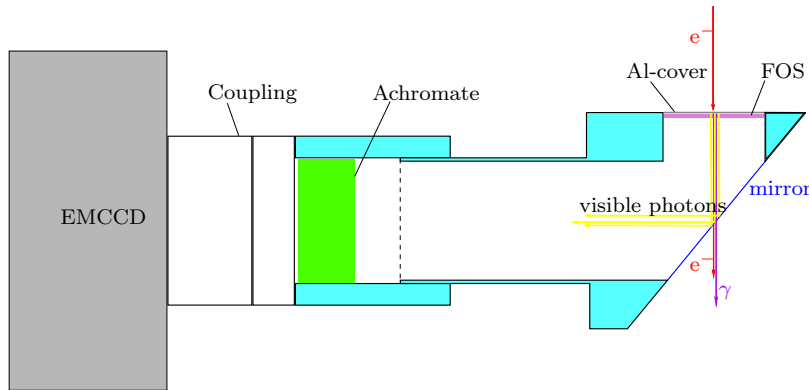


Figure 3.1: Layout of the REGAE detector. Figure adapted from [49].

3.1.1 Andor iXon3 EMCCD cameras

The installed CCD camera is an Andor iXon3 888 EMCCD camera [48]. It has a high dynamic range what makes it capable of detecting single photons up to ten

thousands of photons per pixel. Furthermore the frame rate up to 9 frames/s makes it the best solution for a detector system at REGAE. The exact specifications can be found in Tab. 3.1. As a spare camera an Andor iXon3 885 is available. Its specifications are listed as well for completeness.

The signal detection can be described in three to four steps. First the signal

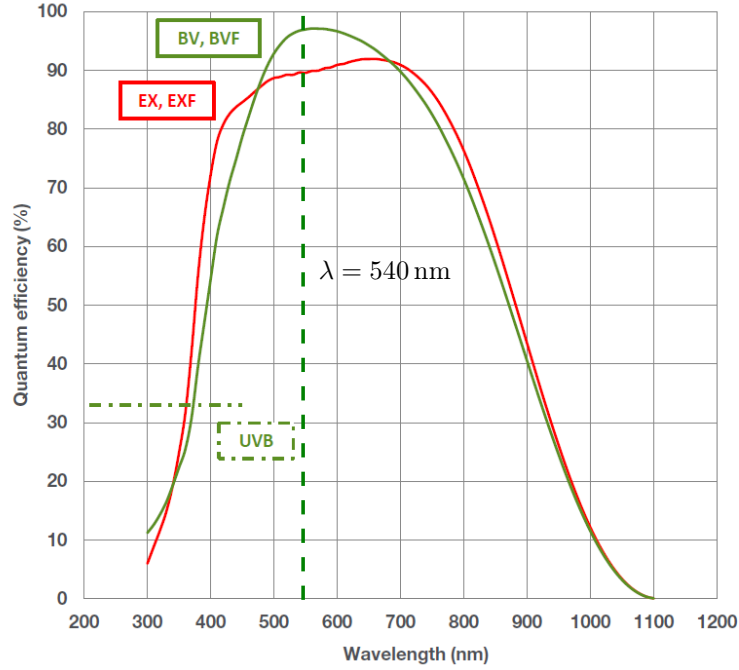


Figure 3.2: Quantum efficiency of an Andor iXon3 888 back-illuminated EM-CCD (green curve (BV, BVF)). Figure originates from [48].

in form of photons is hitting the CCD chip and excites an electron. This process is limited by the *quantum efficiency* (QE) of the CCD material. The QE of the iXon3 888 CCD is shown in Fig. 3.2. Its maximum is reached at a wavelength of $\lambda = 540$ nm and is $\sim 92.5\%$. The wavelength corresponds perfectly with the used scintillator material (see Sec. 3.1.2). After the active area of the CCD has been exposed to the signal the pixels will be shifted to the storage area to clean the active area and prepare it for the next exposure. The stored pixels will be shifted row by row to the readout register. Each row will be consecutively readout pixel by pixel. The two-dimensional array is now one-dimensional. If the EM gain is activated the readout register will be transferred to the multiplication register and amplified. This will be explained below. Finally the analog signal will be digitized

in an analog-digital converter (ADC) to 14 or 16-bit.

The CCD chip is mounted on a Peltier cooling element in an evacuated housing (see Fig. 3.3, right). The Peltier element uses the thermoelectric effect to rapidly cool the chip down. The, so called, TE cooler has a cold and a hot end. The heat is efficiently dissipated via a fan means air cooling or an additional water cooling to reach even lower temperatures. With the water cooling temperatures down to -95°C are achievable. This would be required for single electron event experiments. In case of multi-event detection as at REGAE the normal air chill down to -70°C is sufficient. The cooling is necessary to reduce thermally induced noise. The light hitting the sealed CCD chip enters the housing through an anti-reflection coated window which reduces intensity losses.

The iXon3 models are made to reduce all kinds of noise induced by a camera.

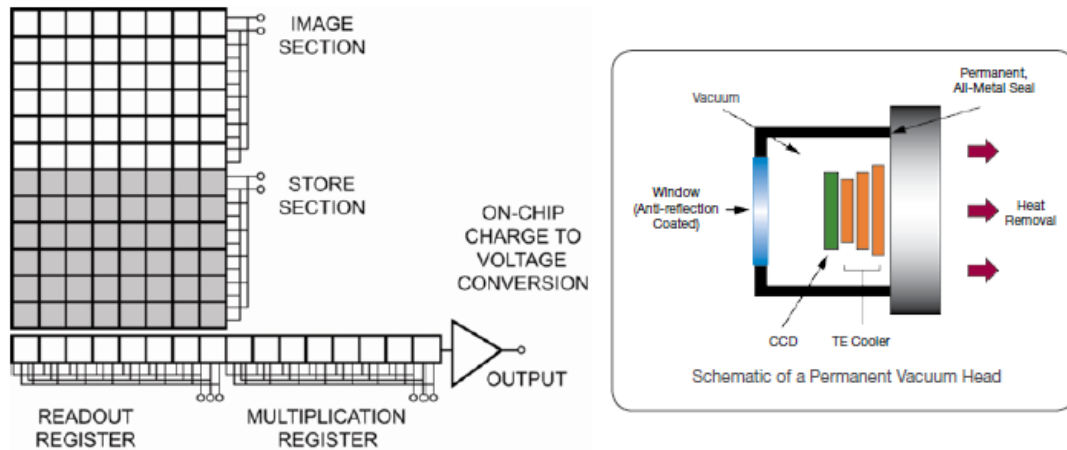


Figure 3.3: **Left:** Schematic layout of CCD chip and register transfer as well as gain/multiplication register. **Right:** Schematic of the iXon3 vacuum head including CCD chip and TE cooler. Figures originate from [48].

There are several sources of noise. First of all there is dark charge, means charge thermally excited on the sensitive area of the chip which is added to the signal. Due to the cooling of the CCD and short integration time this contribution can be ignored. Another source of noise is the clock induced charge (CIC). It is generated by shifting the charges from the sensitive area to the storage area. CIC is specified by the manufacturer with well below $1 e^-/\text{pixel}$. Even for single electron detection CIC is well controlled with this camera. But in case of electron bunches generating

a huge amount of scintillation light CIC is negligible. Another often dominant noise source is the readout noise. Especially, if the signal is amplified in the ADC, the readout noise increases by the applied gain. The EMCCD technology amplifies the signal before it is digitized. The readout noise at the ADC is therefore reduced. The electron-multiplying of the iXon3 models have a special multiplication register in addition to the normal shifting register. The multiplication register is operated at a higher potential so that electrons create additional electron-hole pairs by ionization and consequently amplifying the signal. This multiplication itself follows a statistical process as well and is source of noise again. The uncertainty of the amplification is limited to $\sqrt{2}$ what can be theoretically as well as empirically shown [50]. All the introduced noise sources like dark charge, conventional readout noise as well as CIC can be neglected due to the technical measures on side of the camera or the nature of the signal. Therefore there is only the noise of the signal itself and the multiplication noise factor ($\sqrt{2}$) of the camera. This can be consolidated to the overall noise as

$$\text{Overall Noise} = \text{Signal Noise} \times \sqrt{2}.$$

From the high sensitivity of the camera it follows that shot noise of the signal is the dominant sources of noise. In Sec. 3.2.1 the contributions of the signal and background noises are explained and an analytical description is introduced.

Table 3.1: Characteristics of Andor iXon3 885/888 EMCCD cameras. Data originates from [48].

Type	iXon 885	iXon 888
Quantum efficiency (@ -70°C)	~ 0.65	~ 0.925
Active Pixels (H \times V)	1002 \times 1004	1024 \times 1024
Pixel Size (H \times V)[μm]	8 \times 8	13 \times 13
Image output	14-bit	14-/16-bit
Frame rate (full frame) [fps]	31.4	8.9
Min. exposure time [μs]	10	10
Cooling [$^\circ\text{C}$]	-95	-95
Pixel Well depth [$\# e^-$]	30 000	$\sim 80\,000$

3.1.2 Hamamatsu Fiber Optic Scintillator (FOS)

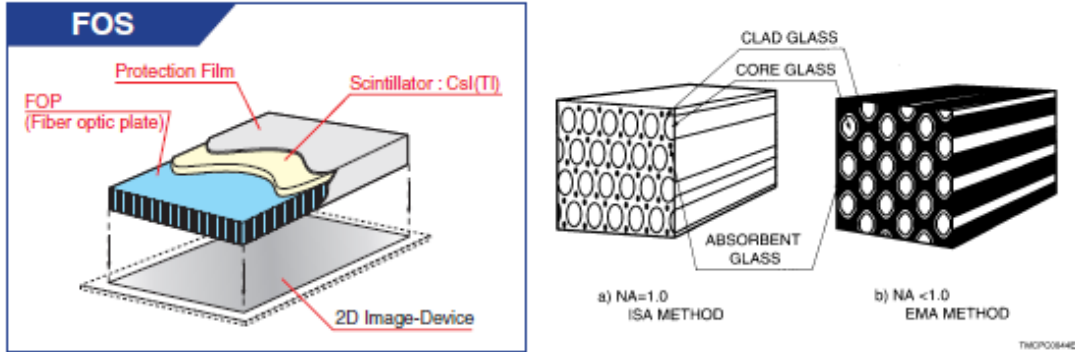


Figure 3.4: **Left:** Schematic composition of a Hamamatsu Fiber Optic Scintillator (FOS). **Right:** Schematic structure of a Fiber Optic Plate (FOP). Figures originate from [47].

The Hamamatsu Fiber Optic Scintillator (FOS) [47] is a CsI(Tl)-crystal-screen which is evaporated onto a Fiber Optic Plate (FOP) (Fig. 3.4, left). This setup is a superior design of a scintillator screen. The CsI(Tl) crystals are grown perpendicular to the supporting base, have a needle-like shape and function themselves as a light guiding structure (Fig. 3.5). CsI(Tl) as a scintillation material has a benefit in combination with the installed EMCCD chip because the scintillation spectrum and the quantum efficiency have a huge overlap (compare Fig. 3.2 and Fig. 3.7, left). Furthermore the light yield per deposit energy is high and stable at room temperatures (Fig. 3.7, right).

On the other hand the FOP guides the scintillation light. The FOP is a composition of fiber optics and absorbent glass (Fig.3.4, right; the used FOS has a FOP packed like the schematic graphic 'a) NA=1.0 ISA METHOD'). Because the fibers accept just a specific solid angle range they operate as a kind of filter for the angular distribution of the scintillation light. The narrow emission of the scintillation light reduces the spherical aberration of the optical system connecting the FOS and the camera and consequently the overall spatial resolution of the detector system is improved. The guiding of the fiber optic is illustrated in Fig. 3.6. The acceptance angle θ_{\max} is described by the *numerical aperture* (N.A.) which is defined as

$$\text{N.A.} := n \sin \theta_{\max} = \sqrt{n_1^2 - n_2^2},$$

where n_1 and n_2 respectively refers to the refractive indices of the core and clad

glass. The numerical aperture is equal to 1 for the FOP. In air ($n = 1$) the acceptance angle θ_{\max} is 90° . Using the refractive index of CsI (Tab. 3.2) $\theta_{\max} = 35.2^\circ$. All properties of the FOP are shown in Tab. 3.3.

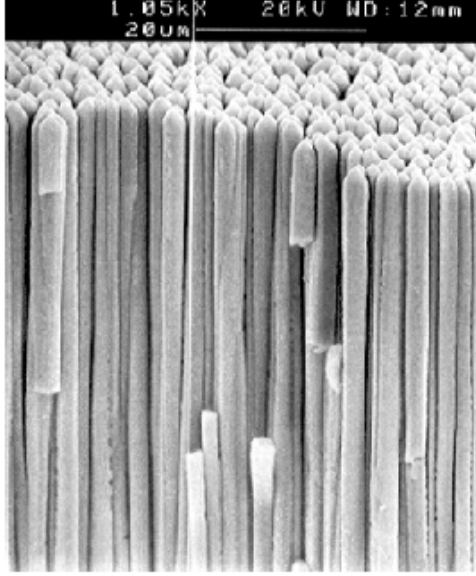


Figure 3.5: Vapour-deposited column-shaped CsI(Tl) scintillation crystals of very smooth structure. Diameter $\sim 3 \mu\text{m}$, length $> 0.5 \text{ mm}$. Figure originates from [51].

N.A.	1.00
n_1	1.82
n_2	1.495
$d_{\text{fiber}} [\mu\text{m}]$	6
Core Glass P.F. [%]	74
Clad Glass P.F. [%]	24.7
Absorb. Glass P.F. [%]	1.3
Dimensions [mm^2]	15×15
Thickness [mm]	3

Table 3.3: Properties of the FOP contained in the FOS used at REGAE. The refractive indices n_1 and n_2 are defined like in Fig. 3.6. P.F. means ‘packing fraction’. Data originates from [47].

For the later usage it is worth to have a closer look at the core and clad glass of the FOP. Of special interest is the average density of the FOP. Due to the high refractive index of the core glass it is probably made of flint glass ($\text{SiO}_2\text{-PbO}$). For the clad glass it is not clear. But from Fig. 3.8 the average density of the the FOP ρ_{FOP} can be approximated. The dependency of the refractive index and the density of glass can be well approximated by a polynomial model, introduced in [54]. The refractive index and the density of silicate glass behave almost linear.

Table 3.2: Comparison of NaI(Tl) and CsI(Tl). Data originates from [44].

Alkali Halides	Density [g/cm ³]	Refractive index	λ max. emission [nm]
NaI(Tl)	3.667	1.85	415
CsI(Tl)	4.51	1.8	550
	Decay time [μ s]	Light yield [Photon/MeV]	
NaI(Tl)	0.23	38 000	
CsI(Tl)	0.68(64%), 3.34(36%)	65 000	

With the ratio of core and clad glass - given in Tab. 3.3 - contains in the FOP the obtained average density is $\rho_{\text{FOP}} \simeq 4.5 \text{ g cm}^{-3}$.

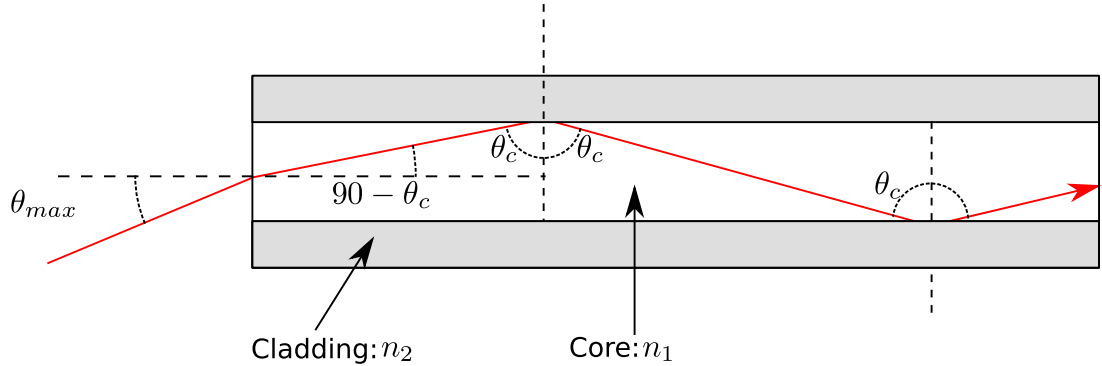


Figure 3.6: Schematic illustration of light guiding inside a fiber optic. The acceptance angle θ_{max} is defined by the refraction indices n_1 and n_2 , which defines the critical angle θ_c of a total reflection inside a fiber. Figure originates from [52].

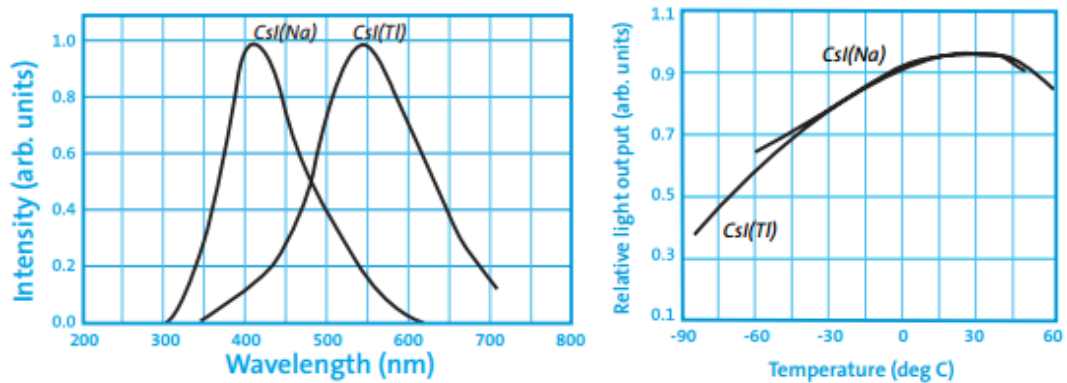


Figure 3.7: Left: Spectrum of the scintillation light of CsI(Tl) and CsI(Na). **Right:** Light output depending on temperature for CsI(Tl) and CsI(Na). Figures originate from [53].

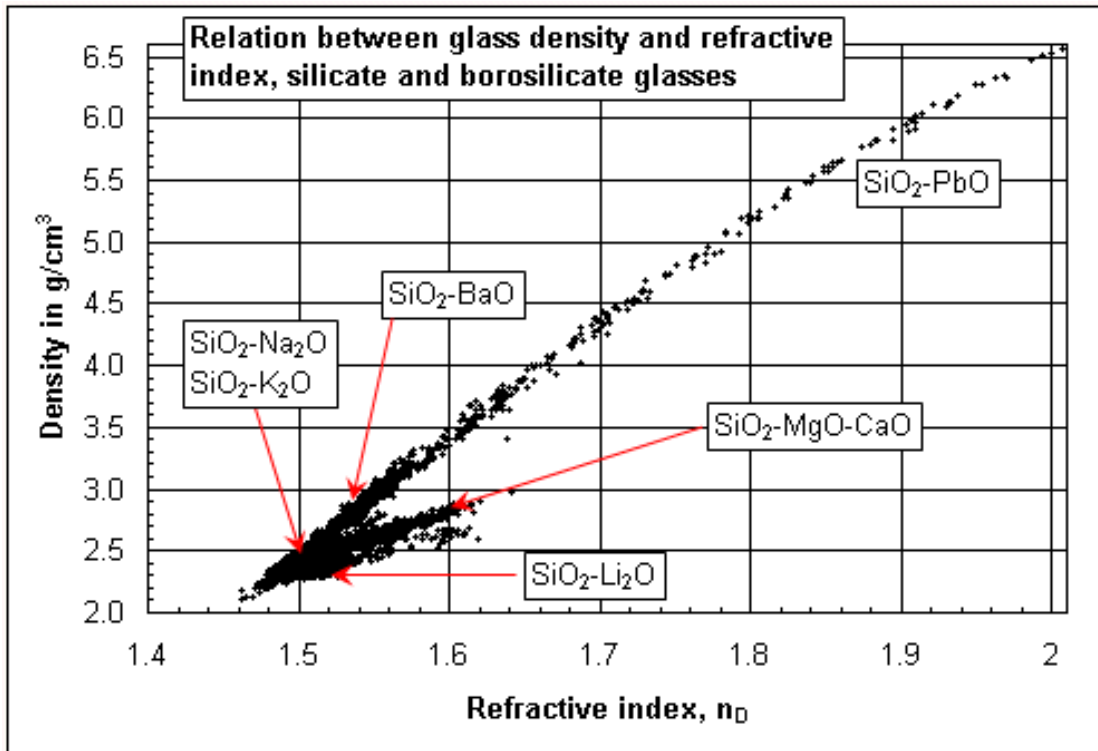


Figure 3.8: Relation between material density and refractive index for different glass compositions. Plot is based on [54]. Figure originates from [55].

3.1.3 REGAE detector system efficiency

Detector efficiency means the conversion from kinetic energy of the accelerated electrons to scintillation light inside the scintillator and the subsequent conversion to an electrical signal at the detector camera. For this purpose it is necessary to determine the light yield of the scintillator depending on the mean beam energy as well as the angle acceptance of the detector light optic. Furthermore, the conversion of light-to-signal of the EMCCD camera has to be taken into account. Simple assumptions will be made to describe and estimate the overall detector efficiency theoretically. Then a measurement will be presented to verify the estimation.

CsI(Tl)-FOS light yield

Starting with a pure CsI(Tl) crystal and ignoring the FOP for a moment makes it easier to estimate the maximum photon number expected from the scintillator layer. The light yield depends mainly on three properties: the scintillator material, the scintillator's thickness and the kinetic energy of the incoming species which are electrons in this case. These three parameters determine the deposited energy. Due to the relativistic energies of the electrons the thickness is not negligible because the electrons are not stopped by the scintillator and just a fraction of the kinetic energy is deposited inside the scintillator. There are other parameters which influence the light yield like the temperature and the activator concentration. These effects will be ignored for this simple considerations. Aside from this they are just giving small variations of the light yield. The temperature influence is shown in Fig. 3.7. Normally the conditions are close to optimum: the highest scintillation efficiency of CsI is close to room temperature that can be assumed in case of the REGAE environmental conditions and furthermore CsI(Tl) does not strongly depend on the Tl⁺ concentration [56].

The stopping power $P(E_{\text{kin}})$ of a material depends mostly on its density. For electrons there are two mechanisms mainly contribute to their energy loss inside a material. For electrons below a kinetic energy of roughly 1 MeV it is the collision with the target's atoms. The atoms can directly be ionized or excited. For electrons with a higher kinetic energy the cross section is decreasing and the energy loss due to coulomb interaction gets more dominant and increases. The electrons are deflected inside the electromagnetic field of the target and irradiate. This radiation can be absorbed by the target material again. The sum of both mechanisms yields

the total stopping power which is deposited inside the target. Fig. 3.9 shows the

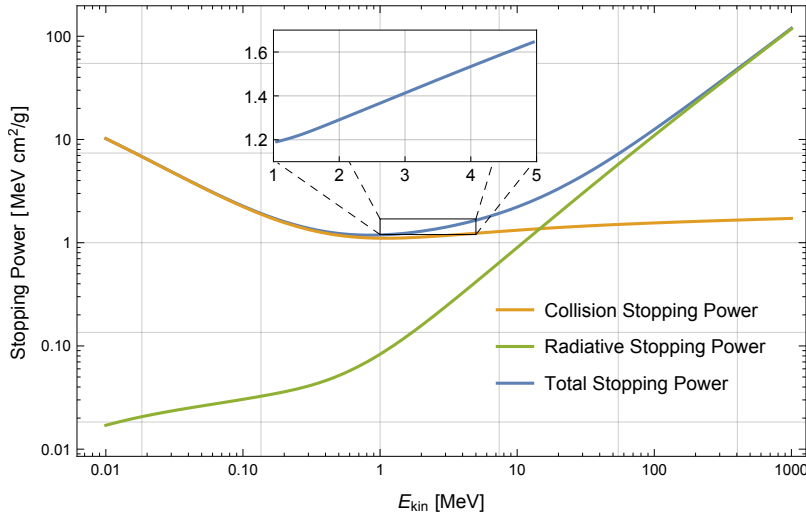


Figure 3.9: Stopping power of CsI. Curves base on data from [57].

stopping power of CsI. Especially, the region of 2 MeV to 5 MeV is of interest for REGAE. The deposited energy of a single electron E_{e^-} is given as:

$$E_{e^-}(E_{\text{kin}}) = P(E_{\text{kin}}) \rho a \quad (3.1)$$

with the density ρ and the scintillator thickness a in forward direction of the electrons. To estimate the light yield a mean beam energy E_{kin} of 3 MeV which is typical for REGAE is assumed and a scintillator thickness of $a = 150 \mu\text{m}$ is used. Introducing these parameters and the material specific stopping power as well as the density (Tab. 3.2) to Eq. 3.1 an energy of 95.6 keV will be deposited by a single electron. The conversion efficiency (light yield per MeV) is given in Tab. 3.2. This yields **6213 photons** over the full solid angle of 4π .

The solid acceptance angle of the connecting light optics (illustrated in Fig. 3.10) determines the fraction of photons reaching the detector camera and is defined by its setup. Due to the transition between different materials the refraction indices of CsI has to be known (Tab. 3.2). The refractive indices of the FOP is not essential. This can be easily shown. By means of *Snell's law* each transition between two media can be expressed as:

$$\begin{aligned} n_{\text{CsI}} \sin(\alpha_{\text{CsI}}) &= n_{\text{FOP}} \sin(\alpha_{\text{FOP}}), \\ n_{\text{FOP}} \sin(\alpha_{\text{FOP}}) &= n_{\text{vac}} \sin(\alpha_{\text{vac}}). \end{aligned} \quad (3.2)$$

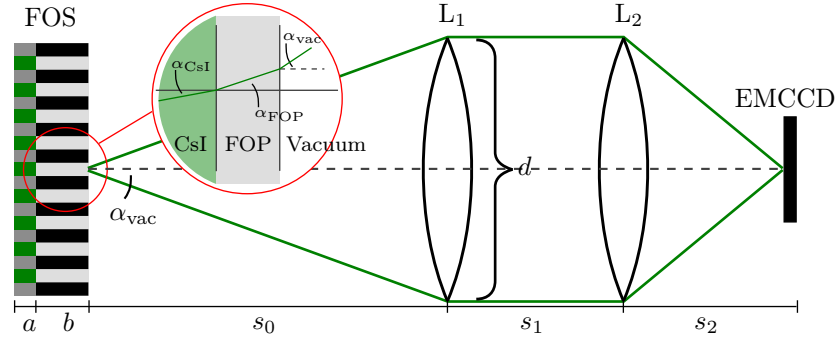


Figure 3.10: Light optic of D1. Where $a = 150 \mu\text{m}$ is the thickness of the CsI scintillator; $b = 3 \text{ mm}$ is the thickness of FOP. s_{0-2} are the distances between the FOS, lenses and the EMCCD; $s_0 = 400 \text{ mm}$, $s_1 = 350 \text{ mm}$, $s_2 = 300 \text{ mm}$. Focal lengths f_1 and f_2 of the lenses L_1 and L_2 are identical with the distances s_0 and s_2 . The lenses' diameter is $d = 2''$.

Concluding Eq. 3.2 with $n_{\text{vac}} = 1$ yields for α_{vac} :

$$\sin(\alpha_{\text{vac}}) = n_{\text{CsI}} \sin(\alpha_{\text{CsI}})$$

which just depends on α_{CsI} . On the other hand α_{vac} is defined by the distance s_0 to the first lens L_1 and its diameter d . Using the approximation for small angles α_{CsI} can be written as

$$\alpha_{\text{CsI}} = \arcsin\left(\frac{d}{2 s_0 n_{\text{CsI}}}\right).$$

The corresponding solid angle is a fraction of a 4π -sphere. The resulting three dimensional object can be imagined as a cone. The solid angle of a cone with apex angle $2\alpha_{\text{CsI}}$ is defined as:

$$\theta_{\text{acc}} = 2\pi(1 - \cos(\alpha_{\text{CsI}})).$$

The distance from the FOS to L_1 is $s_0 = 40 \text{ cm}$ and the diameter of L_1 is $d = 2''$. This leads to a solid acceptance angle θ_{acc} of 0.0038 sr . The fraction of the total light yield collected by the detector optic is $0.0038/4\pi \simeq 3.0 \times 10^{-4}$. The principle transmittance of the integrated FOP is quoted as 66% for Lambertian source [47] at 550 nm from the manufacturer. This fact is negligible because just a very small solid angle in forward direction is of particular interest. Therefore the

highest expected light yield of REGAE's CsI(Tl)-FOS should be $6213 \cdot 3.0 \times 10^{-4} \simeq$ **1.86 photon/e⁻** for the assumed machine parameters and geometrical setup of the detector system. This estimation assumes a perfectly transmitting optic and ignores the reflecting effect of the Aluminum coating of the FOS which should increase the light yield in forward direction.

Experimental photon calibration of the REGAE detector system

To verify the former estimated light yield of the FOS it is necessary to calibrate the used Andor iXon3 EMCCD camera. There are two versions of this type in use - the 885 and 888. For the measurement the Andor iXon3 888 has been used. To calibrate the light yield a calibration of the detected beam signal/intensity - stated in *total pixel count* - and the incoming photon number is required. Due to the low bunch charge at REGAE the photon number could be pretty low and therefore the EM-gain of the cameras is often used. The Andor iXon cameras have a so called *Real-Gain Mode*. The gain of the signal should be proportional and the adjusted gain should be identical with the real magnification of the signal. Means, a gain of 10 should amplify the signal by a factor of 10.

To measure the total pixel count of a signal, images for different camera gains with the *Real Gain Mode* were taken and a linear fit has been used to determine the ungained pixel count. A measurement as well as the yielded result for the ungained signal are shown in Fig. 3.11. As an intermediate result the linearity of the gain mode and its Real-Gain function could be validated with this measurement. In order to calibrate the pixel count relative to the incoming number of photons the quantum efficiency of the CCD chip on the one hand and the pixel well depth on the other hand are needed. These parameters are given by the manufacturer (Tab. 3.1). For the given measurement the camera has been recording 16-bit images. Therefore a pixel count of $527\,889 \pm 85\,324$ has been detected. That is equal to $696\,644 \pm 128\,355$ photons. The measured bunch charge was (82 ± 1) fC. It was necessary to choose a comparably low charge because a large range of the gain should be scanned to perform a calibration like in Fig. 3.11. The resulting overall detector efficiency is **(1.4 ± 0.3) photon/e⁻**. This takes the scintillator conversion efficiency, the light optics geometry and transmission as well as the camera detection efficiency into account. The result is in good agreement with the estimated result. To measure reasonably and reliably the detector efficiency should not be below 1 photon/e⁻.

Due to the detector efficiency of D1 the fluctuations from shot-to-shot of the electron number is not negligible. A higher detector efficiency, meaning a higher conversion rate of electrons to photons, would reduce the shot noise of the signal created by a electron bunch drastically. The tremendous influence on the beam signal evaluation, if not well treated, will be shown in the next section.

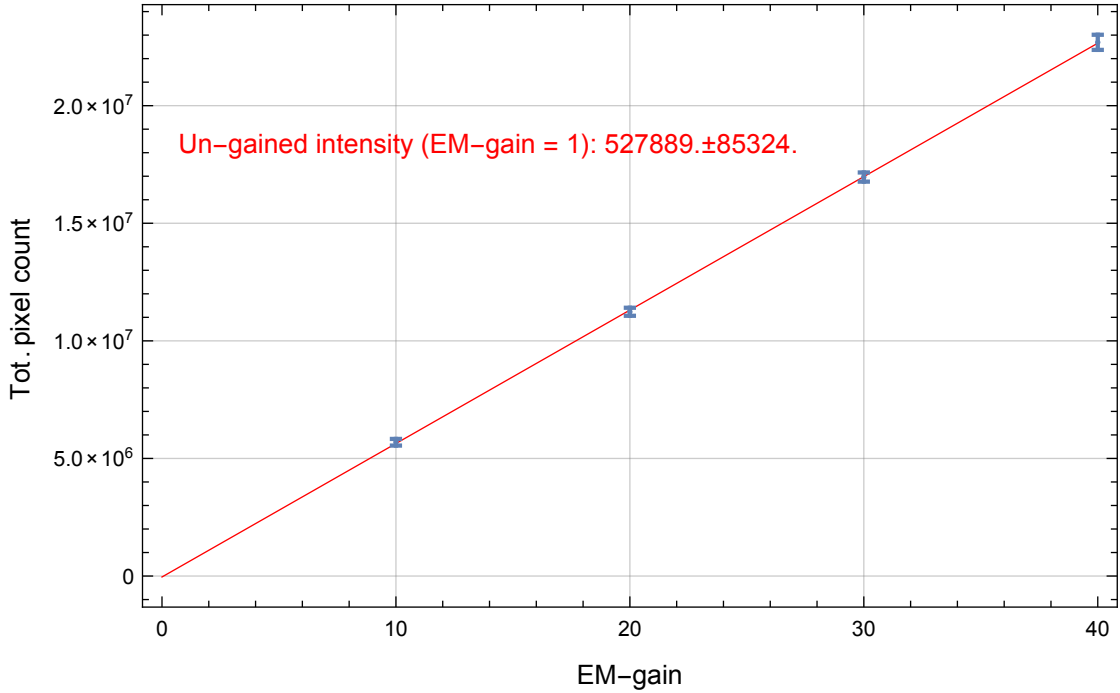


Figure 3.11: Extrapolation of the ungained intensity of the signal detected by the Andor iXon3 888. The Real-Gain mode has been used and shows a linear behavior. The fit (red, solid curve) yielded: $\text{Tot. pixel count} = -39529.6 + 567419 \times \text{EM-gain}$.

3.2 Image post-processing

For any kind of image-based beam diagnostics the noise and background signals are an issue which can have tremendous impact on the analysis of the beam signal. The relevant factor is the *signal-to-noise-ratio* (SNR). But sources of noise are manifold. In course of this thesis it is important to distinguish between the different sources. On the one hand there is the electrical noise generated by the

imaging device. In case of REGAE it is a high-sensitive EMCCD camera. There are several technical possibilities to reduce the electrical noise of an camera - in detail presented for the used camera in Sec. 3.1.1. On the other hand a fundamental source of noise is the *shot-noise*, meaning the *shot-to-shot* fluctuations of the electron number at a certain point or in case of an imaging diagnostic device at a certain pixel. On a taken image there are two signals. First, the signal from an accelerated and transported electron bunch - the required one. The second one is caused by electrons accelerated from a cavity but in an unintended way. High RF field gradients emit electrons from the inner cavity surface. The roughness of the surface leads to field exaltation and the emission of electrons. This signal is unwanted. It is called *dark current*. A small amount is always transported through a beamline and therefore overlaying with the very beam signal on a detector. Because it is independent of the bunch electron emission, it is easy to take background images and subtract them from images with a wanted beam signal. The majority of the dark current signal vanishes but the dark current is shot noise dominated thus the subtraction of background images generates additional noise. With high statistics the noise can be reduced but never vanishes. In the first subsection I take a closer look at the nature of the shot noise to understand and describe it. A post-processing routine for camera images based on an elementary analysis of the noise signal is introduced with the final aim to reduce the contribution of noise to the beam signal evaluation. This is of particular interest for the RMS calculations of emittance measurements done at REGAE. Due to the low bunch charge, especially compared to the dark current level, and the high-end imaging device shot noise is the dominant source of noise at REGAE's detector system.

The second subsection of this section will take a closer look at the RMS calculation of an image considering a beam signal overlaid with noise. And in particular an error estimation will be done to get an impression of the reliability and robustness of the introduced noise evaluation of the first subsection. Because noise limits the accuracy of any signal related evaluations which can be obtained from an image, it is important to know where are the limits and how can they be estimated?

The last subsection faces an experimental problem which occurs at REGAE's detector system D1. A distinct beam halo is observable on every image taken with the detector system. A full discussion of the origin and investigations of this halo will be done in the next section of this chapter. In the final subsection of this section only a method to handle images with a halo is introduced and illustrated.

3.2.1 Theoretical description of noise

The dominance of *shot noise* at REGAE's detector system D1 is depicted in Fig. 3.12. The principal noise level of the camera (upper row) is shown as well as the noise level introduced by the *dark current* (middle row). To illustrate the differences of these two sources it is useful to compare the pixel histograms of both - shown in the right plot in the last row. In this context a histogram visualize how many pixels with the same pixel value are included in a pixel array. As a reference the histogram of a normal distributed 'beam signal' is plotted as well. The basic difficulty regarding noise in images can be seen in this plot. The low intensity tails of the beam signal are overlaid with noise and it is not possible to distinguish between both. In case of a perfect Gaussian shaped beam profile a fit would help to derive the standard deviation which is - in this particular case - equal to the RMS width of the distribution. In any other case a direct calculation of the RMS (see Eq. 2.3) can be dominated - depending on the noise level - by the noise. Hence, a reliable post-processing routine to distinguish beam signal and noise based on basic assumptions to determine the RMS beam size precisely is desirable and aim of this subsection.

Such a routine can be developed by means of a theoretical description of the dominant noise source. The phenomenon of *shot noise* has been described by W. Schottky [58] in 1918. If the number of particles, which are individually excited (electrons from the surface of a cavity or photons from a cathode), is sufficiently small, the uncertainty of these independent random events can be described by a Poisson distribution like

$$f(k; \lambda) = \frac{\lambda^k e^{-\lambda}}{k!}. \quad (3.3)$$

$k \in \mathbb{N}$ is the number of electrons collected on a pixel of the image and λ is the expected value as well as the variance of the distribution. The relative signal variation can be defined as the expected value of the signal distribution divided by its width. The width is the square root of the variance of a distribution. In case of a Poisson distribution this variation is proportional to $\sqrt{\lambda}$. Therefore the variation of the signal depends on the square root of the expected value. In contrast, for a normal fluctuating signal it would be proportional to the expected value because the width is not called to the expected value.

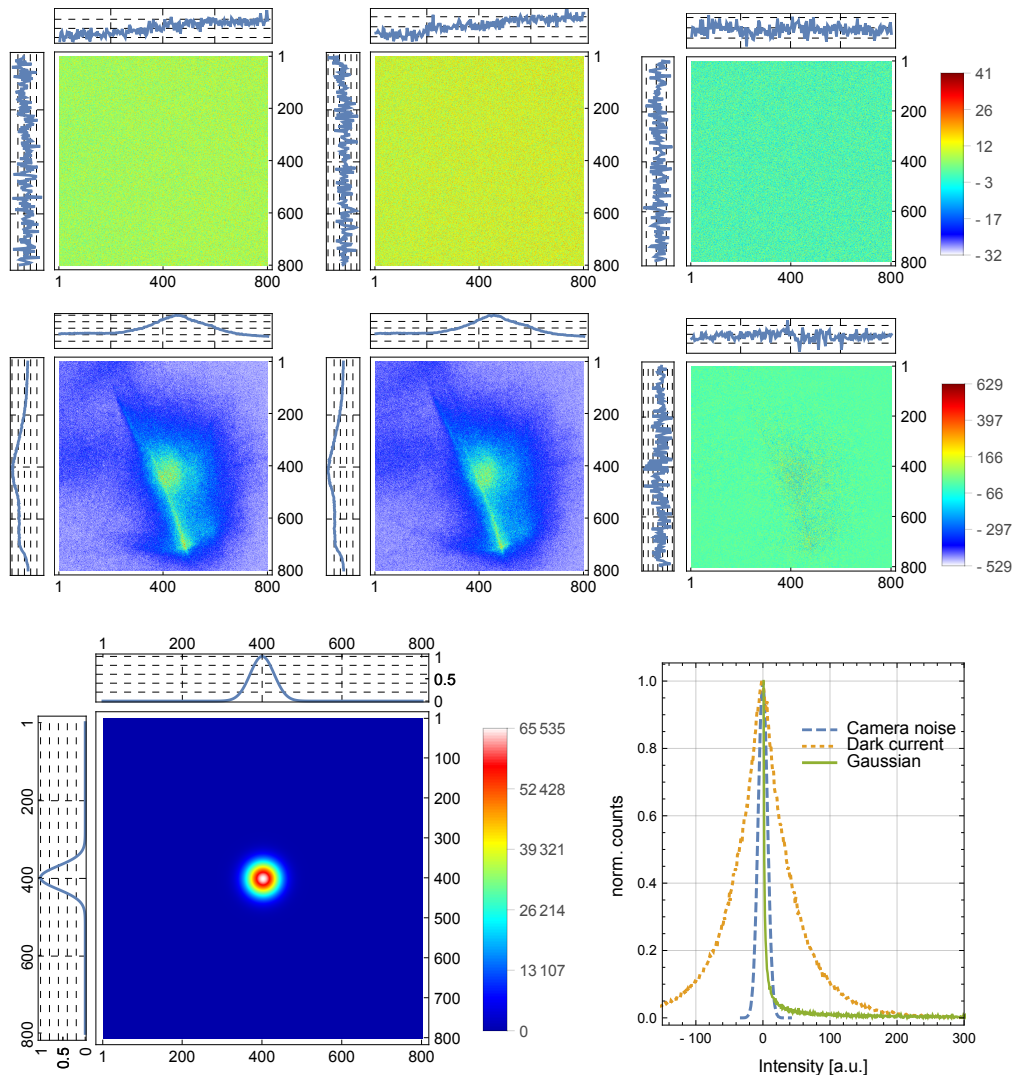


Figure 3.12: In the **first row** are noise images (left, middle) of the Andor iXon 888 camera shown. The camera is cooled down to -70°C . The images contain all kind of noise caused by the camera itself. The right image shows the difference of the first two. The **second row** is similar to the first. Here are two real background images shown. The 'signal' is *dark current*. The right image shows again the difference of the left and middle. The remaining structure is *shot noise* caused by the dark current. In the **third row** the left plot shows an artificial normal distributed beam profile. The right plot shows the histograms of the Gaussian distribution as well as of the two difference plots of the first and second row.

Considering the subtraction of a background image from a beam signal image means: subtracting two Poisson-distributed pixel images. The beam image of course contains the desired signal but it occupies just a small fraction of the whole image. The larger part is still background dominated. Considering just a single pixel, the difference of two Poisson-distributed pixel can be described by a so called Skellam distribution [59] and is defined as

$$p(k_S; \lambda_1, \lambda_2) = e^{-(\lambda_1 + \lambda_2)} \left(\frac{\lambda_1}{\lambda_2} \right)^{k_S/2} I_{k_S} \left(2\sqrt{\lambda_1 \lambda_2} \right), \quad (3.4)$$

where λ_1 and λ_2 are related to the two Poisson distributions and $I_{k_S} (2\sqrt{\lambda_1 \lambda_2})$ is the modified Bessel function of the first kind. k_S is in contrast to the Poisson distribution element of \mathbb{Z} . To illustrate the Skellam distribution of Eq. 3.4 the *probability mass functions* (PMF) for different pairs of λ_1 and λ_2 are plotted in Fig. 3.13. The expected value of a Skellam distributed PMF is $\lambda_1 - \lambda_2$ and its variance is $\lambda_1 + \lambda_2$.

For the purpose of demonstration it is worth to mention a different utilization of the Skellam distribution. In the context of image post-processing, e.g. by Y. Hwang et al. [60], the Skellam distribution could be used to determine sharp edges in photos. The difference of two images reveals a drastic change of the noise intensity at sharp edges which corresponds to a drastic change in the photo intensity as well. This demonstration impressively shows how much information is contained in the noise of images. Therefore, the Skellam distribution is a well known and used distribution to describe the difference of two shot noise dominated images. In the context of this work it will be used to distinguish between noise and the wanted beam signal. And consequently validate the noise level and determine a profound intensity cut in order to reduce the noise level.

For two Poisson distributed pixels of the signal and background image the assumption $\lambda_1 = \lambda_2$ should hold because they have the same source - pixels, dominated by a wanted signal, are excluded of course. In the following λ will replace λ_1 and λ_2 . Consequently the variance is equal to 2λ .

Although the Skellam distribution describes the nature of the generated noise very well, it is unpractical to integrate it into an automatized post-processing routine. The intended fit routine to determine the parameters of the Skellam distribution is comparably slow. But another assumption, supported by the middle row and the histogram of the background noise of Fig. 3.12, can be made if λ is comparably large. For $\lambda \gtrsim 30$ a Poisson distribution tends to a normal distribution and conse-

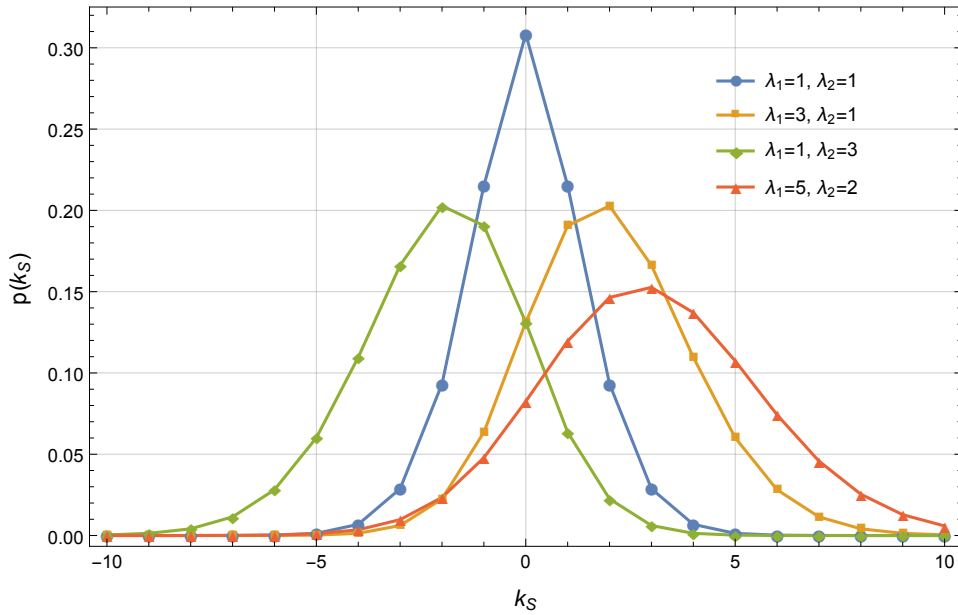


Figure 3.13: Shown are PMFs for different pairs of λ_1 and λ_2 for $k_S \in \mathbb{Z}$. (The lines are not indicate continuity.)

quently the difference of two normal fluctuating images yields a normal distributed noise distribution. The corresponding normal distribution can be formulated as

$$f(k_S; \lambda) \sim \frac{e^{-k_S^2/4\lambda}}{\sqrt{4\pi\lambda}}, \quad (3.5)$$

where λ is equivalent to the already introduced λ of the Skellam distribution. The standard deviation of a normal distribution is equal to the square root of the variance thus the standard deviation in this particular case is $\sqrt{\lambda}$. This assumption works pretty well for 14- or 16-bit images, where the pixel depth is high. For lower pixel depths a Skellam distribution is probably more suitable.

The made assumptions are reasonable but again the found simplification of Eq. 3.5 just holds for single pixels. To get a significant sample number hundreds of images would be necessary. But the used camera has a megapixel CCD, hence the subtraction of two images contains one million pixel. Even if a fraction is occupied by the beam signal the statistic would be more than sufficient. Of course it is just valid as long as all λ_i ($i = 1 \dots N$; N : Number of pixels) just slightly differ. The middle row of Fig. 3.12 is a good example where this assumption not holds. There is a clearly remaining structure created by the dark current signal in the noise image (middle

row, right). Therefore the histogram shows not a normal distributed noise contribution but instead a superposition of several normal distributed noise signals all contained in one image. Empirically proved it seems reasonable to describe such a distribution by a sum of two normal distributions like

$$f(k_S) = A_1 \sqrt{2\pi} \sigma_1 e^{-(k_S - \mu_1)^2 / (2\sigma_1^2)} + A_2 \sqrt{2\pi} \sigma_2 e^{-(k_S - \mu_2)^2 / (2\sigma_2^2)}, \quad (3.6)$$

where A_i are the amplitudes, μ_i the expected values and σ_i the standard deviations. The histogram of Fig. 3.14 shows the fit of a subtraction of a beam signal image and a background image using the introduced function of Eq. 3.6. The noise is centered at zero that confirms $\lambda_{i,1} = \lambda_{i,2}$. Due to the presence of a beam signal the intensity distribution is not symmetric anymore. Therefore only the red colored data points has been used for the fit. The deviation of the taken data and the fit at the right flank of the histogram shows the contribution of the beam signal to the pixel histogram.

Nevertheless this description of the noise contained in an image can be used to

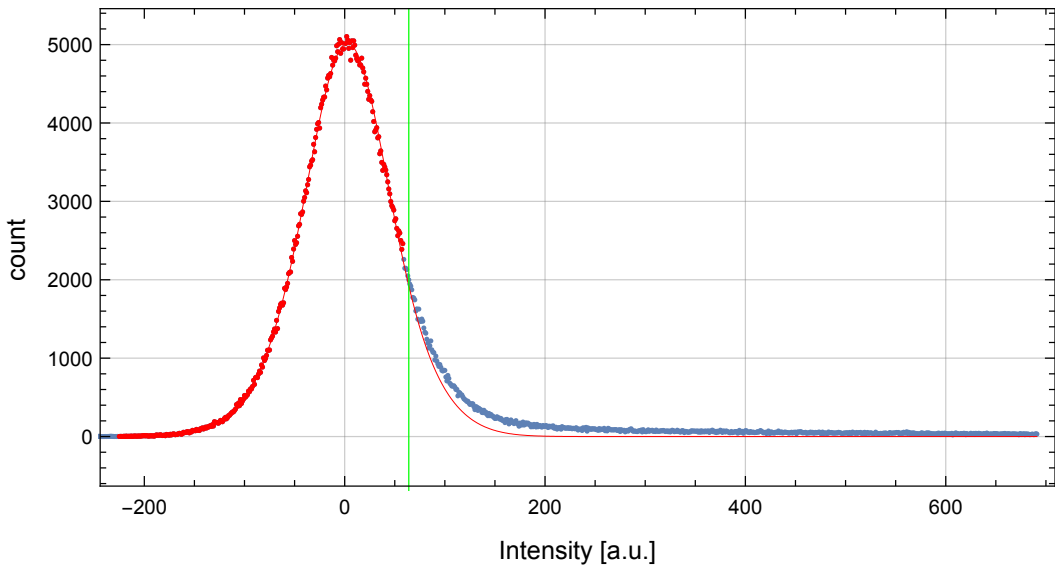


Figure 3.14: Histogram of pixel intensity (blue dots). Red dots were used for double Gaussian fit. The green line marks the cut-off value k_{cut} (90%-cut).

define a reasonable and reproducible cut-off of the noise for not only any kind of

shot noise dominated but also for any kind of normal distributed noise dominated images. This cut-off is illustrated by the green line in Fig. 3.14. For every pixel below this threshold it is not possible to distinguish between noise and beam signal. For pixel values above the cut-off there are still noise dominated pixels, but their contribution to the whole signal is much smaller.

Before discussing the optimal threshold the efficiency of this routine will be depicted. In Fig. 3.15 an example of an artificial Gaussian beam profile overlaid with a real background/noise image taken at REGAE is shown. To illustrate the capability of the post-processing routine the amplitude of the Gaussian beam profile has been chosen to be comparably low. The added dark current signal is the same as in Fig. 3.12 (middle, left). The post-processing has been applied like described. Another background image has been subtracted (Fig. 3.12, middle row, middle). Then the intensity cut-off threshold k_{cut} has been determined from the histogram of the background subtracted image. In order to improve the calculation of the first and second moments (barycenter and RMS) a region of interest (ROI) from a first RMS estimation of the image has been defined. Such a routine has been already introduced in [35, 61]. The ROI can be clearly seen in the right plot of Fig. 3.15. The results, shown in Tab. 3.4, are promising. Considering the poor signal-to-noise ratio and poor statistic of images - normally, several images with and without beam signal are taken and subtracted - the accuracy of the reconstructed moments is good.

Speaking of noise, the beam signal itself is dominated by shot noise as well and has to be taken into consideration. To reduce the uncertainties of the beam signal it is necessary to increase the statistic. Assuming the machine runs stable for several shots, it is valid to take multiple images and average them. In addition several background images should be taken and averaged as well to reduce statistical errors. The statistical error is proportional to $1/\sqrt{N}$ where N is the number of samples.

In summary, it could be shown that the post-processing routine depends only on general assumptions of the nature of the noise and is capable of automatically analyze and reduce the noise level of shot noise dominated beam signal images. At the same time it has a high reliability.

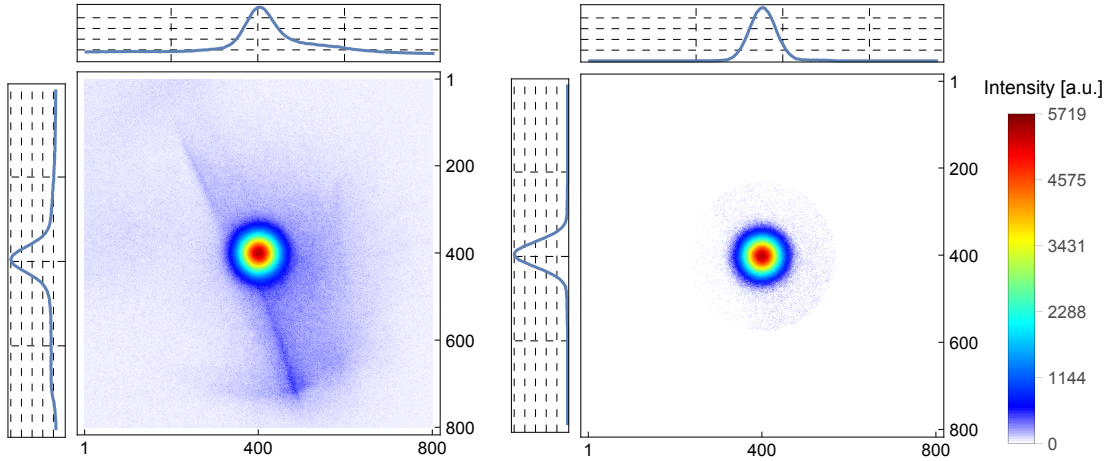


Figure 3.15: **Left:** Background image from Fig. 3.12 has been added to an artificial Gaussian beam profile. **Right:** Same beam profile after applying whole post-processing routine.

Table 3.4: Theoretical and post-processed barycenter (1st moment) and RMS (2nd central moment) of a Gaussian beam profile (Fig. 3.15). The moments are given in pixel.

Mode	x_{rms}	y_{rms}	x_{mean}	y_{mean}
theoretical	30	30	400	400
w/o post-processing	179.9	187.3	407.4	414.7
w/ post-processing	33.4	34.0	401.4	400.7

3.2.2 Estimation of RMS error due to intensity cuts

An intensity cut off always affects a part of the wanted beam signal as well and hence introduces a systematic error to the RMS calculation. To get a profound impression how noise falsifies the RMS calculation an estimation of the induced error is performed.

In order to find an analytical description some assumptions for the signal as well as for the noise are necessary:

1. The noise is homogeneously distributed over the full-range of the image.
2. The beam signal is normal distributed.

The aim is to find the 'optimal' intensity cut for a given beam image.

The intensity cut of a normal distributed signal confines it to an elliptical area, called *region of interest* (ROI) in the following. A study, how a well defined but arbitrary ROI falsifies a RMS calculation has already be done by myself in [35] and ultimately based on [62]. Some results will be used in the following. Concluding already achieved results and new assumptions lead to the following definition of parameters:

$\sigma_{x,y}$: standard deviations of the 2D normal distributed beam signal

$a_{x,y}$: Half-axes of ROI

c : Scaling variable of ROI ($a_{x,y} = c \cdot \sigma_{x,y}$)

$P(c)$: Integrated signal fraction lying inside ROI depending on c

$\rho(\theta)$: Arbitrary point on an ellipse in polar coordinates

$P(c)$ and $\rho(\theta)$ are defined as follows:

$$P(c) = 1 - e^{-c^2/2}, \quad (3.7)$$

$$\rho(\theta) = \frac{c}{\sqrt{\frac{\cos^2 \theta}{\sigma_x^2} + \frac{\sin^2 \theta}{\sigma_y^2}}}. \quad (3.8)$$

In addition it is necessary to transform a centered 2D normal distribution like

$$S(x, y) = S_{\max} \exp\left(-\frac{x^2}{2\sigma_x^2} - \frac{y^2}{2\sigma_y^2}\right) \quad (3.9)$$

with S_{\max} as the amplitude into polar coordinates to calculate the RMS of $S(x, y)$. Introducing $\rho(\theta)$ (Eq. 3.8) and the scaling factor c into Eq. 3.9 yields

$$S(r, \theta) = S_{\max} \exp\left(-\frac{c^2 r^2}{2\rho(\theta)^2}\right). \quad (3.10)$$

These definitions will be of interest below.

The indicator to judge the quality of an intensity cut is the ratio of the calculated RMS value and the known RMS or standard deviation of a given normal distributed signal

$$\frac{x_{\text{RMS}}}{\sigma_x}.$$

It will be shown that this ratio only depends on the *signal-to-noise-ratio* (SNR) of the image and the choice of the intensity cut.

The SNR is an important quantity in the field of signal analysis. Depending on the source of noise and technical applications, different definitions of the SNR can be found. In the course of this study it is defined as

$$\text{SNR} = \frac{\text{signal amplitude}}{\text{noise level}}. \quad (3.11)$$

The *noise level* will be identified by the standard deviation of the noise distribution, already introduced in Eq. 3.5 as $\sqrt{\lambda}$. With the *signal amplitude* S_{\max} Eq. 3.11 can be written as

$$\text{SNR} = \frac{S_{\max}}{\sqrt{\lambda}}. \quad (3.12)$$

λ is a result from the noise distribution fit in the course of the intensity cut routine. In a measurement the real signal amplitude, however, is not accessible because the signal is always overlaid with noise. For large SNR the assumption that the maximum pixel value is equivalent to S_{\max} is a good approximation.

As described in the previous subsection the noise distribution can be approximated via the Skellam function which tends to a normal distribution for large expectation values λ . Hence, the noise distribution can be described as

$$g(k) = B \exp\left(\frac{-k^2}{4\lambda}\right) \quad (3.13)$$

with B as its amplitude and λ as the variance and consistently $\sqrt{\lambda}$ as the standard deviation. $g(k)$ is assumed to be centered at zero.

The intensity cut itself can be freely chosen, the cut value will be called k_{cut} . It is helpful to connect it with a more meaningful quantity. Here, the relative integrated noise intensity q of the total integrated noise intensity I_{tot} will be used. It is defined as

$$q = \frac{\int_{-\infty}^{k_{\text{cut}}} g(k) dk}{I_{\text{tot}}} \quad \text{with} \quad I_{\text{tot}} = \int_{-\infty}^{\infty} g(k) dk. \quad (3.14)$$

Now an expression for the cut-off intensity k_{cut} can be obtained by solving Eq. 3.14 which yields

$$\begin{aligned} k_{\text{cut}}(\lambda, q) &= 2\sqrt{\lambda} \text{InvErf}(2q - 1) \\ &= 2\sqrt{\lambda} C_1(q) \quad \text{with} \quad C_1(q) = \text{InvErf}(2q - 1), \end{aligned} \quad (3.15)$$

where InvErf is the *inverse error-function*. Due to the nature of the normal distribution $k_{\text{cut}}(\lambda, q)$ tends to infinity for $q \rightarrow 1$ and to minus infinity for $q \rightarrow 0$. Therefore the relative integrated noise intensity q will be only defined in the domain $(0, 1)$.

The remaining noise contributes to the calculation of the RMS value. If the remaining noise is assumed to be homogeneously distributed over the ROI, its expectation value can be added as an offset to the signal $S(x, y)$. The expectation value of the noise contained in the ROI, denoted as N_{cut} in the following, is given by the expectation value λ_r of the remaining noise distribution and can be written as

$$N_{\text{cut}}(\lambda, q) = (1 - q) \lambda_r(\lambda, q). \quad (3.16)$$

The expectation value λ_r (1st central moment) is required and can be found to be

$$\begin{aligned} \lambda_r(\lambda, q) &= \frac{\int_{k_{\text{cut}}}^{\infty} k g(k) dk}{\int_{k_{\text{cut}}}^{\infty} g(k) dk} \\ &= 2 \sqrt{\lambda/\pi} \frac{\exp(-C_1(q)^2)}{\text{Erfc}(C_1(q))} \\ &= 2 \sqrt{\lambda/\pi} C_2(q) \quad \text{with} \quad C_2(q) = \frac{\exp(-C_1(q)^2)}{\text{Erfc}(C_1(q))}. \end{aligned} \quad (3.17)$$

The RMS (2nd central moment) of an image including beam signal (Eq. 3.9) and noise (Eq. 3.16) can be calculated as follows

$$x_{\text{RMS}}^2 = \frac{\int_{-\infty}^{\infty} \int_{-\infty}^{\infty} x^2 (S(x, y) + N_{\text{cut}}(\lambda, q)) dx dy}{\int_{-\infty}^{\infty} \int_{-\infty}^{\infty} (S(x, y) + N_{\text{cut}}(\lambda, q)) dx dy}. \quad (3.18)$$

To solve Eq. 3.18 it is convenient to switch to Polar coordinates. Additionally Eq. 3.7, Eq. 3.8 and Eq. 3.10 have to be introduced. Instead of the integration over infinity it is now limited to the ROI and Eq. 3.18 yields

$$\begin{aligned} x_{\text{RMS}} &= \frac{\int_0^{2\pi} \int_0^{\rho(\theta)} r^3 \cos^2 \theta (S(\rho', \theta) + N_{\text{cut}}(\lambda, q)) dr d\theta}{\int_0^{2\pi} \int_0^{\rho(\theta)} r (S(r, \theta) + N_{\text{cut}}(\lambda, q)) dr d\theta} \\ &= \sigma_x^2 \frac{S_{\text{max}} \left(P(c) - \frac{c^2}{2} \exp\left(-\frac{c^2}{2}\right) \right) + \frac{1}{8} c^4 N_{\text{cut}}(\lambda, q)}{S_{\text{max}} P(c) + \frac{c^2}{2} N_{\text{cut}}(\lambda, q)} \end{aligned} \quad (3.19)$$

and the relative RMS error is consequently obtained as

$$\frac{x_{\text{RMS}}^2}{\sigma_x^2} = \frac{S_{\text{max}} \left(P(c) - \frac{c^2}{2} \exp\left(-\frac{c^2}{2}\right) \right) + \frac{1}{8} c^4 N_{\text{cut}}(\lambda, q)}{S_{\text{max}} P(c) + \frac{c^2}{2} N_{\text{cut}}(\lambda, q)}. \quad (3.20)$$

It depends on the signal amplitude S_{\max} , the noise expectation value λ (Eq. 3.13), the relative integrated noise intensity q and the ROI scaling variable c . To reduce the dependencies it is worth to take a closer look at c . Because $k_{\text{cut}}(\lambda, q)$ determines an elliptical ROI for the total signal $S(x, y) + N_{\text{cut}}(\lambda, q)$ the scaling variable c is not arbitrary anymore. It can be easily determined with $a_x = c\sigma_x$ where a_x is the horizontal half-axis of the ROI and σ_x the horizontal standard deviation of the beam signal.

$$\begin{aligned}
 S(a_x, 0) + N_{\text{cut}}(\lambda, q) &= k_{\text{cut}}(\lambda, q) \\
 S_{\max} \exp\left(-\frac{a_x^2}{2\sigma_x^2}\right) + N_{\text{cut}}(\lambda, q) &= k_{\text{cut}}(\lambda, q) \\
 \Rightarrow a_x = \sigma_x \sqrt{-2 \ln\left(\frac{k_{\text{cut}}(\lambda, q) - N_{\text{cut}}(\lambda, q)}{S_{\max}}\right)} \\
 \Rightarrow c(S_{\max}, \lambda, q) = \frac{a_x}{\sigma_x} &= \sqrt{-2 \ln\left(\frac{k_{\text{cut}}(\lambda, q) - N_{\text{cut}}(\lambda, q)}{S_{\max}}\right)}. \tag{3.21}
 \end{aligned}$$

Using the definition of the SNR (Eq. 3.12) to simplify Eq. 3.20 and Eq. 3.21 they yield:

$$\frac{x_{\text{RMS}}^2}{\sigma_x^2} = \frac{C_3(q) \text{SNR} \left(P(c) - \frac{c^2}{2} \exp\left(-\frac{c^2}{2}\right) \right) + \frac{c^4}{8}}{C_3(q) \text{SNR} P(c) + \frac{c^2}{2}}, \tag{3.22}$$

$$c(\text{SNR}, q) = \sqrt{-2 \ln\left(\frac{C_4(q)}{\text{SNR}}\right)} \tag{3.23}$$

with

$$\begin{aligned}
 C_3(q) &= \frac{\sqrt{\pi}}{2 C_2(q) (1 - q)}, \\
 C_4(q) &= 2 C_1(q) - C_3(q)^{-1}.
 \end{aligned}$$

Now the relative RMS error (Eq. 3.22) only depends on the SNR and the relative integrated noise intensity q .

The assumed, simplified model has some logical and consequently mathematical limits. An intensity cut k_{cut} smaller than N_{cut} is meaningless. Mathematically spoken, $c(\text{SNR}, q)$ (Eq. 3.23) is no longer real. It is only real for

$$\frac{C_4(q)}{\text{SNR}} > 0.$$

SNR is per definition positive so that $C_4(q)$ has to be positive. In case $N_{\text{cut}} > 0$ the lower limit of q can be numerically approximated. $C_4(q)$ and the lower limit are shown in Fig. 3.16, left.

For q tending to q_{min} , c and consequently the ROI are tending to infinity. Intro-

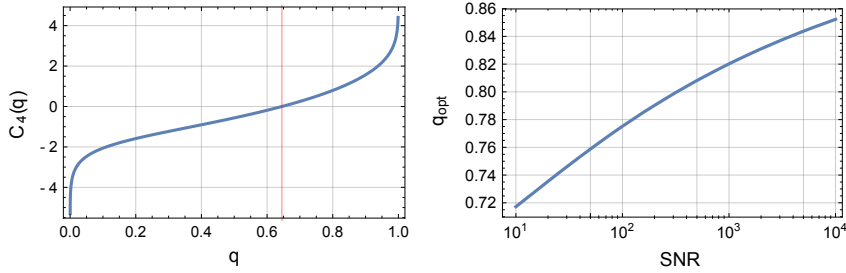


Figure 3.16: **Left:** $C_4(q)$ (blue) plotted for whole interval $(0, 1)$ of the relative integrated noise intensity q . The minimal q_{min} can be numerically determined. It is marked by the red vertical line and is approximately **0.6451**. **Right:** The optimal relative integrated noise intensity q_{opt} depending on SNR.

ducing $c \rightarrow \infty$ to Eq. 3.22 the relative RMS error tends to infinity or x_{RMS} tends to infinity. This is consistent with the definition of the RMS (Eq. 2.3) assuming the signal is not falling to zero for $x \rightarrow \infty$. A special case which illustrates the consistency of the used model is given by $N_{\text{cut}} = 0$, means no noise. Following the former logic $k_{\text{cut,min}} = 0$ and $q_{\text{min}} = 0.5$. Introducing $k_{\text{cut,min}}$, q_{min} and $c \rightarrow \infty$ to Eq. 3.22 leads to

$$\frac{x_{\text{RMS}}}{\sigma_x} \rightarrow 1.$$

x_{RMS} tends to the standard deviation σ_x of the signal $S(x, y)$.

Furthermore the optimal relative integrated noise intensity q_{opt} can be determined from Eq. 3.22. It is a rather hypothetical consideration. To achieve $x_{\text{RMS}}/\sigma_x = 1$ the intensity cut value k_{cut} has to be chosen in a way that the remaining noise compensates the cut off signal. But obviously this requires that the assumptions of the noise distribution are fulfilled. In a real measurement this is unlikely but nevertheless it gives an impression for reasonable q values. q_{opt} is plotted in dependence of SNR in Fig. 3.16, right.

In Fig. 3.17 the relative RMS error is depicted for a larger range of parameters. x_{RMS}/σ_x is shown for different SNR as well as certain q parameters. For large SNR the RMS error tends to zero what is an obvious but important realization. For the

REGAE experiment it implies to maximize the SNR for every measurement which is feasible with the camera gain. Especially, the Andor cameras have a decent and well behaving camera gain.

For some values of the relative integrated noise intensity q the RMS error can be over- or underestimated. To avoid this and be able to make a clearer prediction of the RMS error, it is advisable to choose $q > 0.8$. Then the RMS beam size is always underestimated and consequently the emittance depending on the RMS beam size will be always slightly underestimated. For all following post-processed images or related beam size determinations $q = 0.9$ has been chosen. This compromise has worked nicely for all applications. Furthermore a $\text{SNR} > 10^3$ should be always the aim to keep the RMS error on a percent level.

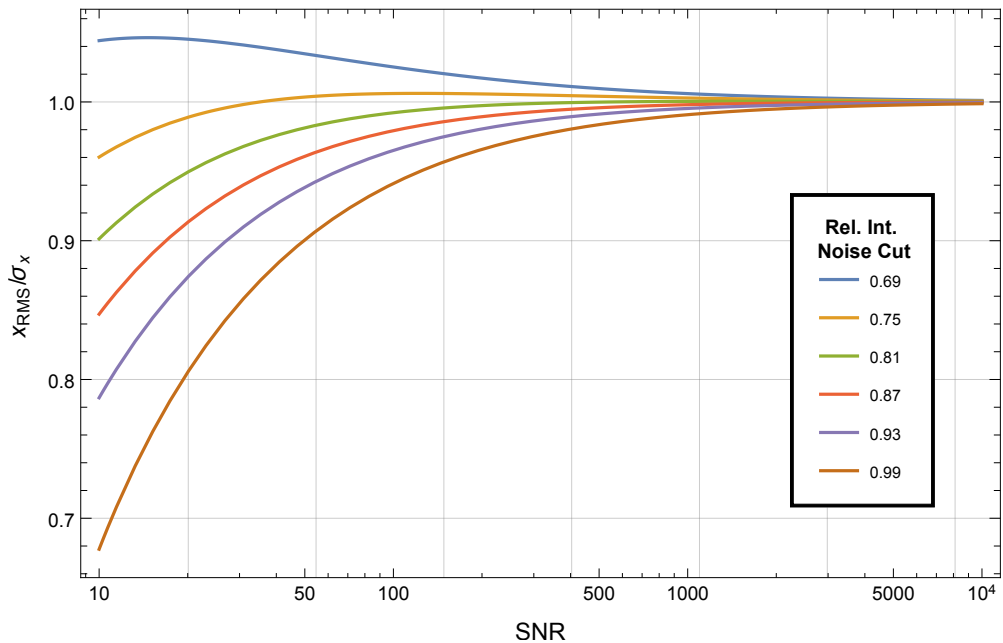


Figure 3.17: The relative RMS error (x_{RMS}/σ_x) for a few specific values of the relative intensity noise cut q depending on *signal-to-noise-ratio* (SNR).

3.2.3 Beam halo at the REGAE detector D1

During the machine operation of REGAE we had to face a broad and distinct halo which can be clearly seen with our detector system. An example is shown in

Fig. 3.18.

The effect of this halo on diffraction experiments is small. For a diffraction

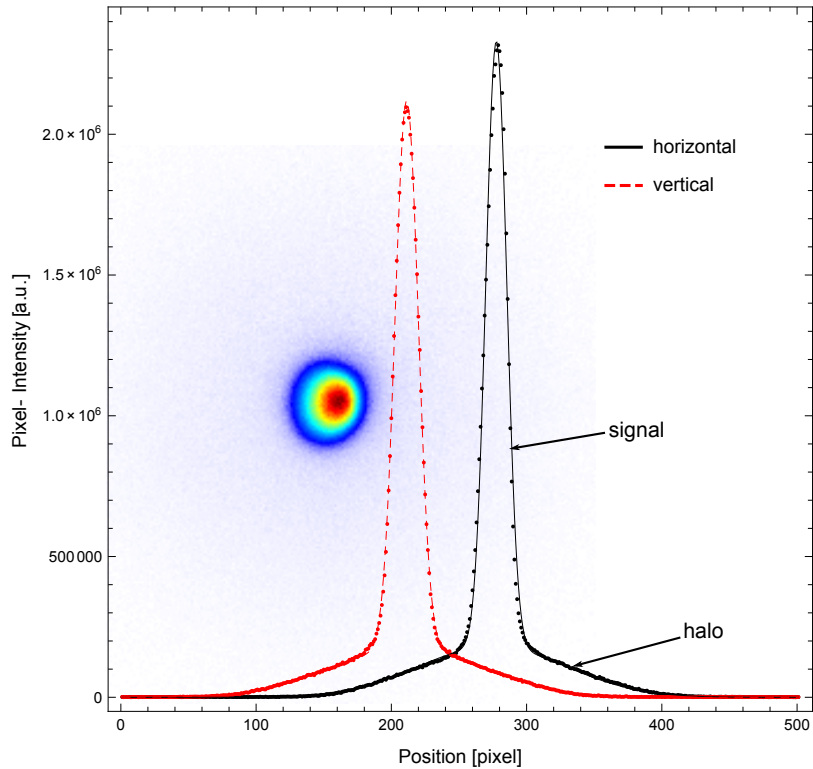


Figure 3.18: Measured beam profile at REGAE - projections and 2D-colored profile. Double Gaussian fits (solid lines) has been applied.

pattern the geometry of the pattern and not the distribution of each point or line matters. Just if the beam quality is too poor it influences the quality of a diffraction pattern. Therefore, even if the broad beam profile would be real the peaked part of the beam has a high beam quality (or small emittance, respectively) and good results can be achieved.

In contrast, for any kind of beam dynamic studies like an emittance measurement the halo has a tremendous impact. It will be shown that the halo is artificial and caused by the detector system. In order to use the taken data an intensity cut has been applied before using the images for further evaluations. Due to the cut RMS values are most likely underestimated. This fact has to be kept in mind for all measurements.

The halo as well as the 'peak on top' can be described by the superposition of two

Gaussian distributions:

$$f(x) = a_1 \exp\left(-\frac{(x - \mu_1)^2}{2\sigma_1^2}\right) + a_2 \exp\left(-\frac{(x - \mu_2)^2}{2\sigma_2^2}\right). \quad (3.24)$$

a_i is the distribution's amplitude, μ_i describes the barycenter and σ_i the standard deviation (or 2nd central moment) of each distribution for $i = 1, 2$.

The aim is to use only the peaked Gaussian profile for an emittance measurement. Eq. 3.24 is used to fit the beam profile of an image to determine the intensity cut for a complete series of images taken during an emittance measurement. This is valid as long as the total intensity of the beam signal reaches the camera for all magnet settings during the scan - that should be given anyway. The beam profile images near the beam size minimum are preferred to determine the cut intensity due to the high SNR. The intensity cut is defined as the integrated intensity of the first Gaussian distribution:

$$I_{\text{cut}} = \int_{-\infty}^{\infty} a_1 \exp\left(-\frac{(x - \mu_1)^2}{2\sigma_1^2}\right) dx,$$

assuming a_1 , μ_1 and σ_1 are the parameters of the peaked Gaussian distribution. From the cut-off applied images the RMS beam size can be calculated and used for the emittance determination.

This routine is illustrated in Fig. 3.19. A measured beam profile is shown. It is generated from 10 images containing beam signal and 10 background images which has been subtracted. To reduce the noise and to determine the RMS beam size the introduced post-processing routine (Sec. 3.2.1) has been applied. After that a double Gaussian fit has been performed and the cut off intensity determined. The obtained RMS beam size from the post-processed and the intensity cut image as well as the standard deviation of the double Gaussian fit are summarized in Tab. 3.5. The intensity cut results are underestimate indeed the standard deviation. But the agreement of the peaked standard deviation and the RMS is good and much more realistic than the results obtained from the post-processed image taking the beam halo into account.

In the next section the origin of the halo will be explained and consequently the intensity cut-off introduced in this section will be confirmed.

Table 3.5: RMS beam size evaluations of a post-processed typical beam image (Fig. 3.19). The left plot shows the average of 10 beam signal images and 10 subtracted background images. Three different methods are used to evaluate the RMS. **1.** A double Gaussian fit has been applied to the beam projections. $\{\sigma_1, \sigma_2\}$ are listed. The beam signal is represented by σ_1 . **2.** The RMS of the whole image has been calculated. **3.** From the Gaussian fit in **1.** the integrated intensity I_{cut} of the halo has been used to apply a cut. The resulting beam profile is shown in the right plot.

Dimension	Gaussian fit	Full Image	PostPro Image
x_{rms} [pixel]	{8.24, 56.0}	26.5	7.73
y_{rms} [pixel]	{9.48, 58.8}	27.1	8.72

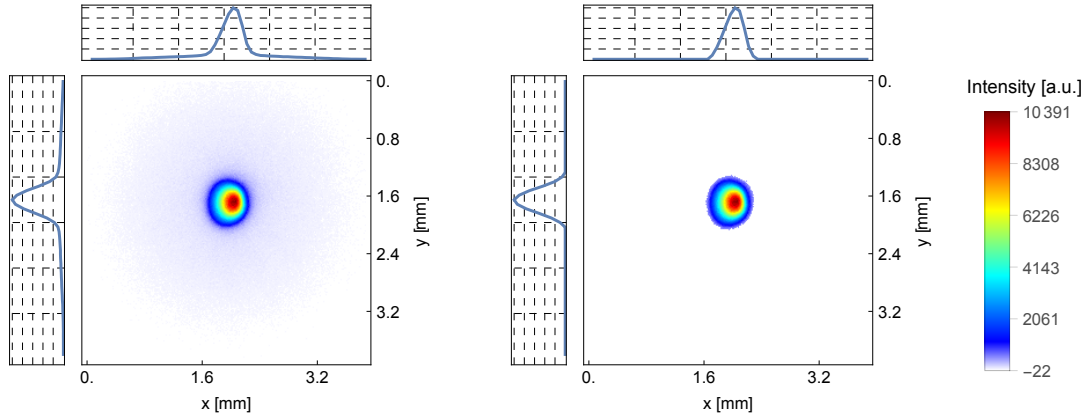


Figure 3.19: **Left:** Measured 2D-beam profile at REGAE. **Right:** Same beam profile after applying an intensity cut-off. RMS calculation and Gaussian fit results in Tab. 3.5.

3.3 Investigation of beam halo

As already mentioned the distinct beam halo is a massively disturbing beam profile feature for any kind of beam dynamic investigations or measurements. It blows up the measured beam size and consequently increases the resulting emittance. Therefore it is essential and inevitable to investigate the source of the halo. If the halo is indeed an artifact of the detector the performance of the machine

would be much better and much closer to design parameters as concluded from measurements taking the halo into account.

In this section three approaches are presented to get to the bottom of the halo. A major cause of a real double Gaussian distributed beam profile would be the transverse laser profile at the cathode. But another fact objects this: the halo is visible on each taken beam profile over the last four years no matter how the machine or the laser parameters at the cathode have been set up. There is not a single image where it is not observable. Therefore it seems implausible that the halo is laser related. To avoid any other real source for the halo, initially a beam based approach has been pursued which indeed indicates that the halo has to be an artifact. But the results are not unambiguous and they do not explain the origins of the halo.

In a next step all machine related sources have been eliminated by setting up a measurement of the D1 detector system in the laboratory. As an electron source two different radioactive β^- -sources have been used. For the stronger β^- -source a broad beam profile is indeed visible but it is not as distinct as a typical beam profile at REGAE. For this reason Monte Carlo simulations of the electromagnetic interaction of the electrons passing the FOS have been performed. They will be presented in the third subsection of this section. In the end there are a lot of strong indications that the beam halo at the detector system D1 has to be an artifact.

3.3.1 Beam based investigations

The first approach to determine the source of the beam halo is a beam based measurement. The idea is to confine the beam size at a certain position to a known value by means of the beam collimators at DDC1 or DDC2 (Fig. 1.1 or Fig. 1.2). From an emittance measurement beam parameters at the position of the solenoid used for the emittance scan can be determined. Now the beam size at the position of the collimators can be calculated with the envelope equation (Eq. 2.22). If the full, broad beam profile does not fit through the collimator the beam halo could not be a real part of the measured beam profile.

Since the beam transfer through the buncher cavity cannot be expressed in an analytical expression and the collimators downstream of the buncher cavity are used the buncher cavity as a possible reason to generate a halo can be excluded as well. The collimators at DDC2 have been used to confine the maximum beam size. An emittance scan with Sol67 has been performed with a kinetic mean beam

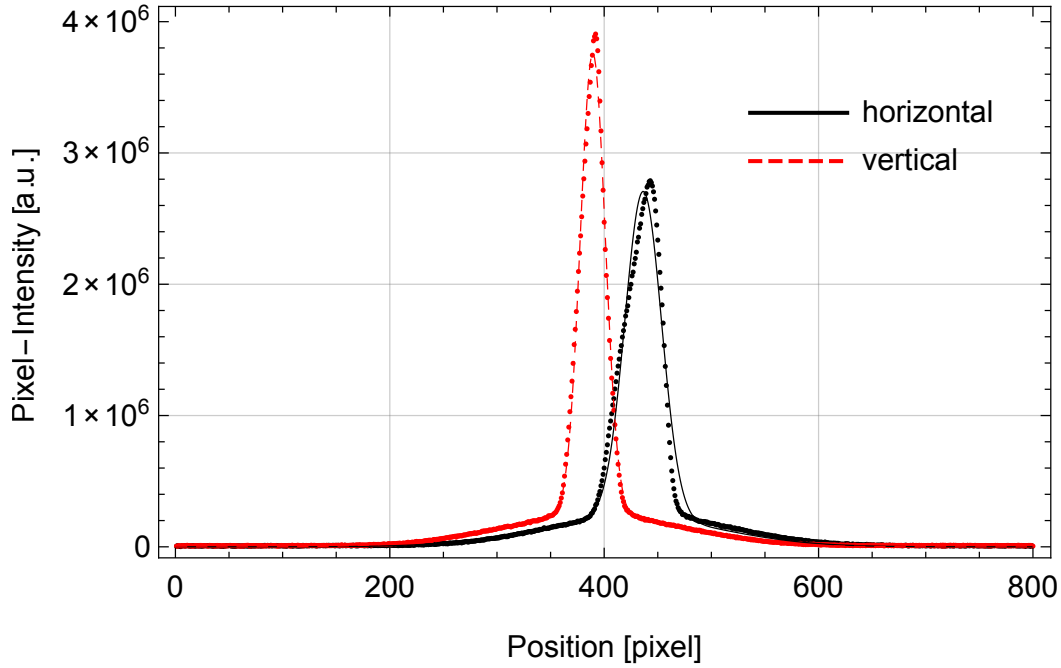


Figure 3.20: Horizontal and vertical beam profile (dots) and fitted double Gaussians (solid) at D1.

energy of 3.16 MeV and a bunch charge of 46.9(6) fC. The scan is evaluated for the peaked as well as for the broad part of the taken beam profiles. A double Gaussian function (see Eq. 3.24) can be fitted to the beam projections. The fitted standard deviations have been used for the emittance determination. Projections of the beam profile are shown in Fig. 3.20. The double Gaussian profile can be clearly identified. The emittance fit and the corresponding results are shown in Fig. 3.22 and Tab. 3.6, respectively. Introducing x_{RMS} , $(x_{\text{RMS}})'$, $\epsilon_{n,\text{RMS}}$ and the transfer matrix of a drift (Eq. 2.19) to Eq. 2.22 allows to calculate and plot the beam envelope from the solenoid to the position of the collimator at DDC2 (Fig. 3.21). The RMS beam size at the collimator is 0.32(2) mm and 1.50(3) mm for the peaked and broad part of the diagnosed beam, respectively. The diameter of the collimator was $d = 1.1$ mm. For the scan the collimators have been used to clip a huge amount of the bunch charge to shape the beam transversely and improve the transverse beam quality, meaning decreasing the transverse beam emittance. Therefore the passed beam profile was probably close to a uniform or flattop profile. But the largest achievable RMS beam size directly behind a collimator is reached with

a flattop beam profile hitting the collimator in the front or in good approximation with a normal distributed beam much larger than the collimator's diameter. The maximal achievable beam size for a 1.1 mm collimator diameter is 0.318 mm what almost perfectly matches the calculated beam size of the analytically backtracked beam from the solenoid. Consequently it is absolutely plausible that the peaked part of the detected beam profile has passed the collimators but on the other hand it is impossible for the broad part of the beam profile.

The measurement clearly shows that a beam halo could not pass the collimator. The section between the collimator and detector contains only drifts and solenoids and the beam is not strongly focused. A mechanism which could generate such a halo under such common conditions is not known. As a consequent this measurement is an evidence that the beam halo has to be an artifact and is probably caused by the detector system.

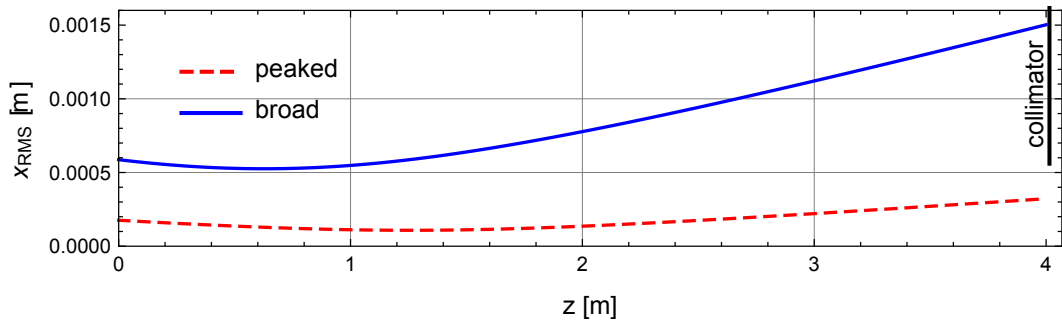


Figure 3.21: Backtracking of the peaked and broad Gaussian distribution from Sol67 to the collimator ($d = 1.1$ mm) at DDC2 using the fit results from Tab. 3.6. The black vertical line indicates the collimator position and its radius.

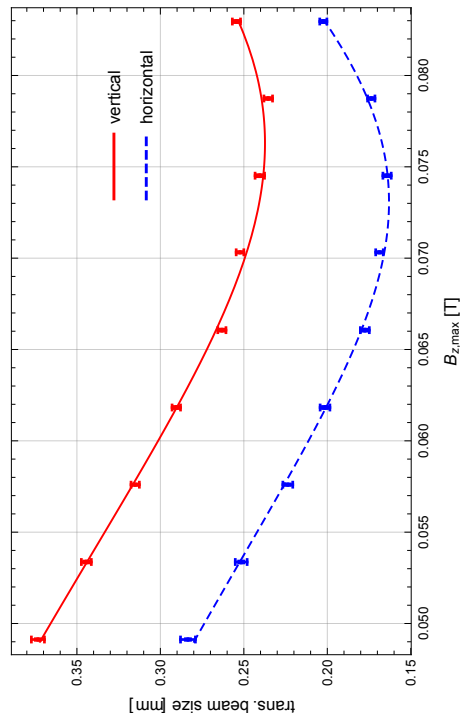
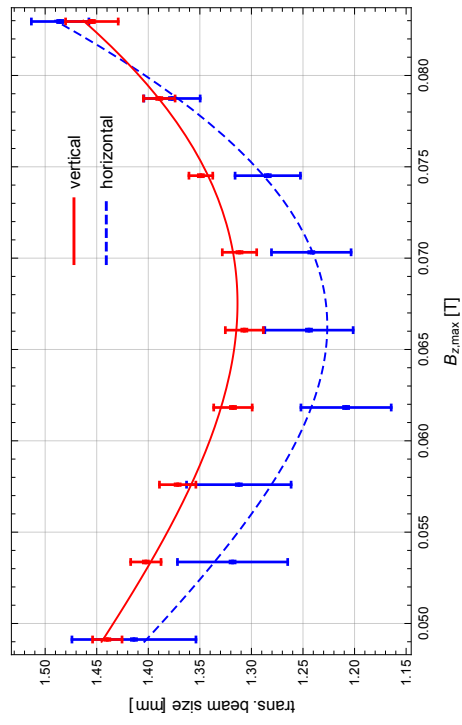


Figure 3.22: Beam size scan and fit of the peaked (left) and of the broad (right) Gaussian beam part.

Table 3.6: Emittance fit results of the peaked (upper) and the broad (lower) profile part.

Direction	$\epsilon_{n,rms}$ [π mm mrad]	$s_{0,rms}$ [mm]	$(s_{0,rms})'$ [μ rad]	χ_{red}^2
horizontal	0.054(6)	0.162(3)	71(3)	1
vertical	0.085(7)	0.176(4)	87(3)	1.8
horizontal	1.79(27)	0.72(6)	217(51)	0.3
vertical	1.56(13)	0.59(4)	187(26)	0.4

3.3.2 FOS investigations in the laboratory

To support the assumption that the detector system generates the broad halo measurements in the laboratory have been set up. An arrangement compatible to the original light optic has been used. A schematic layout is shown in Fig. 3.23. A β^- -source is placed on top of the FOS screen. Due to the β^- emission the FOS scintillates light in the visible range which is reflected by the mirror and focused by the lens to the EMCCD Andor camera. All crucial components of the detector system as the FOS and the Andor camera are included in this setup. It is of course unlikely that the light optics of the detector D1 generates the halo. The whole setup is housed in a black box to avoid any kind of stray light.

Weak β^- -source ^{137}Cs

The measurements were performed with the help of Dr. Delsim-Hashemi. Two different β^- -sources have been used. Firstly a comparably weak ^{137}Cs source (Tab. 3.7) with an activity of 200 kBq has been used. Due to the low activity a long exposure time of 30 min has been necessary. The lower left plot of Fig. 3.24 shows a taken image. The emitting area of the source was as large as the FOS area. Therefore a Plexiglas piece with a 5 mm slit has been placed between the source and the FOS to image a sharp edge. The halo should be visible at this edge. A simple approach has been chosen to describe a uniform distributed β^- -beam imaging a sharp edge (Fig. 3.24, upper). Theoretically the intensity profile should rise linearly (green curve). Due to scattering at the edge a smeared out profile is

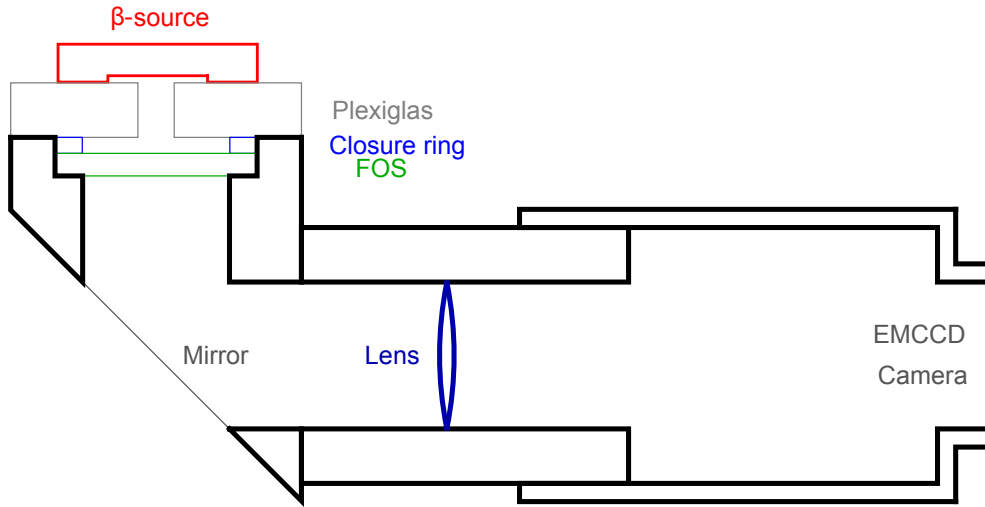


Figure 3.23: Experimental setup of the FOS measurement with a β^- -source.

expected which will be approximated by an *error-function*

$$I_{\beta}(z) = \frac{A}{2} \left(\text{Erf} \left(\frac{z - \mu}{\sigma} \right) + 1 \right), \quad (3.25)$$

where A is the amplitude, μ the position of the half-height of the error-function, σ is the width of the error-function. The maximal slope right at the half-height position and the slope m_r of the theoretical linear ramp are equal. With the slope m_r and the maximum intensity A the characteristic width rt (red,dotted) of the linear ramp is simply given as:

$$rt = \frac{A}{m_r}. \quad (3.26)$$

On the other hand rt is defined by the geometry of the setup, where w is the slit width, h height and d the distance from the Plexiglas bottom to the FOS:

$$rt = d \frac{w}{h}$$

which yields $rt = 1.47$ mm for $w = 5$ mm, $h = 7.5$ mm and $d = 2.2$ mm.

The edge profile (Fig. 3.24, lower left) has been integrated along x to apply a fit with the model introduced in Eq. 3.25. The result is shown in the lower right of

²D3 prepares and characterizes radioactive preparations.

Table 3.7: ^{137}Cs decay including all subsequent decays. Strongly unlike decay channels are ignored. Data received from DESY's radiation safety group D3².

^{137}Cs (200 kBq; 30.17 a)

Progeny	Species	Probability [%]	Max. E_{kin} [keV]	Avg. E_{kin} [keV]
$^{137\text{m}}\text{Ba}$	β^-	94.6	512	174
^{137}Ba	β^-	5.4	1176	416.3

$^{137\text{m}}\text{Ba}$ (200 kBq; 2.55 min)

Progeny	Species	Probability [%]	Max. E_{kin} [keV]	Avg. E_{kin} [keV]
^{137}Ba	γ	100	661.6	-

Fig. 3.24. Due to the weak signal the measured profile is a bit noisy but still the expected intensity trend is observable and the fitted curve matches pretty well. From the fitted amplitude A and width σ the characteristic width of the ramp yields $rt = 220(9)$ pixel. For the optical setup of this measurement a pixel calibration of $6.7 \mu\text{m}/\text{pixel}$ has been found. Hence, rt is $1.47(6)$ mm which coincide with the theoretical value.

Unfortunately, the halo is not visible. It should add a further component to the intensity profile which is not included in the introduced model and therefore should be visible as a deviation from the model in the measurement. A possible explanation for the absence of a halo in this measurement will be presented at the end of this section. But first a second measurement with a stronger and much more active β^- -source will be presented.

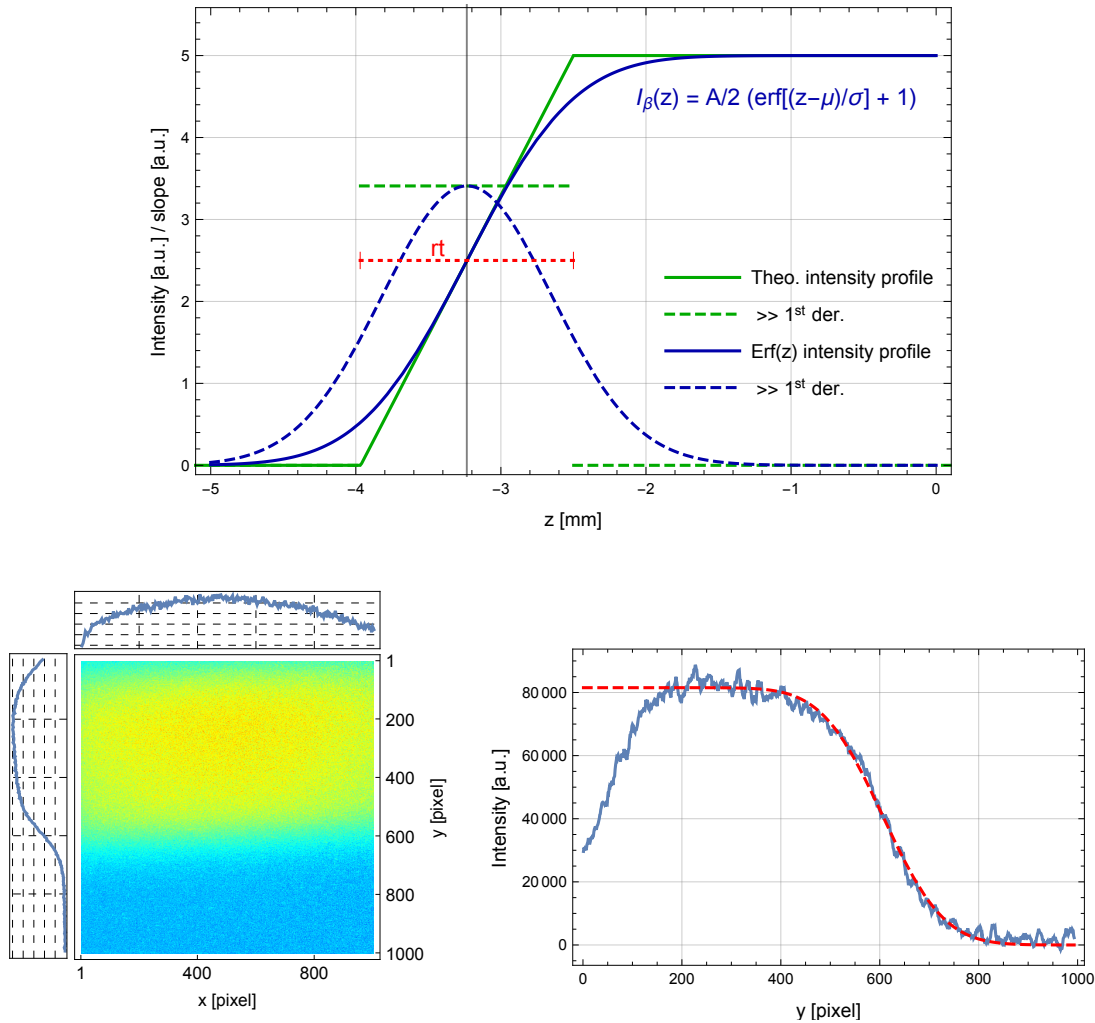


Figure 3.24: Upper: A theoretical profile of an imaged edge (solid green) and an approximation with an error-function (solid blue). In addition the derivatives of the solid lines are depicted (dashed lines). The vertical gray line marks the position of the half-height of the error-function/intensity profile and the maximal slope of the error-function. The red dashed line indicates the ramp's width rt . **Lower Row:** The left plot shows the 2D profile taken in the laboratory using the ^{137}Cs source. The right plot shows the integrated profile (solid blue) and a fit using the introduced model (dashed red). The intensity profile is obtained by averaging over 10 pixel columns of the left profile.

Strong β^- -source ^{90}Y

The second source, ^{90}Sr , decays into ^{90}Y which is the main β -source (Tab. 3.8). Compared to ^{137}Cs it was more active and has a higher max. kinetic energy. This is more comparable to REGAE conditions. Because the emitting area was small the Plexiglas edge imaging method was not necessary. A nice round spot could be imaged with the setup. An exposure time of only 30 s was sufficient.

The measured profile as well as its projections are shown in Fig. 3.25. The signal

Table 3.8: Characteristics of the β -decay of ^{90}Sr and ^{90}Y . Data received from DESY's radiation safety group D3.

^{90}Sr (2.34 MBq; 28.74 a)

Progeny	Species	Probability [%]	Max. E_{kin} [keV]	Avg. E_{kin} [keV]
^{90}Y	β^-	100	546	195.8

^{90}Y (2.34 MBq; 64.10 h)

Progeny	Species	Probability [%]	Max. E_{kin} [MeV]	Avg. E_{kin} [MeV]
^{90}Zr	β^-	99.99	2.28	0.9298

has long tails but it is really smooth - not comparable to the distinct halo of REGAE beam profiles (see Fig. 3.18). This smeared-out profile can be explained by the broad energy spectrum of the β^- -source. Low energy electrons are scattered more strongly inside the CsI scintillator which broadens the scintillation light profile as well. A more precise inspection of the measurements done with the β^- sources will be made in the next section by means of Monte Carlo simulations. At this point a clear statement about the halo could not be done.

3.3.3 EGS5 simulations

Despite the measurements done in a laboratory environment with a REGAE-like detector system including the same FOS and camera the source of the halo could not be clearly identified. Thus simulations have been performed to emphasize the assumption that the halo is an artifact of the detector system. The hypothesis is: electrons are scattered from the Fiber Optic Plate (FOP, Sec. 3.1.2) towards

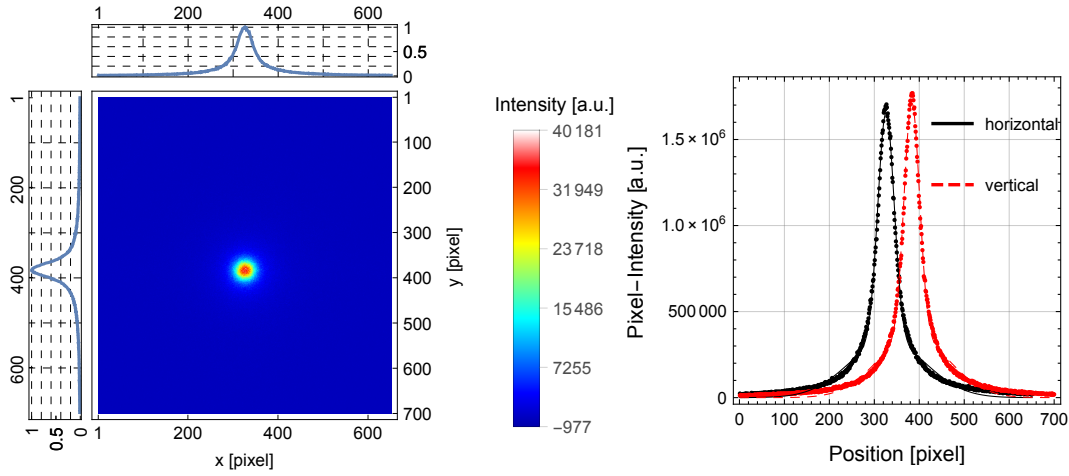


Figure 3.25: Left: Beam profile of a 30s exposed FOS to a ^{90}Y β^- -source.
Right: Horizontal and vertical beam projections (dots) fitted with a double Gaussian (solid/dashed lines).

the CsI scintillator and scintillate again. Due to the scattering inside the different layers of the FOS the electron distribution gets broader. The resulting scintillation signal overlays with the original signal of the electron beam and forms the characteristic double Gaussian transverse beam profile at REGAE. Consequently the broad part of the beam profile is an artifact and should not be taken into account for any kind of measurement and especially not for emittance measurements where the RMS beam size is essential.

For the simulations the Monte Carlo based program EGS5 [63] has been used. EGS (**E**lectron-**G**amma **S**hower) is a commonly used software package to simulate the coupled transport of charged particles as well as photons through any geometrical arrangement of various types of matter. It takes all kinds of interactions between particles (electrons, positrons, photons, etc.) and the chosen medium into account. For charged particles there are two kinds of interaction which matters: collisions or irradiation. Collisions can lead to excitation or ionization of an atom. Subsequently all generated secondary particles are tracked and interact with matter or particles again. Irradiation of an electron inside a medium due to the Coulomb field of the atoms will generate Bremsstrahlung. For the generated photons three interaction schemes are relevant depending on the photon energy: For high energy

photons the pair production is dominant and Compton scattering for mid-range photons (MeV range). The lower energy range is dominated by the photo effect. All particles are tracked until a termination criterion is reached. This could be a lower energy limit where the particle will probably be stuck inside the medium or when it leaves the medium. All details of the EGS code and how the various algorithms are working can be checked in the manual [63] and won't be explained in detail in the course of this thesis.

The geometry of the FOS has been realized as a layer of CsI and glass. The exact

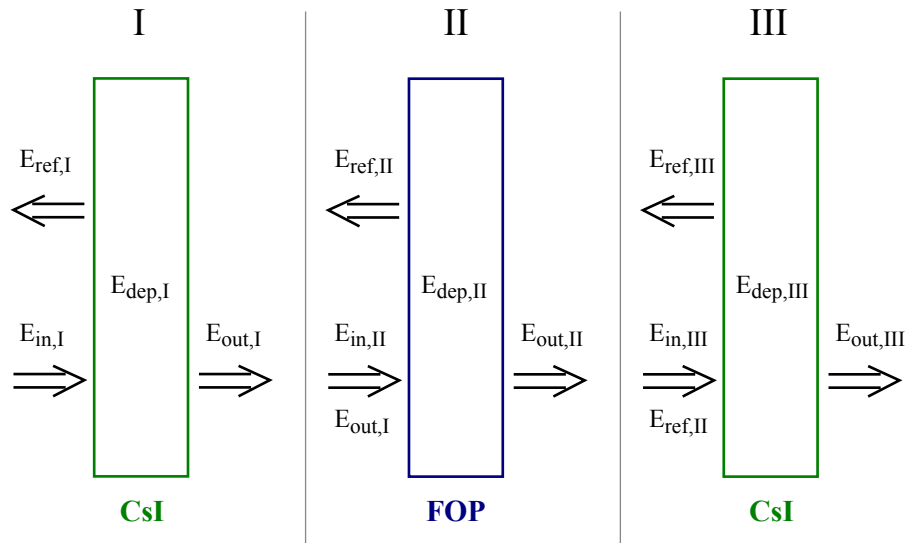


Figure 3.26: Schematic of energy transfer and deposition for an EGS simulated FOS screen. The scattering process at the different layers is divided in three segments (I-III).

composition of the FOP has been assumed to be a layer of flint glass. Flint glass has a density of $\rho_{fg} = 3.88 \text{ g cm}^{-3}$. The density of the FOP has been approximated to be $\sim 4.5 \text{ g cm}^{-3}$ in Sec. 3.1.2. Even if the density is underrated the principle mechanism can be shown. Therefore the comparability of the FOP with flint glass is good enough. The FOP does not scintillate itself and mainly the back scattering of electrons is of interest.

For each layer a full evaluation of the incoming, deposited, reflected and outgoing energy has been done. The complete scattering process inside the FOS can be separated into three segments:

- I. Incoming electrons from source are hitting the CsI layer.

II. Transmitted electrons from CsI layer are hitting the FOP.

III. Reflected electrons from the FOP are hitting the CsI layer again.

The energy transmission, deposition and the different segments of the simulation are illustrated in Fig. 3.26. The simulation of each layer has been combined to form a full simulation of the FOS. This simulation routine has been performed for two different electron sources: The ^{90}Y β^- source from the laboratory setup and a REGAE-like electron beam which has a comparably high (~ 2.5 MeV) and almost mono-energetic energy - the energy spread has been neglected for the EGS5 simulations.

The simulation of all segments has started with a point-like electron distribution because of simplicity. A beam profile can be integrated by convolving the resulting profile with an arbitrary initial profile. But this can be done in a post-processing step and can be used to illustrate the similarity between measured and EGS simulated beam profiles. The second aim of this section is to get an adequate impression of the deposited energy inside the CsI layer of the FOS which is proportional to the scintillation light emission. Hence, the ratio of the halo intensity and the peaked beam intensity of the measured beam profiles should be comparable to the simulated electron energy deposition inside the scintillator layer of the incoming electrons and the back scattered from the FOP.

Because the energy loss inside the CsI layer depends on the incident energy E_{in} it is useful to determine the relative energy loss at a $150\ \mu\text{m}$ thick CsI crystal like it is integrated in the FOS of the REGAE detector system D1. The relative energy loss as well as the empirical stopping power of CsI from Sec. 3.1.3 are compared in Fig. 3.27. The stopping power has been used to estimate the absolute light yield of the FOS scintillator. It should coincide to the energy absorption obtained from an EGS simulation. For comparison the stopping power (Eq. 3.1) needs to be divided by the incident energy E_{in} to yield the relative energy absorption p_{e^-} :

$$p_{e^-} = \frac{E_{e^-} - (E_{\text{kin,in}})}{E_{\text{kin,in}}} = \frac{P(E_{\text{kin,in}}) \rho_{\text{CsI}} d_{\text{CsI}}}{E_{\text{kin,in}}}. \quad (3.27)$$

For incident energies above 1.5 MeV the two curves coincide pretty well but for lower energies the different assumptions of the models are visible. The model of the stopping power does not take secondary particles and their interactions into account. Furthermore for low energies Eq. 3.27 has to diverge because the theoretical energy deposit along the full depth d_{CsI} is calculated but low energy

electrons will be stopped before reaching the full depth and of course only deposit their total kinetic energy. Considering this the EGS5 simulation and the empirical model agree for a certain energy range and deviate especially for low energies.

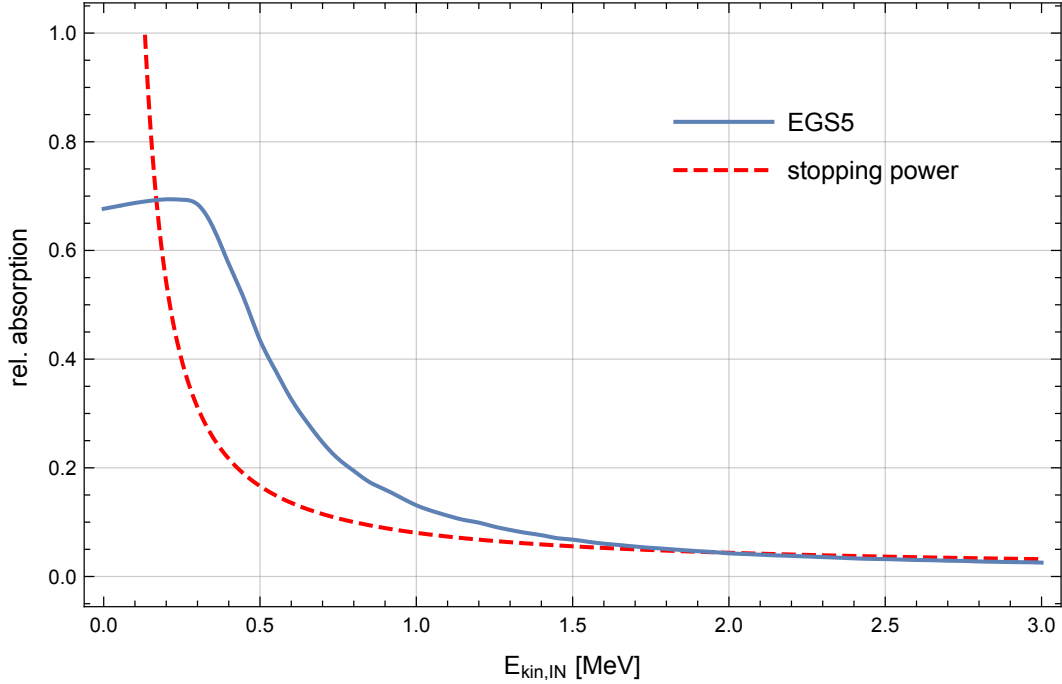


Figure 3.27: Relative energy absorption of CsI ($d = 150 \mu\text{m}$) as function of the incident energy E_{kin} . Simulated with EGS5 and calculated with the stopping power $P(E_{\text{kin}})$ (Eq. 3.1).

^{90}Y β^- -source

The main difference between a REGAE-like electron beam and the β^- source used in the laboratory is the energy width of the beta source. In order to reproduce the measured results of the laboratory setup the EGS5 simulations have to be extended by the β^- emission spectrum of ^{90}Y . The spectrum can mathematically described by *Fermi's golden rule* [64] which leads to an expression of the energy spectrum $N(T)$:

$$N(T) = C_L(T) F(Z, T) p E (Q - T)^2, \quad (3.28)$$

where T is the kinetic energy, C_L is a shape function which indicates the forbiddenness of a decay - it is constant for allowed decays. $F(Z, T)$ is Fermi's Function with Z as the final-state nucleus charge. E is the total energy and p the momentum, both obviously depending on T . Q is a characteristic constant of each decay. In case of a β^- -decay it is the maximum β^- or neutrino energy, respectively. Based on the *mass-energy equivalence* Q can be easily calculated as

$$Q = (m_{ini} - m_{fin}) c^2,$$

with the initial and final mass of the radionuclide.

Fermi's Function $F(Z, T)$ takes the Coulomb attraction/repulsion between the nucleus and the emitted β^- into account. It is defined as

$$F(Z, T) = \frac{2(1+S)}{\Gamma(1+2S)^2} (2p\varrho)^{2S-2} e^{\pi\eta} |\Gamma(S+i\eta)|^2 \quad (3.29)$$

and contains again the β^- -momentum p which can be substituted by the total energy $E = T + m_e c^2$:

$$p = \sqrt{(E/c)^2 - (m_e c)^2}.$$

Γ in Eq. 3.29 is the mathematical *Gamma function*. The remaining expressions are defined as follows:

$$\begin{aligned} S &= \sqrt{1 - \alpha^2 Z^2}, \\ \eta &= \frac{\alpha Z E}{p c}, \\ \varrho &= \frac{r_N}{\hbar}, \end{aligned}$$

where α is the *fine-structure constant*. The nucleus radius r_N can be easily approximated with

$$r_N = r_0 A^{1/3},$$

where A is the atomic mass number. r_0 is not a real constant, but it varies slightly for the specific nucleus. The average error of an arbitrary nucleus is below 20% which is sufficient for the purpose of this simulations. All relevant constants are given in Tab. 3.9. The β^- -spectrum $N(T)$ (Eq. 3.28) of ^{90}Y is plotted as a *probability density function* (PDF) in Fig. 3.28.

Table 3.9: Constants required for Fermi's golden rule of ^{90}Y β -decay.

Q [MeV]	2.2801
C_L	0.4881
A	90
r_0 [m]	1.25×10^{-15}
α	7.297×10^{-3}

To realize the β^- -spectrum of ^{90}Y in an EGS simulation a uniform energy spectrum has been simulated by repeating the same simulation for the whole range of energy which can be delivered by a ^{90}Y β^- -source. By mapping the energy spectrum on the simulation results the energy deposition has been corrected. This method can be used for each layer of the FOS - just the energy spectrum of the incident electron distribution needs to be adapted. Fig. 3.28 and Fig. 3.29 show the development of the energy spectrum passing the different layers of the FOS. The main difference between the original energy spectrum of ^{90}Y and the spectrum after passing the first layer (CsI) is the energy loss at lower energies. The overall shape is still similar to the original shape. In strong contrast is the energy spectrum of the back scattered electrons. It is shifted to low energies which will deposit a huge amount of their energies during the second passing of the CsI layer. The final energy deposition in the CsI layer has been calculated from the back scattered electron spectrum and the energy absorption curve of CsI (Fig. 3.27). Tab. 3.10 summarize the energy transmission and deposition in all three segments of the simulation. Due to the simplified calculation method of segment III, only the deposit energy $E_{dep,III}$ is available.

Because the deposit energy inside the CsI layer of the FOS is proportional to the scintillated light intensity, the relative energy deposition of the incident electron beam ($E_{dep,I}$) and the back scattered electrons from the FOP towards the CsI ($E_{dep,bs}$) is proportional to the intensity ratio of the beam signal and the halo detected by the camera. Using the terminology of Fig. 3.26 this energy ratio can be defined as:

$$\frac{E_{dep,bs}}{E_{dep,I}} = \frac{E_{out,I} \cdot E_{ref,II} \cdot E_{dep,III}}{E_{dep,I}}. \quad (3.30)$$

For the ^{90}Y simulations this ratio is **0.153**. The amount of deposited energy from

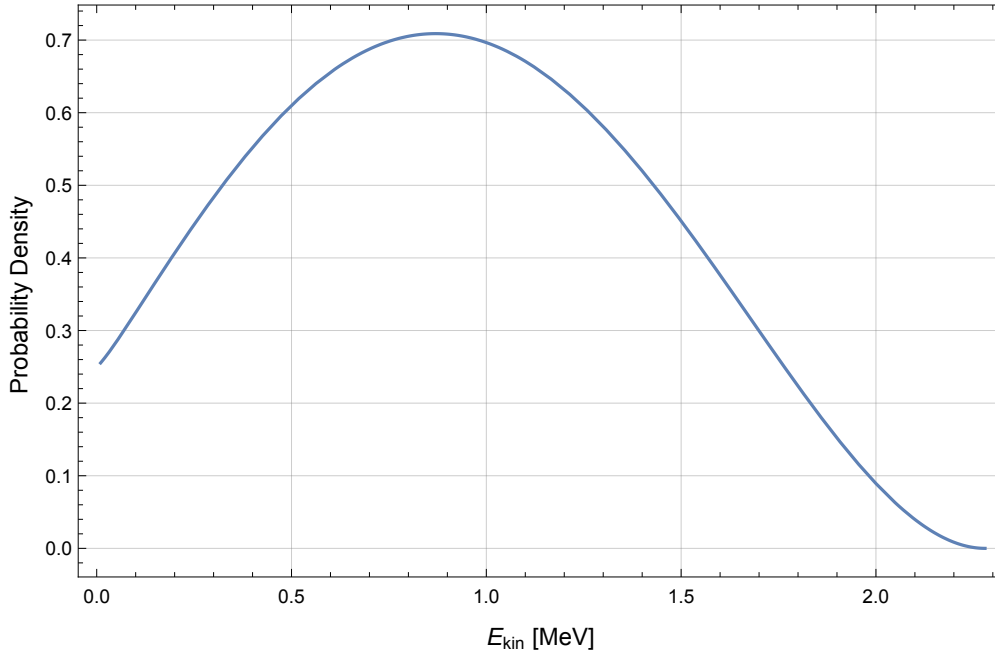


Figure 3.28: Energy spectrum of β^- -emitter ^{90}Y . E_{kin} is equivalent to T in Eq. 3.28.

back scattered electrons is compared to the directly deposited energy low. The reason is the broad energy spectrum of the source. Fig. 3.30 illustrates the amount of in forward direction transmitted energy through the CsI from a ^{90}Y source. The difference between the red dashed and blue solid line is approximately the deposited energy - neglecting the reflected fraction. The relative energy absorption of CsI is of course much higher for lower electron energies. hence, the deposited energy of the electrons inside the CsI in the first place is already high and consequently the back scattering effect is comparably low.

Table 3.10: Energy transmission and deposition of a ^{90}Y β^- -spectrum passing a FOS screen.

Segment	\mathbf{E}_{in}	\mathbf{E}_{out}	\mathbf{E}_{ref}	\mathbf{E}_{dep}
I	1	0.723	0.116	0.153
II	$\mathbf{E}_{out,I}$	~ 0.0	0.091	0.893
III	$\mathbf{E}_{ref,II}$	-	-	0.352

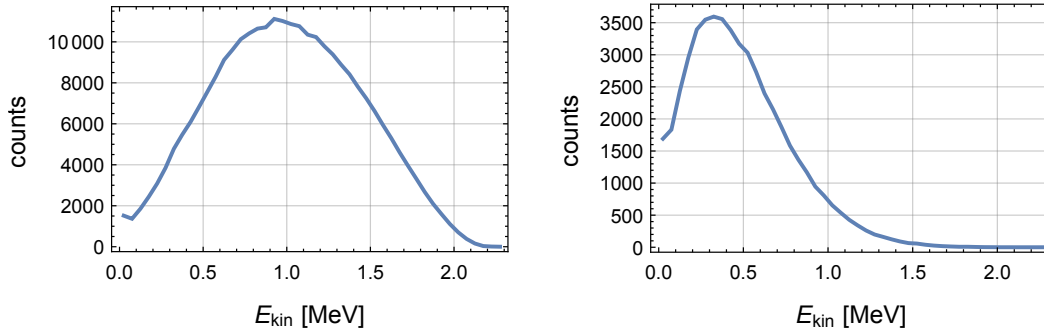


Figure 3.29: Left: Energy spectrum of electrons leaving the CsI layer. Pertaining to Fig. 3.26 the integral of this spectrum is equivalent to $E_{out,I}$. **Right:** Energy spectrum of back scattered electrons from FOP. The integral of this spectrum is equivalent to $E_{ref,II}$. **Both:** 'Counts' is an arbitrary relative unit and has only a qualitative character for each plot.

Another consequence of the broad energy spectrum of ^{90}Y is the broadening of the beam profile. Depending of the energy the electron scattering inside the CsI layer is quite different. Fig. 3.31 shows the accumulated transverse profile broadening for the EGS simulation of segment I. Qualitatively it is already similar to the measured profile of Fig. 3.25. Because Fig. 3.31 shows only the broadened profile of a point-like source it has to be convolved with the incident transverse profile of the ^{90}Y source and subsequently with the profile of the back scattered electrons from the FOP. Due to the comparably low contribution of the back scattered electrons to the total deposited energy in the CsI layer they just contribute as a broad underground to the final beam profile. Because it is difficult to estimate the incidental beam profile and because Fig. 3.31 already shows a good agreement with the measured profile, a detailed analysis of the profiles has not been done. Summarizing, it is not possible to distinguish between the real signal and the artifact caused by the FOS with the laboratory setup.

In a final step a REGAE-like case will be simulated and analyzed in the next subsection. The higher kinetic energy and almost mono-energetic spectrum of the electrons will make it easier to distinguish between the real signal and the artifact.

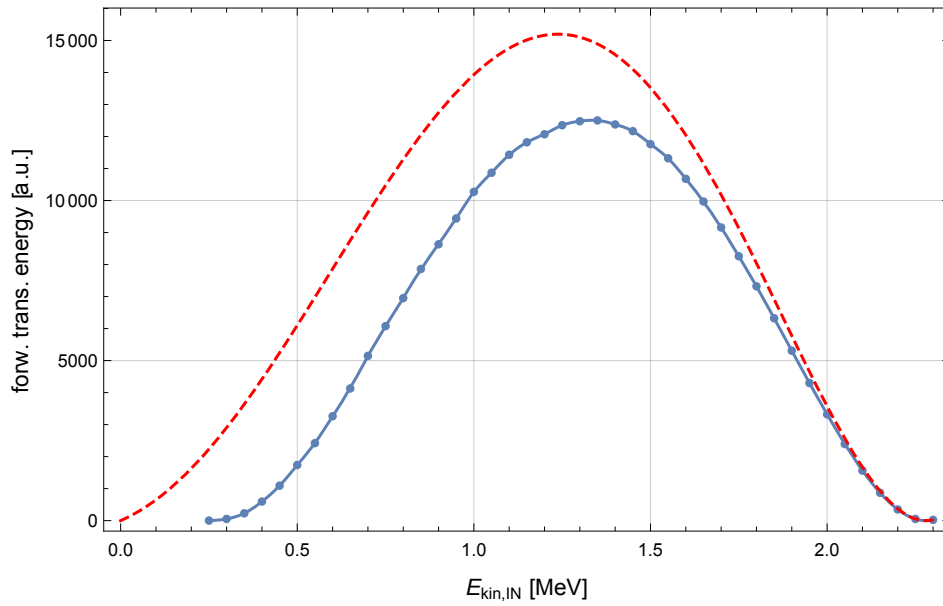


Figure 3.30: Total transmitted electron energy in forward direction (solid, blue) depending on incident electron energy $E_{\text{kin,in}}$ for a $150\ \mu\text{m}$ thick CsI scintillator. As well the original total energy distribution of ^{90}Y (red, dashed) is shown.

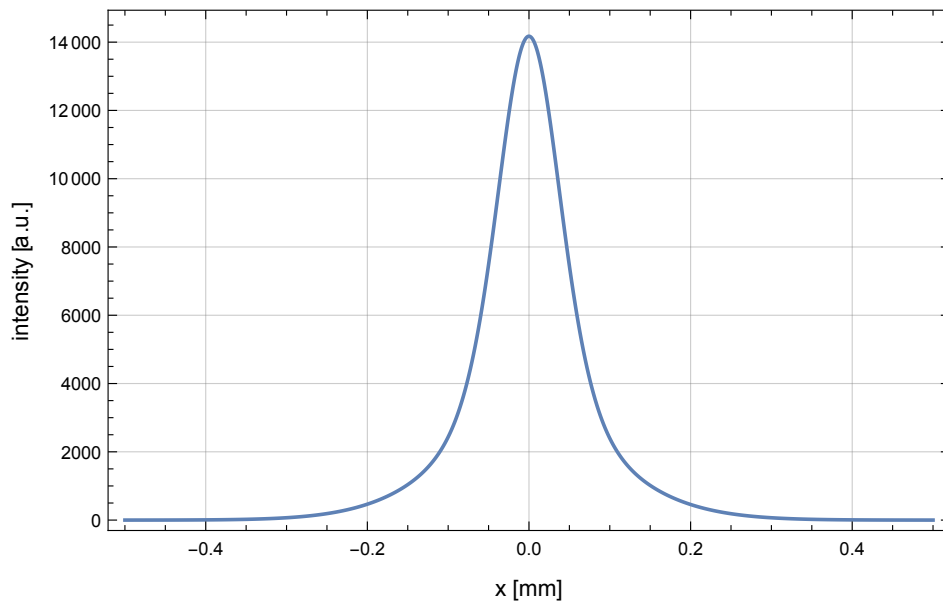


Figure 3.31: Accumulated transverse profile of $^{90}\text{Y}\ \beta^-$ -source after passing the CsI layer ($d = 150\ \mu\text{m}$).

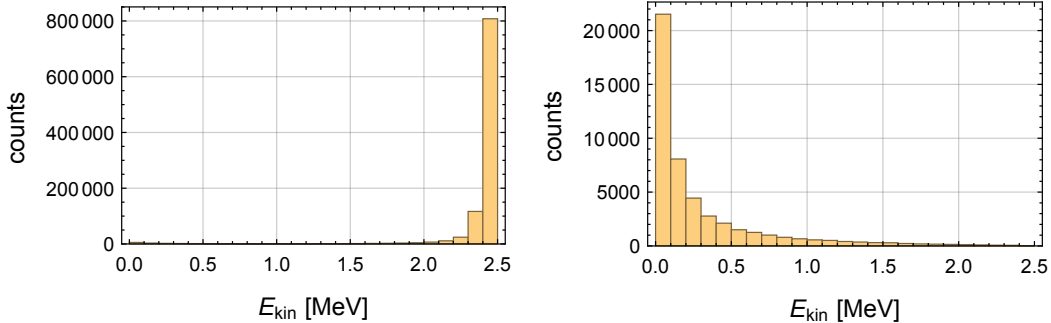
REGAE case


Figure 3.32: Energy spectrum of the forward moving electrons (left) as well as photons (right). $E_{\text{kin,in}} = 2.5$ MeV.

For the REGAE-like simulation 2.5 MeV electrons have been simulated. The simulation routine is the same as for the ^{90}Y case. Each layer of the FOS will be simulated and analyzed separately. An additional assumption is a negligible energy spread. Again, a point-like electron source has been used so that subsequently a transverse profile has to be convolved to obtain a final transverse profile. Starting with the first segment of the FOS simulations: the high energy electrons are only slightly scattered at the CsI layer and the average energy in forward direction is approximately still 2.5 MeV (Fig. 3.32, left). Therefore segment II starts with the same energy of 2.5 MeV. Another assumption which has been made already for the ^{90}Y β^- -source can be shown exemplarily for the REGAE-like case as well. Besides electrons Bremsstrahlung is generated. The energy spectrum of the forward directed Bremsstrahlung is shown in the right plot of Fig. 3.32. The counts of both histograms in Fig. 3.32 are proportional. The fraction of forward moving gammas to electrons and potential back scattered gammas is so low that they can be neglected.

Again, an evaluation of each segment of the simulation routine is possible and yields a quite different picture of the energy deposition of incident and back scattered electrons. On the one hand the energy deposition of the main beam is comparably low but the fraction of the back scattered electrons from the FOP is low as well. The detailed results are listed in Tab. 3.11. The ratio, introduced in Eq. 3.30, of deposited energy of the back scattered electrons from the FOP and the originally incident electrons is equal to $0.011/0.032 \simeq 1/3$ in case of almost

Table 3.11: Energy balance of a REGAE-like electron beam of 2.5 MeV hitting the FOS scintillation screen. Chronological relative energy loss/transmission of the two layers CsI and FOP. Photon production and energy deposition is neglected.

Segment	E_{in}	E_{out}	E_{ref}	E_{dep}
I	1	0.950	0.012	0.032
II	$E_{\text{out,I}}$	0.024	0.051	0.886
III	$E_{\text{ref,II}}$	-	-	0.228

mono-energetic electrons. Compared to the case of the ^{90}Y β^- -source the ratio is higher.

To demonstrate the quite good coincidence between the simulations and measurements at REGAE it is worth to take a closer look at the transverse beam profiles. The main electron beam is just slightly broaden after the first layer of CsI. More interesting is the profile of the back scattered electrons from the FOP. It is shown in Fig. 3.33. The upper row shows the profile and the lower plot the energy spectrum. Beside the peaked center, which in worst case just slightly broaden the signal and in the best case amplify the main signal, the broad part of the profile is of interest. It is generated by a point-like 2.5 MeV source and has a standard deviation of 1.2 mm. It contains a large fraction of the total back scattered energy. Due to the broad energy spectrum a huge amount of the energy will be deposited in the CsI layer. To get an impression of the total transverse profile of a normal distributed electron beam passing the FOS and all subsequent scattering at the different layers it is necessary to convolve the incident electron beam profile with the outgoing profile of the CsI layer and the back scattered profile from the FOP. The result is plotted as solid blue profiles in Fig. 3.34. The three plots compare the simulated EGS profile of an electron beam scattered forth and back inside the FOS with the original unscattered profile (upper, left) and a measured beam profile at REGAE (lower). For the incident electron distribution of the simulation a profile similar to the measured has been used. It has the same standard deviation and amplitude like the peaked part of the measured profile. The upper right plot of Fig. 3.34 shows the almost perfect agreement of the scattered electron beam profile with a double Gaussian function (Eq. 3.24). The ratio of the integrated intensities of the broad part and the peaked should be equal to the energy ratio of

the deposit energies of forward and back scattered electrons inside the CsI layer. And indeed it is, the ratio of the intensities is 0.347 compared to 0.344 from the deposit energies. This just proves the consistency of the simulations.

The simulated and measured profile have a similar shape and both show a distinct halo. Only the intensity ratio of the both components do not agree. The halo of the measured profile contains a larger portion of the total intensity. But still, the tendency of the simulation shows a quite good agreement between the assumption about the origin of the beam halo at the REGAE detector and the real measurements. The discrepancies between the measurement and the simulation are probably due to the simplifications and assumptions of the FOS and electron beam. There is another quite important result from the simulation which should be mentioned: The simulated beam profile has been formed by the simulation results on the one side and the peaked part of a measured double Gaussian beam profile on the other side. The pure Gaussian distributed profile at the beginning is almost unchanged in the final beam profile. Even if the FOS produces an artifact the original beam profile is easily accessible as long as the halo is treated correctly. Therefore the described method to handle the beam halo, introduced in Sec.3.2.3, is valid and can be used for further beam diagnostic applications.

Table 3.12: Comparison of the simulated transverse profile with EGS and a measured beam profile at REGAE. The profiles are shown in Fig. 3.34. Listed are results from a fit of the profiles. The double Gaussian function of Eq. 3.24 has been used. Besides the amplitudes a_1 , a_2 and the standard deviations σ_1 , σ_2 the integrated intensities I_1 , I_2 and their ratio I_2/I_1 are listed.

Fit	EGS	Measurement
a_1 [a.u.]	6.68×10^6	6.43×10^6
σ_1 [mm]	0.0720	0.0719
I_1	1.21×10^6	1.16×10^6
a_2 [a.u.]	1.40×10^5	2.82×10^5
σ_2 [mm]	1.20	0.97
I_2	4.20×10^5	6.86×10^5
I_2/I_1	0.347	0.591

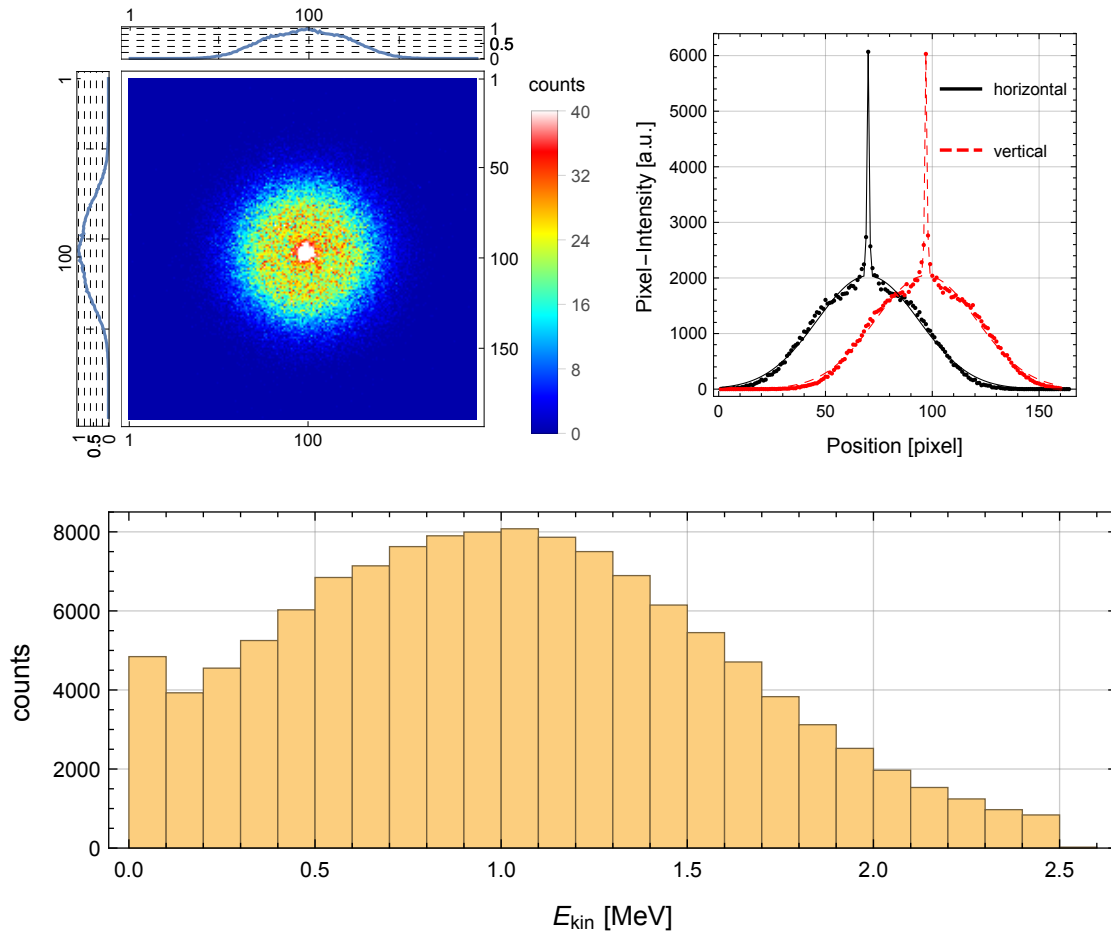


Figure 3.33: Upper, left: Beam profile of back scattered electrons from FOP.

Upper, right: Beam projections horizontal and vertical are shown and had been fitted with a double Gaussian function. The pixel size is $50\ \mu\text{m}$ and the fitted standard deviations of the profiles are equal in both directions. $\sigma_{x,1} = 0.03\ \text{mm}$ and $\sigma_{x,2} = 1.2\ \text{mm}$.

Lower: Energy spectrum of back scattered electrons from FOP.

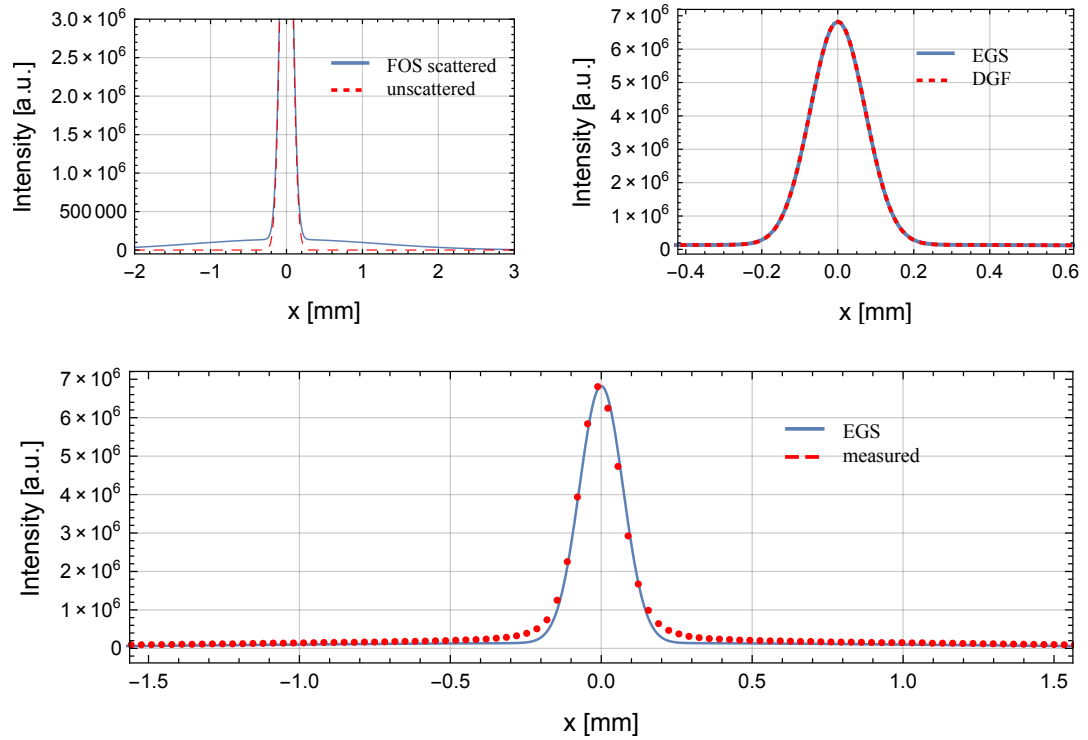


Figure 3.34: Upper Row: On the left hand side the comparison of a scattered (at all layers of the FOS) and unscattered (or incident) Gaussian REGAE beam profile. The original beam size (unscattered beam) is $\sigma = 71.9 \mu\text{m}$. Due to the scattering the distinct halo is visible. On the right hand side a fit with a double Gaussian function of the same scattered beam profile is shown. **Lower:** Scattered beam profile from EGS simulation compared with a measured profile at REGAE.

3.3.4 Conclusion

The investigations of the beam halo detected at REGAE's detector system D1 show clearly that the halo is an artifact of the FOS. The beam based measurement proves that the halo could not be real. Another suspicious fact is the observation of the halo on hundreds of images taken over almost four years. It seems unlikely that for a huge variety of machine and laser settings this halo is beam dynamically explainable. To verify the origin of the halo tests in the laboratory with the REGAE detector system D1 have been done. These measurements have not yielded clear results to undoubtedly judge about the origins of the halo. The first used β^- -emitter was too weak even if the measurement and the evaluation method worked quite well. The second emitter was much stronger but the distinct halo, which is always observable at REGAE's detector system, was missing. To explain the measurements of the laboratory setup and REGAE, simulations with EGS have been performed with a great success. But it should be mentioned that former simulations [65] using GEANT4 [66, 67] to study the interaction of electrons with a FOS have not revealed the distinct beam halo. A reason could be the different purposes of the studies. It is not clear whether back scattering and multi-scintillation has been considered for these studies.

Nevertheless the presented simulations matches the observations at the machine and the laboratory. Hence, the measured profile from the ^{90}Y β^- -emitter as well as the REGAE halo could be explained. What leads the conclusion that multi-scattering at different layers of the FOS generates the halo. Back scattered electrons from the thick and dense FOP scintillate in the CsI layer again but due to scattering inside the different materials the additional and unwanted scintillation signal is much broader than the original signal. The overlap of both forms the characteristic double Gaussian profile at REGAE. Even the measured profile from the ^{90}Y β^- -emitter can be explained by this mechanism. The scattering of electrons depends on their energy. The broad energy spectrum of a β^- -emitter yields an overlap of all the different energies. Therefore the distinct halo, known from REGAE, can not be observed. The signal of the incident electrons and the halo of the back scattered electrons add up to a smoothly shaped profile like it has been measured with the laboratory setup. The maybe most important realizing is that the incident beam profile seems to be preserved for the REGAE case of almost mono-energetic electron bunches. The halo appears just as an additional component which can be easily identified and treated. Hence, the introduced intensity

cut to eliminate the contribution of the halo to the RMS calculation is qualified and will be the fundament of the RMS determination for all data taken with the REGAE D1 detector system. Especially, it is of great importance for the emittance measurements of Chap. 5.

Development of an electron beam optics for the external injection experiment at REGAE

This chapter is dedicated to the upcoming beam optical challenges of the future laser plasma acceleration (LPA) experiments. A small transverse beam size down to a few μm at position of the plasma target inside the target chamber is required. Even with an excellent electron beam quality as it can be achieved at REGAE it is challenging to generate such small transverse beam sizes. A strong focusing is needed and it has to be located close to the target position. Due to geometrical limitations an in-vacuum solution has been preferred and in course of his master thesis T. Gehrke¹ [28] has developed a design for permanent magnetic solenoids (PMS). This chapter treats all steps which have followed the work of T. Gehrke concerning the assembling and characterization of the PMS. Especially for the assembling some specialized developments have been required to find the best solution. The second section of this chapter presents simulations to illustrate the feasibility of injecting the REGAE electron beam into a laser plasma wakefield using the PMS.

¹t.gehrke@dkfz.de

4.1 Permanent Magnetic Solenoids

In this section the permanent magnetic solenoids (PMS) is introduced. Besides a short overview of the design the assembling and magnetic field measurements of the PMS are of particular interest. Because the PMS is compounded from wedges a sorting algorithm has been developed to optimize the magnetic field quality. The algorithm is geared to the well known idea of sorting magnets for the assembling of undulators [68, 69]. The routine is described and results presented. It is based on a universal field quality criterion, which cannot only be applied to solenoids but to every type of magnet, and a simple analytical field model. Both have been checked with ASTRA simulations and the field quality criterion shows a great correlation with the beam quality of a tracked particle beam. Most results has been already presented in [70, 71]. Some aspects of this topic are examined in greater detail. Furthermore the magnetic field measurements will be presented - the measuring routine as well as the post-processing of the measured field which is necessary to compare it with the simulated field. For the measurement a highly precise 3D Hall probe has been used. Nevertheless it will be shown that the field imperfections of the assembled PMS are below the resolution limit of this probe. What consequently proves the quality of the sorting algorithm as well as of the developed field model.

4.1.1 Design

At this point a short recap of the developed design [28] is presented. Besides the strong focusing two more demands are desired: the emittance growth induced by the PMS should be as small as possible and the weight of the PMS has to be limited to enable an in-vacuum alignment with piezoelectric movers. Investigations of different designs have shown that the induced emittance growth for two radially magnetized rings is considerably smaller than for an axially magnetized ring if a weight limitation has to be applied. In the particular case at REGAE a reduction of the emittance growth by 65% is feasible by mimicking the magnetic field of the single axially magnetized ring with two radially magnetized rings. Furthermore it allows a larger influence on the field shape since a third free parameter, the distance $d = 2l_1$ between both rings, is introduced. The PMS dimensions (in mm) depicted in Fig. 4.1 are as follows $R_o = 25.4$, $R_i = 17$, $l_1 = 7.8$ and $l_2 = 44.8$ while the weight is just 0.628 kg. The focal length f for a 5 MeV electron beam is ~ 0.2 m. A small drawback of using radially magnetized rings is the constructional

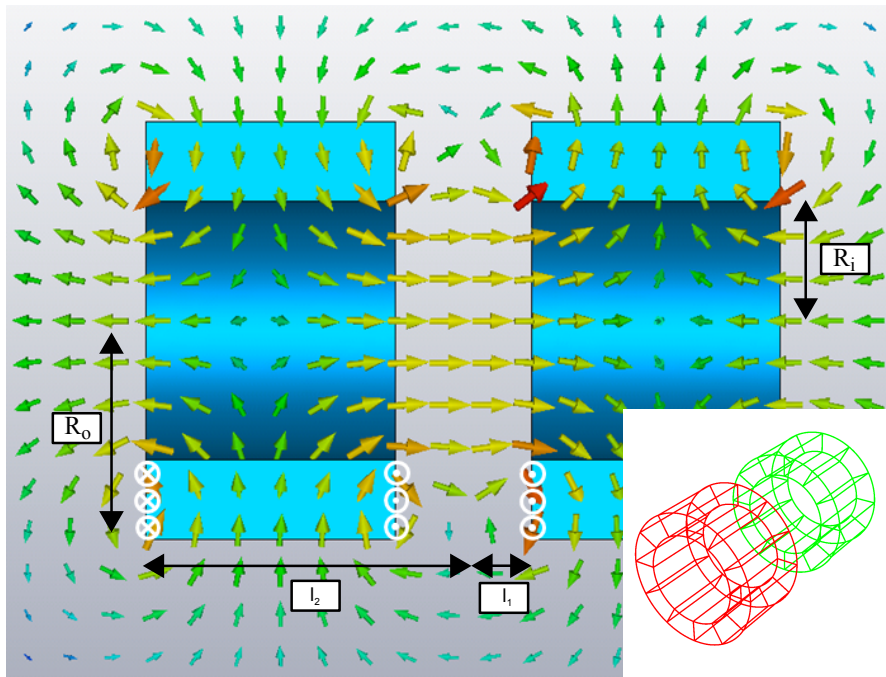


Figure 4.1: CST² simulation of two radially magnetized rings (blue) and the conceptual wedge-based design. The relevant dimensions of the PMS are illustrated.

realization. For technical reasons it was not possible to magnetize a single ring but instead each ring has to be assembled out of 12 individual wedges (schematic drawing Fig. 4.1). The used material for the wedges is a neodymium, iron and boron alloy (NdFeB) [72]. It provides high surface current densities to reach the required magnetic field strength. Due to technical reasons the amplitude as well as the magnetization direction of the wedges can vary too much to ignore it. This is a common issue and well known from other permanent magnetic structures assembled from pieces. Hence, it is necessary to optimize the assembling with a sorting algorithm to preserve the field quality.

²CST: Computer Simulation Technology [73]

4.1.2 Field description and sorting algorithm

Field model

Because the available codes (e.g. CST, using a Maxwell solver) to calculate the magnetic field of such an arrangement like the PMS had problems to resolve the magnetic field of wedges with small deviation from their magnetization and anyway a fast and accurate field description is preferred, a simple analytical field model has been developed. The approach of describing the magnetic field of 2×12 wedges bases on current loops covering the surface of each wedge (Fig. 4.2). Whereat each loop is described as four straight parts forming a quadrangle. Each straight part can be described by *Biot-Savart's law* with the result that the total magnetic field of a wedge $\mathbf{B}(\mathbf{r})$ follows as

$$\mathbf{B}(\mathbf{r}) = \sum_{i=1}^{N_L} \sum_{j=1}^4 \left(\frac{\mu_0}{4\pi} \int_{l_{ij}} I \frac{\mathbf{r} - \mathbf{r}'}{|\mathbf{r} - \mathbf{r}'|^3} \times d\mathbf{l} \right) \quad (4.1)$$

where \mathbf{r} denotes the position of the field and \mathbf{r}' the position of a wire element. I is the current and $d\mathbf{l}$ is the length of the differential element of the wire in the direction of the current. N_L is the number of current loops, i and j denote the specific current loop and a certain straight part, respectively.

The magnetization \mathbf{M} of a wedge is defined by the direction and its magnitude which were measured by the manufacturer and can be translated into a tilt of the current loops or a variation of the current I , respectively. These transformations have to be introduced to Eq. 4.1. The mean current over all wedges is chosen in a way that it reproduces the measured maximum longitudinal magnetic field. The manufacturing errors of the magnetization strength are added in proportion to this average current.

The model ignores inhomogeneous magnetization and the relative permeability ($\mu_r \leq 1.05$) of the wedges but is of course Maxwell conform. Because we are interested in the far field of each wedge this should be still a good approach.

Magnetic field quality of a Permanent Magnetic Solenoid

Since the total magnetic field of a two-ring setup is simply given as the superposition of the individual magnetic fields of flawed wedges, an optimal configuration of the 24 wedges can be found which preserve the transverse beam quality or only causes small deviations. Due to the absence of a common quantity which expresses

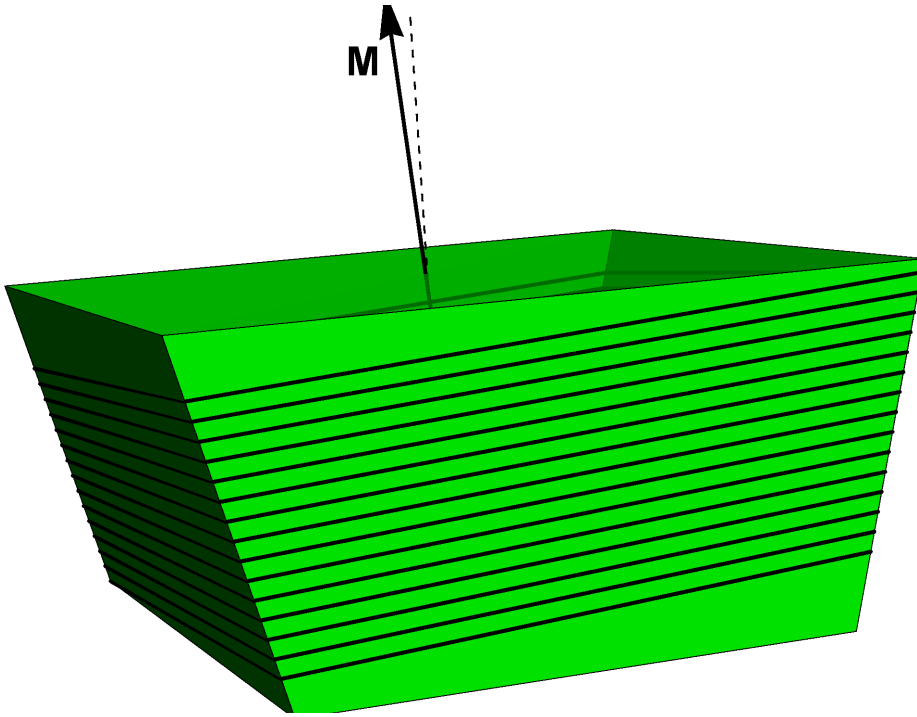


Figure 4.2: Current loops model of a flawed wedge with a tilted magnetization.

the field goodness of a solenoid a new one is introduced which is proportional to changes of the beam quality due to the magnetic field quality. It will be called χ and is motivated by the *normalized 4D-transverse emittance* (Eq. 2.1.1):

$$\chi \sim \epsilon_{4D}^2. \quad (4.2)$$

For an ideal PMS, meaning a PMS with 24 flawless wedges, the magnetic field is rotational symmetric along the longitudinal axis. For a PMS with flawed wedges this assumption no longer holds. Speaking in mathematical terms: the integral of the off-axis magnetic field along the longitudinal axis is no longer independent of the *azimuthal angle*. Therefore circular distributed line field integrals of the transverse field components (these could be described in *cylindrical* coordinates or *Cartesian* coordinates which are used in the following) which are zero only for an ideal solenoid field, are calculated. For a flawed solenoidal field the integrals are not zero anymore and as a consequence the transverse momentum of a charged particle passing the PMS is not independent of the azimuthal angle. For an ensemble of particles this leads to a decrease of the beam quality or in other words it leads to an emittance growth. To find a field quality criterion the asymmetry of the field

has to be expressed in a simple way. So that a simplified approach of a particle passing the PMS has been developed. A circular set of line field integrals around the symmetry axis will be calculated with the former mentioned field model. These field integrals are proportional to the final transverse momentum of imaginary particles traveling along these field lines.

$$p_x \sim - \int_a^b B_y(z) dz \quad \text{and} \quad p_y \sim \int_a^b B_x(z) dz$$

where the distance between a and b describes the integration length which should be long enough so that the magnetic field effectively drops to zero. The transverse position of the line field integrals is constant in longitudinal direction so that every line field integral represents one point in the 4D phase space (x, p_x, y, p_y) . The set of all points can be seen as a phase space distribution and the 4D-emittance-like quantity χ (Eq. 4.2) can be calculated. χ takes all kinds of correlations between the four transverse beam quantities $\{\langle x \rangle, \langle y \rangle, \langle p_x \rangle, \langle p_y \rangle\}$ into account.

Because the magnetic field of the PMS will be described numerically on a discrete grid and not analytically it is worth to think about the simulation parameters of the field model to calculate the field quality χ . There are three free parameters:

1. the number of current loops per wedge N_L - already mentioned above,
2. the number of magnetic field points along the magnetic field lines N_z ,
3. the number of magnetic field lines used to calculate the field quality N_{fl} .

The second parameter can be replaced by the step width between two magnetic field points δz . Reducing these numbers reduces the computation time to calculate χ . Therefore it has to be the aim to keep these numbers as small as possible without losing precision. Consequently it has to be checked how fast the field model converges. The focal length f of a solenoid can be chosen as a quantity to verify the field model quality in dependence of N_L . f has been already introduced in Eq. 2.30. Here, only the proportionality with the second field integral (compare Eq. 2.29) will be used:

$$\frac{1}{f} \sim F_2.$$

For the convergence test the numerical integral

$$\sum_{i=1}^{N_z} B_{z,0}(z_i)^2 \delta z \quad \text{with } N_z = 1001 \text{ and } \delta z = 0.4 \text{ mm,}$$

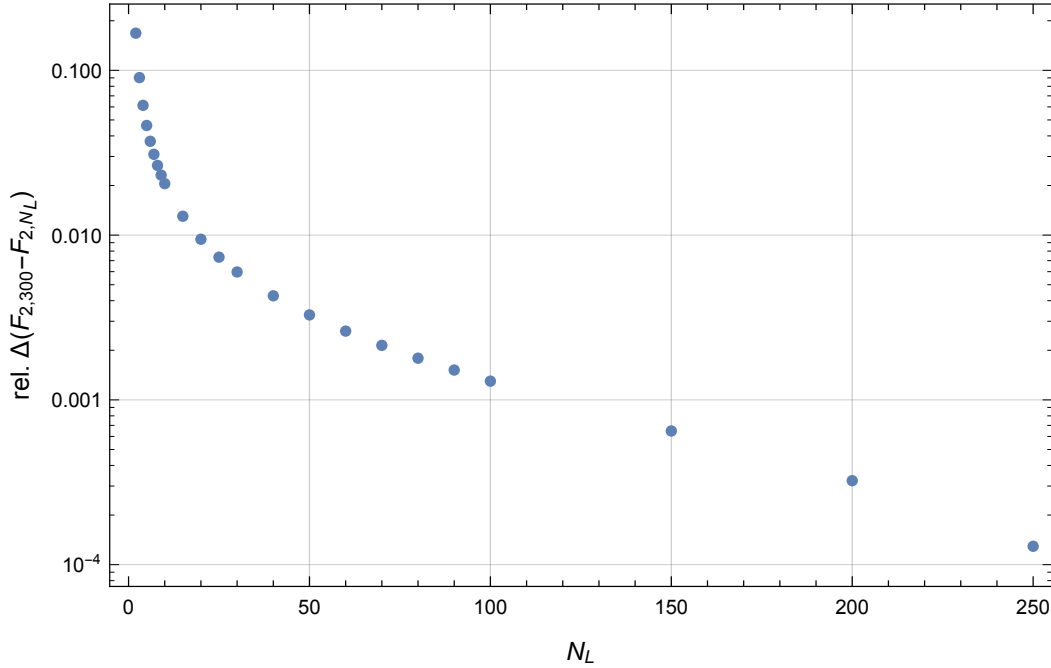


Figure 4.3: Deviation of the second field integral F_{2,N_L} from $F_{2,300}$ depending on the number of current loops N_L per wedge.

calculated with the field model, has been used. The relative deviation of F_{2,N_L} from $F_{2,300}$ is shown in Fig. 4.3. $F_{2,300}$ is assumed to be close to the maximal precision of this algorithm and has been taken as the reference. A deviation of $\sim 1\%$ seems to be acceptable which yields $\mathbf{N}_L = \mathbf{20}$.

In order to test the convergence of N_z or δz and N_{fl} the magnetic field quality factor χ (Eq. 4.2) can be used. As for N_L the line field integrals have to be numerically approximated to calculate χ :

$$\sum_{i=1}^{N_z} B_s(z_i)^2 \delta z,$$

where $s = x, y$. The total simulation range in z -direction was $z = [-0.5, 0.5]$ m. For the δz test $N_{\text{fl}} = 24$. On the other hand $\delta z = 1$ mm for the N_{fl} test. The results are shown in Fig. 4.4 and Fig. 4.5, respectively. To verify the convergence of different PMS assemblies it is helpful to normalize χ , called $\hat{\chi}$. It is always normalized to the most accurate χ provided by the particular series of tests.

For each PMS assembly $\hat{\chi}$ converges comparably slow for varying δz (Fig. 4.4, up-

per). It is interesting to note that the difference between the assemblies converges much faster. The absolute $\hat{\chi}$ is still increasing for smaller δz but it is almost independent on the assembly, shown in the lower part of Fig. 4.4. Therefore $\delta z \leq 2$ mm has been chosen for any further simulations.

For the convergence of χ depending on the number of magnetic field lines the result is pretty straight forward. Above $N_{\text{fl}} = 20$ the relative deviation from the maximum precision of χ is clearly below the per mil level as illustrated in Fig. 4.5.

Assembling of a Permanent Magnetic Solenoid

Using the computationally simple field description (Eq. 4.1) and the 4D-emittance-like quantity (Eq. 4.2) an evolutionary algorithm has been developed with the goal to find the optimal permutation for each ring with the given magnetization data provided by the manufacturer. A direct calculation of all permutations (1 PMS $\rightarrow 12! \times 12! \approx 2 \times 10^{17}$; excl. spare wedges and flipping) is not feasible. The algorithm is a two-step process. The first step consists of a numerical least-square algorithm [41] to determine a rough starting point for the second part. In the first part all available wedges - including spare wedges (pool) - are taken into account. In each iteration three actions can be performed:

1. swap with pool,
2. swap inside the rings,
3. flip around radial axis.

The second step is based on the concept of *simulated annealing* [74]. It is a common method for the assembling of magnetic structures like undulators [75] and can be adapted to this problem. A simulated annealing routine tries to find the global minimum of a fitness quantity $Q(x)$ like Eq. 4.2 by treating the system as a thermodynamical system with a falling temperature T . For each iteration $Q(x)$ is determined. Also T is lowered according to a predefined sequence. In our case each iteration consists of swapping wedges inside the rings or flipping them. x corresponds to a certain permutation of both rings whereas x_{opt} is the current best solution. If $Q(x) \leq Q(x_{\text{opt}})$, $x_{\text{opt}} = x$. If $Q(x) > Q(x_{\text{opt}})$, $x_{\text{opt}} = x$ with a

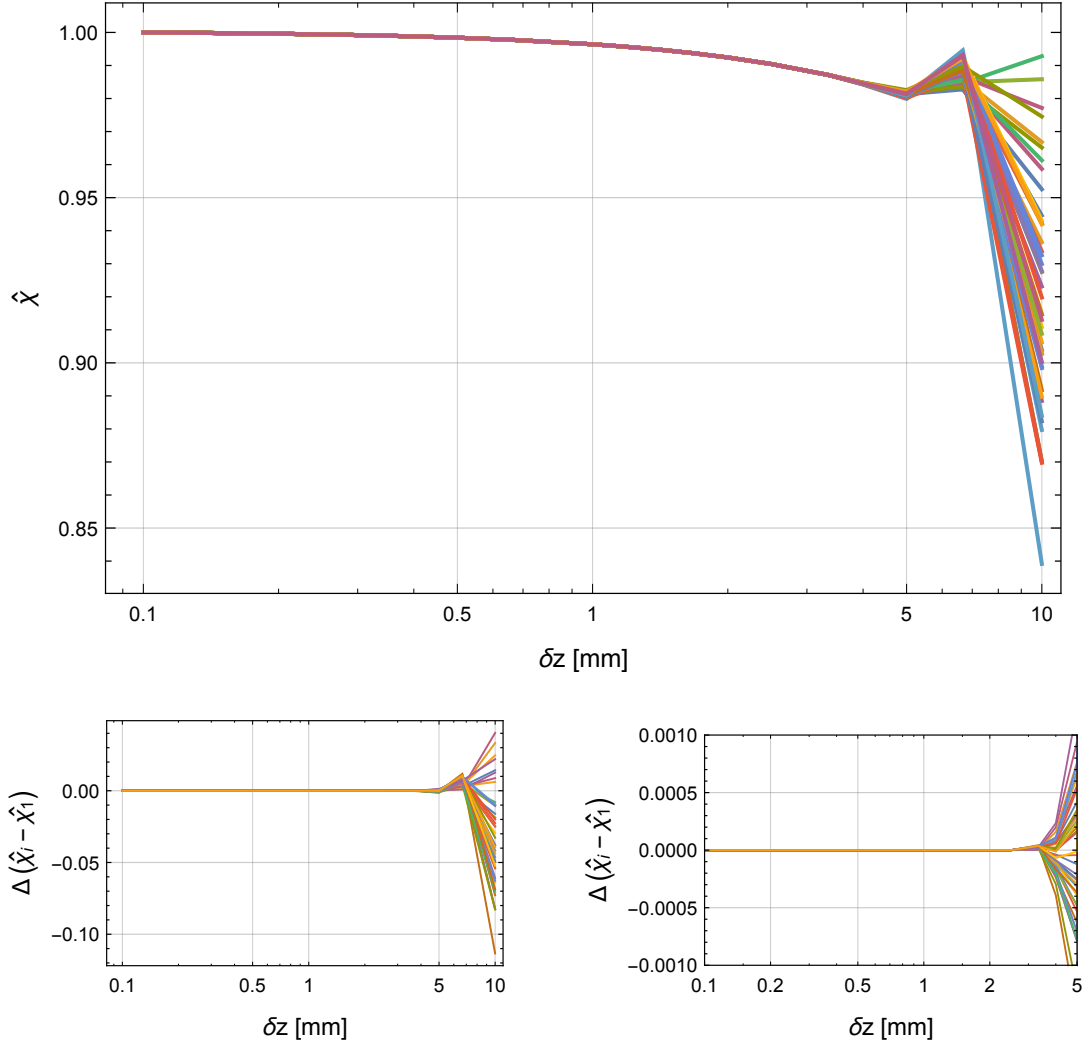


Figure 4.4: **Upper:** Convergence of the normalized field quality $\hat{\chi}$ depending on the step width δz along a magnetic field line for various arbitrarily chosen PMS assemblies. **Lower:** Convergence of the normalized field quality difference $\Delta(\hat{\chi}_i - \hat{\chi}_1)$ with respect to a certain PMS assembly depending on the step width δz along a magnetic field line. Shown are two different magnifications.

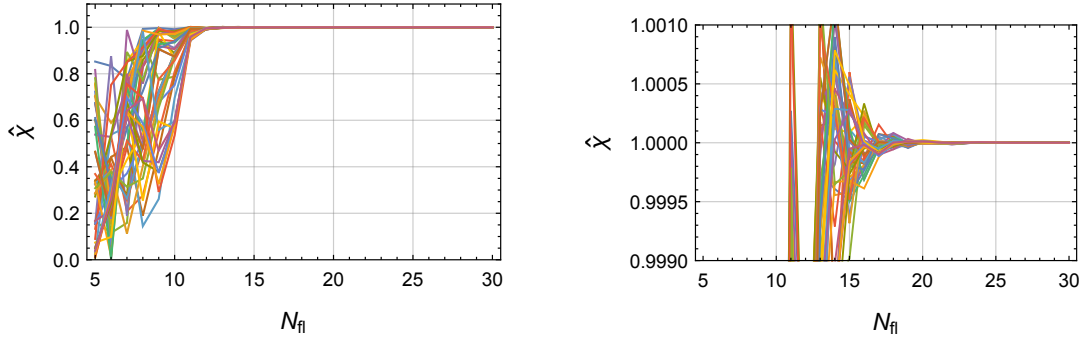


Figure 4.5: Convergence of the normalized field quality $\hat{\chi}$ depending on the number of magnetic field lines for various arbitrarily chosen PMS assemblies. Shown are two different magnifications.

probability

$$\exp\left(-\frac{Q(x_{\text{opt}}) - Q(x)}{T}\right).$$

Thus for low temperatures T the probability of choosing the permutation decreases, whereas for high T the algorithm tends to *jump* out of minima more often. This helps to avoid getting trapped in local minima.

The first part of the optimization algorithm has been written by myself. The second part has been developed by F. Mayet³.

Results

The best arrangement provided by the algorithm has been used to determine the emittance growth. Full 3D field maps were calculated for both the flawed and flawless wedge case using the analytical field model in order to perform particle tracking simulations using ASTRA. Because the emittance growth depends on the initial beam parameters the results are only valid and comparable for the chosen parameters. An artificial electron distribution has been used to probe the two independent assemblies. It is transversely circular normal distributed with an RMS width of 610 μm and a kinetic energy of 5 MeV. The initial transverse 4D emittance is equal to zero, meaning the distribution has no divergence and in addition no energy spread or longitudinal length. Therefore all changes of the emittance

³frank.mayet@desy.de

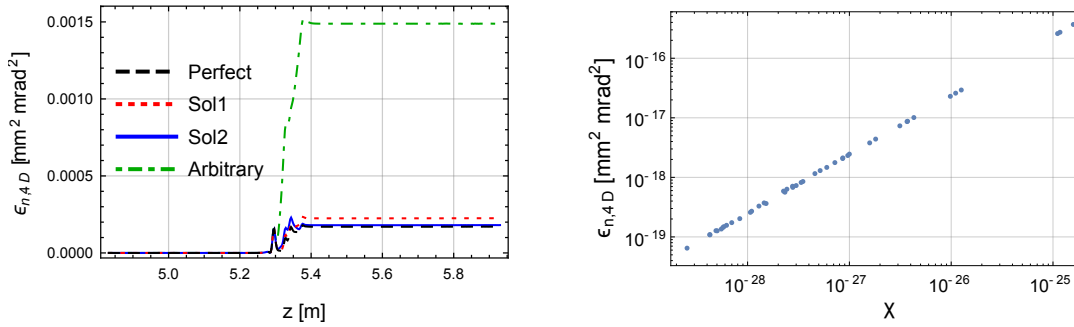


Figure 4.6: Left: Growth of normalized 4D emittance for different PMS assemblies. The PMS's center is placed at $z = 5.33$ m. **Right:** Correlation between the field quality χ used for the numerical sorting algorithm and the normalized 4D emittance tracked with ASTRA.

are caused by the PMS assembly. This includes the 'normal' emittance growth due to the non-linearity of the transverse magnetic fields as well as the additional contribution due to field imperfections caused by the flawed wedges.

Two PMS assemblies (Fig. 4.6, left) were found. Both are compared to a flawless assembled PMS to quantify the additional emittance growth caused by imperfections of the field. A relative 4D emittance growth $\epsilon_{\text{flawed}}/\epsilon_{\text{flawless}}$ of 1.32 and 1.05 could be achieved, respectively. An arbitrary assembly, for example, reaches a relative emittance growth of ~ 8.71 . Furthermore a strict correlation between the fitness quantity and the normalized 4D emittance can be shown. In Fig. 4.6 (right) the 4D emittance growth of 22 simulated assemblies, simulated with ASTRA again, and the calculated χ were plotted. It clearly shows the correlation between the full 4D phase-space emittance and the rather simple field quality factor χ . Depending on the assembly the emittance growth varies over orders of magnitude.

The introduced field quality criterion χ is independent of the type of magnet which has to be assembled. Only the geometrical arrangement of the field integrals has to be adapted to the specific field.

4.1.3 Field measurement

The introduced permanent magnetic assembly is not a usual and well known approach to realize a magnet. Hence, a validation of the design and simulations is required. A measurement of the magnetic field gives the opportunity to prove the concept. But as complicated as the design itself is as complicated is a field

measurement. In this section all steps from choosing the right test setup up to the post-processing of the taken data is described.

3D-Hall probe

Measuring the magnetic field of a geometrical small magnet with a high precision is challenging. In order to compare the field simulations with a measurement we decided for the Metrolab Three-axis Hall Magnetometer THM1176-HF [76] which provides the required accuracy. With a sensor housing of $5.1 \text{ mm} \times 1.3 \text{ mm}$ the geometrical dimensions of the probe are small enough to measure the magnetic field inside the PMS. Furthermore its small active volume of $(150 \times 150 \times 10) \mu\text{m}^3$ is sufficient to measure the absolute field despite the high field variation.

The Hall probe was calibrated relatively to an NMR Teslameter [77] which has an absolute precision of $\pm 5 \times 10^{-6}$ and a relative precision of $\pm 0.1 \times 10^{-6}$. Both probes have been setup inside a homogeneous magnetic field of a huge dipole magnet. The absolute as well as the relative accuracy meet our requirements of $\pm 10^{-4}$. From a linear regression of the absolute magnetic field of the Hall probe relative to the NMR Teslameter the absolute accuracy could be determined to be equal to $0.999\,98(9)$ with respect to the NMR Teslameter. The relative accuracy could be determined in dependence on the absolute magnetic field. The average relative accuracy is $1.08(3) \times 10^{-4}$. Both measurements are depicted in Fig. 4.7.

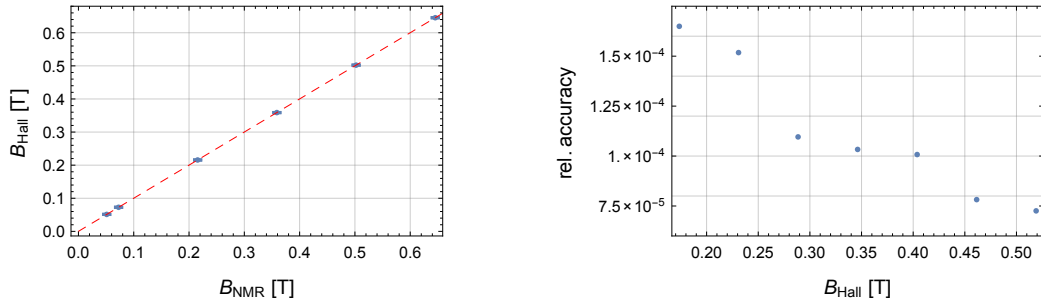


Figure 4.7: **Left:** 3D-Hall probe calibration of the absolute magnetic field measurement versus a NMR Teslameter measurement. The red dashed line shows the linear regression of the taken data. **Right:** Relative magnetic field measurement accuracy depending on the absolute magnetic field. The relative accuracy has been determined from 100 data points per adjusted magnetic field.

Magnetic field measurement and post-processing

The field measurements were done with a 3D linear stage with a minimal step size of $12.5\ \mu\text{m}$. The PMS was fixed on a triple-axis adjustment table. To do a proper field measurement it is necessary to align the the PMS and the Hall probe with respect to the linear stage. Hence, there are 9 degrees of freedom for the alignment: 3 translational (x_0, y_0, z_0) and 3 rotational degrees $(\beta_x, \beta_y, \beta_z)$ of the PMS with respect to the linear stage and 3 rotational degrees $(\alpha_x, \alpha_y, \alpha_z)$ of the Hall probe. The indices denote the rotation axes and (x, y, z) the horizontal, vertical and longitudinal axes, respectively.

The distinct shape of the solenoidal field (Fig. 4.8, upper) offers the possibility to align the linear stage and the Hall probe relatively to the magnetic field of the PMS. Hence it is helpful to recall the introduced polynomial series of the magnetic field of a solenoid in Eq. 2.28. Apparently, it can be seen that on-axis the radial field vanishes and the longitudinal field component has two zero-crossing points. Consequently, there are two points where the absolute magnetic field is equal to zero which are lying on the longitudinal magnetic axis. These can be used to align the PMS relative to the linear stage. Furthermore they define the orientation of the Cartesian grid. Another interesting point is the maximum on-axis magnetic field. First of all it is used to define the origin of the Cartesian coordinate system but secondly all odd derivations of $B_{z,\text{max}}(z)$ are equal to zero at this point. Thus, the transverse plane at the position of the maximum longitudinal field has only a longitudinal field component. This fact can be used to align the horizontal and vertical axes of the Hall probe (α_x, α_y) . Because the probe is fixed on a metal brace and cannot be adjusted this measurement is used for the post-processing correction of the field.

Due to the precision limit of the alignment during the field measurement a post-processing is necessary to compare simulation and measurement. Therefore, the aforementioned field simulation code has been extended by 3 rotational degrees for the PMS geometry, namely $(\beta_x, \beta_y, \beta_z)$. In order to determine the Hall probe misalignment first of all the Hall probe calibration (Fig. 4.7, left) has been applied as well as a background field measurement has been subtracted. The transverse plain at $B_{z,\text{max}}$ has been measured and the probe misalignment has been determined for each measured point. The averaged values are $\alpha_x = -7.41(4) \times 10^{-3}$ rad and $\alpha_y = 4.43(4) \times 10^{-3}$ rad.

Because the measured as well as the simulated field grid is rectangular the 3 trans-

lational degrees (x_0, y_0, z_0) are introduced as a shift of the simulated field with respect to the measured one. Accordingly the resolution of the simulated field has to be higher. As a consequence, the translation alignment is discrete and not quasi-continuous like the rotational alignment. The rotation around the longitudinal axis of the probe α_z has not to be introduced to the simulation code. It has been applied afterward to the simulated field as a simple rotation of the field vector around the z -axis.

For the fitting routine a simple least-square criterion [41] has been chosen:

$$\chi^2 = \sum_i^N \frac{(\mathbf{B}_{m,i} - \mathbf{B}_{s,i})^2}{\sigma_{\mathbf{B}}}$$

where \mathbf{B}_m is the measured magnetic field vector, \mathbf{B}_s is the simulated magnetic field vector, $\sigma_{\mathbf{B}}$ is the standard deviation of the repeatedly measured field and N is the sample size. In order to proof the goodness of the fit the *reduced chi-squared* $\tilde{\chi}^2 = \chi^2 / (N - n - 1)$ (Eq. 2.39) is introduced which should be close to 1.

The field of one PMS has been measured and compared to both assembled PMS models as well as to the ideal PMS model with flawless wedges. The step size of the measured grid was $(0.5 \times 0.5 \times 2) \text{ mm}^3$. The results of the fits are shown in Tab. 4.1. The resolution of the simulated grid was $(0.1 \times 0.1 \times 0.4) \text{ mm}^3$ which defines the minimal translation step widths of the fit routine.

The congruence of the simulated and measured field is exemplarily shown with certain line plots in Fig. 4.8 and Fig. 4.9. In addition to the on-axis longitudinal field itself the absolute as well as the relative deviation of the corrected measured field from the simulated is shown in Fig. 4.8. For the interesting interval $[-100, 100] \text{ mm}$ the relative field deviation is below 2% excepting close to the zero crossings where it is understandably larger. Especially the deviation of the measured field at position of high field variation can be seen in Fig. 4.9. The congruence between the measured and simulated field is getting worse at the local extrema of the field. Taking the challenging circumstances into account the agreement of the measured and simulated field is good. Only the peak field is lower than expected. The design maximum field is $B_{z,max} = 0.4429 \text{ T}$ - the measured is $B_{z,max} = 0.4199 \text{ T}$. This reduces the focus strength by $\sim 10\%$.

Even if the field imperfections of the PMS could not be resolved the field measurement itself is in good agreement with the simulated field. With a measurement the assembled PMS is indistinguishable from a flawless PMS assembling. The only

chance to determine the field quality differences could be a beam based measurement at REGAE. The study of the PMS including the field model, the sorting algorithm and the field measurement has yielded excellent results so far. It remains to observe the performance and behavior of the PMS under realistic conditions at REGAE.

Table 4.1: Comparing fit results for both PMS assemblies as well as for the ideal solenoid model with flawless wedges.

	PMS 1	PMS 2	Ideal
x [mm]	0.00(5)	0.00(5)	0.00(5)
y [mm]	0.00(5)	0.00(5)	0.00(5)
z [mm]	0.0(2)	0.0(2)	0.0(2)
$\beta_{\mathbf{x}}$ [rad]	$4.0(5) \times 10^{-4}$	$4.0(5) \times 10^{-4}$	$4.0(5) \times 10^{-4}$
$\beta_{\mathbf{y}}$ [rad]	$\pi + 0.002\,70(5)$	$\pi + 0.002\,70(5)$	$\pi + 0.002\,70(5)$
$\beta_{\mathbf{z}}$ [rad]	$0.0520(5)\pi$	$1.7182(1)\pi$	-
$\alpha_{\mathbf{x}}$ [rad]		$4.7(4) \times 10^{-3}$	
$\alpha_{\mathbf{y}}$ [rad]		$-7.8(4) \times 10^{-3}$	
$\alpha_{\mathbf{z}}$ [rad]	$\pi + 0.017\,20(5)$	$\pi + 0.017\,80(5)$	$\pi + 0.017\,20(5)$
$\tilde{\chi}^2$	3.38	3.38	3.52

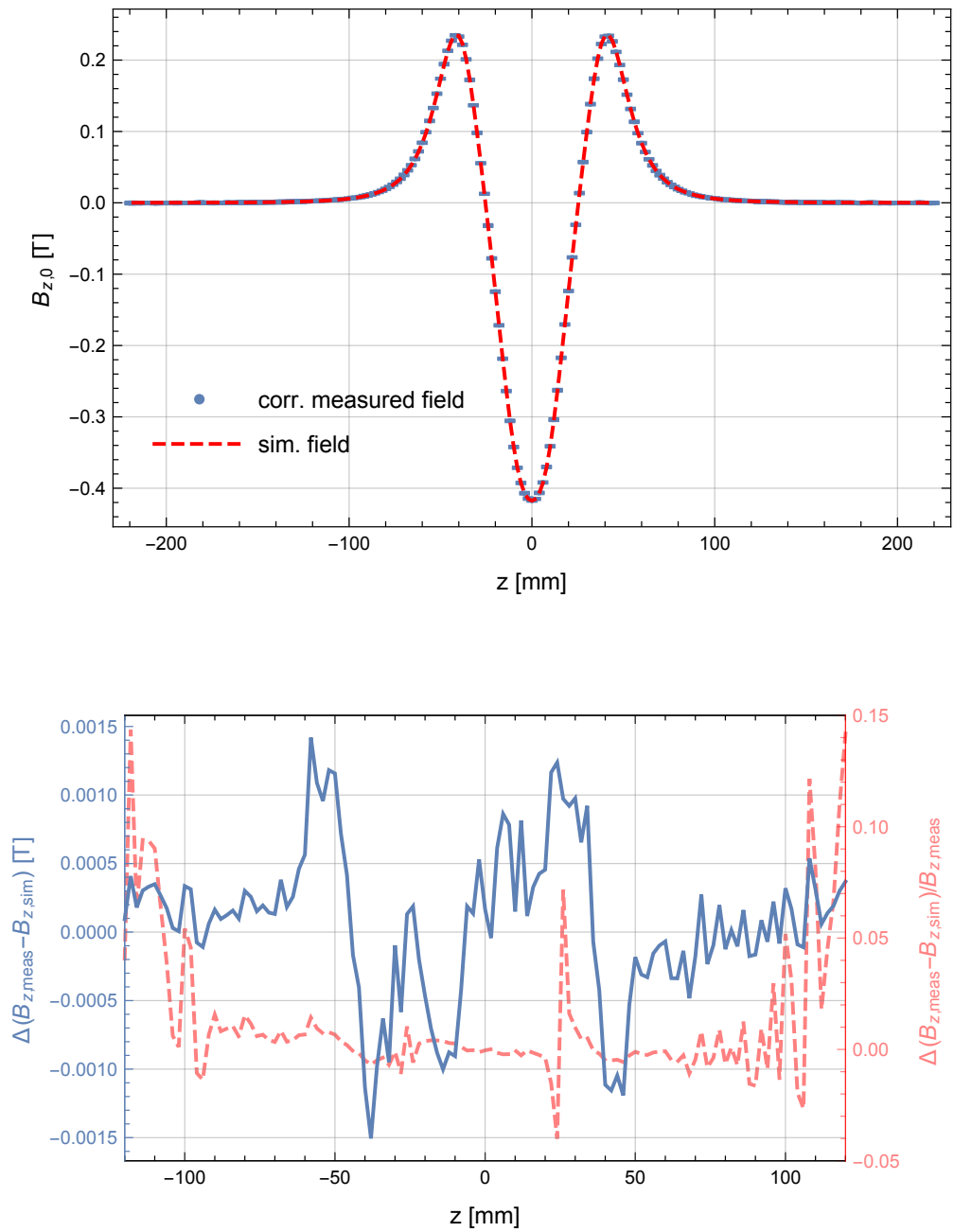


Figure 4.8: Upper: Measured and simulated on-axis longitudinal magnetic field $B_{z,0}(z)$. Lower: Field difference of measured and simulated field (solid blue) and relative field deviation (dashed red) of the measured field with respect to the simulated field.

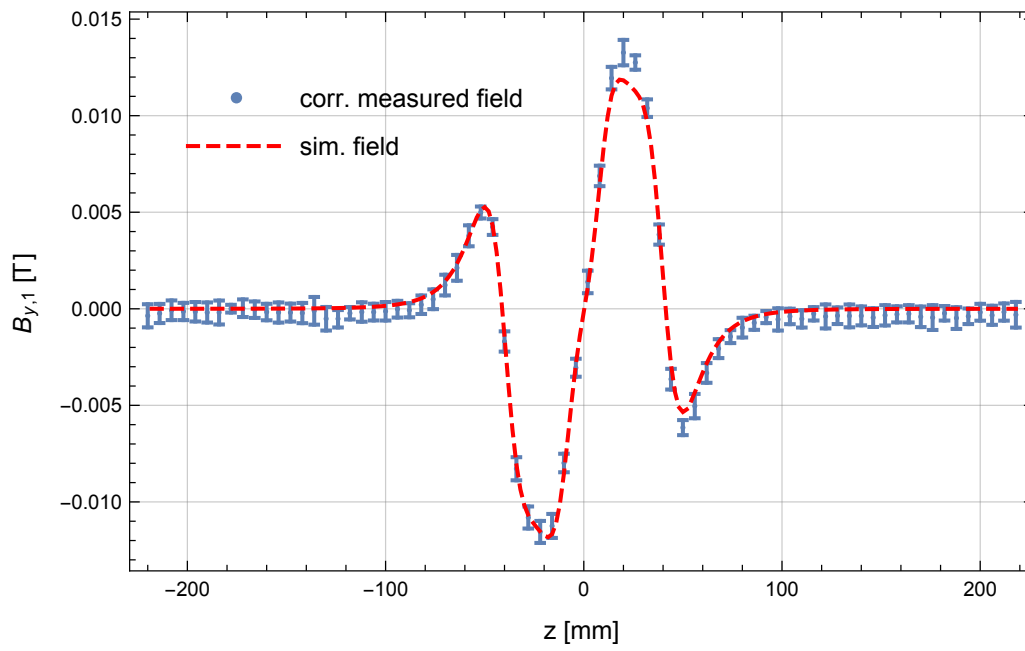


Figure 4.9: Measured and simulated off-axis ($y = 0$, $x = 1$ mm) transverse magnetic field $B_{y,1}(z)$.

4.2 ASTRA simulations of the external injection into a plasma wakefield

In this section an injecting scheme for the laser plasma acceleration experiment at REGAE will be presented. The PMS are assumed to be integrated in the transverse optics of REGAE and it will be shown that the requirements to inject a REGAE electron beam into a plasma wakefield can be fulfilled. It can be shown that the beta function β_m (Eq. 2.26) has to be matched to the plasma wakefield conditions in order to conserve the transverse emittance of the electron beam [78]. And still, these requirements are extremely challenging. By adding a matching region [79, 80] in front of the actual plasma wakefield these demands can be relaxed. The matching region is realized by a up-ramping plasma density profile. The results of [78–80] will be used to determine the transverse beam parameters at the injection point. In parallel to the strong transverse focusing a longitudinal short bunch (~ 10 fs) is required at the injection point as well. But effectively the machine settings just need to be slightly adapted in comparison to the standard settings to still reach a bunch length below 10 fs.

Besides the analytical description of the injection into a plasma wakefield at REGAE an full start-to-injection point ASTRA simulation of the REGAE linac will be presented which merges the analytical found results with the capability of REGAE to achieve the required demands.

4.2.1 Adiabatic matching of an electron bunch into a laser plasma wakefield

Table 4.2: Relevant design parameters for the external injection experiment at REGAE. Table originates from [10], only the electron beam parameters has been adapted.

Plasma		Laser		Electrons	
Density	$n_e = 10^{16} \text{ cm}^{-3}$	Strength	$a_0 = 0.75$	Energy	$\langle T \rangle = 5.1 \text{ MeV}$
Wavelength	$\lambda_p = 334 \text{ }\mu\text{m}$	Beam waist	$w_0 = 42.5 \text{ }\mu\text{m}$	Bunch charge	$Q = 100 \text{ fC}$
Peak field	$E_z = 789 \frac{\text{MV}}{\text{m}}$	Rayleigh length	$z_R = 3.1 \text{ mm}$	Beam size	$r_{\text{RMS}} \approx 3 \text{ }\mu\text{m}$
Plateau	$L_{\text{pt}} = 25 \text{ mm}$	Pulse length	$\tau_{\text{FWHM}} = 100 \text{ fs}$	Bunch length	$z_{\text{RMS}} \approx 9 \text{ fs}$
Ramp	$L_{\text{ur}} = 5 \text{ mm}$	Wavelength	$\lambda = 815 \text{ nm}$	Norm. emittance	$\epsilon_n = 16 \text{ nm rad}$

The analytical description of the plasma wakefield in the linear regime has been introduced in Sec. 2.3. The following description of the injection into a plasma wakefield for the REGAE experiment is based on the analytical description of the wakefields and the resulting transverse focusing strength. Tab. 4.2 introduces the laser, plasma and electron beam parameters used for this study.

It is the aim to inject an electron bunch into a plasma wakefield in a controlled way in order to conserve the transverse beam emittance $\epsilon_{x,y}$. This can be achieved if certain conditions, regarding the interplay of plasma and beam parameters, are fulfilled. Normally, the strong focusing of the wakefield (Eq.2.44) would introduce a phase advance (Eq. 2.25) depending on the accelerating phase, meaning the rotation inside the phase space of each bunch slice would depend on its longitudinal position inside the bunch. Consequently, slices of the phase space distribution would start to shear inside the phase space differently with respect to other slices. The projected phase space area of all these slices would be consequently larger, meaning the emittance would be larger. But under certain conditions the occupied phase space can stay constant. The emittance itself drives the expansion of the tightly focused bunch. The strong focusing wakefield counteracts this trend. If both are balanced the phase space ellipse stays as it is. The electrons still experience a phase advance but only moving along the 'frozen' phase space ellipse. As a consequence the emittance is constant. This condition is fulfilled if the beta function (Eq. 2.24) is equal to

$$\beta_m(\xi) = \beta_0 \sqrt{\frac{K_0}{K(\xi)}}, \quad (4.3)$$

where K_0 and β_0 are the values of the corresponding functions at the laser focus position. The focus strength $K(\xi)$ is equivalent to Eq. 2.44 where ξ is the relative longitudinal coordinate of the co-moving frame of the plasma wakefield.

In the following the injection including the new beam optics at REGAE will be discussed. It should be mentioned that the extraction is not part of this study. But it is as complex and complicated as the injection. The differently rotating beam slices are not shearing inside the plasma wakefield if the beam is matched but as soon as the beam leaves the plasma wakefield the slices start to shear which causes an emittance growth in the transversal [80, 81]. Therefore it is necessary to capture the beam as soon as it leaves the plasma. Besides a tailored plasma density profile at the plasma exit to reduce the slices' divergence, magnets could be placed as close as possible. Hence, a second PMS can be placed directly behind

the plasma target at REGAE.

For the REGAE injection experiment a linear density up-ramp profile has been chosen before its transition into a constant density. The up-ramp profile is used as a so called *adiabatic matching* region. Adiabatic means in this context that the optical functions evolve slowly compared to the phase advance along the ramp so that electrons experience a full revolution inside the phase space while the optical functions β and α are in good approximation constant. Then the optical functions has to be matched only at one position along the plasma and will be guided by the focusing fields automatically in a matched way. The matching region is meant to add a smooth focusing into the actual plasma wakefield. That consequently relaxes the beam parameters at the injection point. Without the adiabatic matching region a matched beta function $\beta_{m,0}$ of 0.25 mm or respectively a beam size of 0.6 μm has to be achieved at the focus of the laser pulse. Fig. 4.10 illustrates on the one side the plasma density profile and on the other side the laser beam size evolution $w(z)$ inside the plasma which has been introduced in Eq. 2.44 already. For a Gaussian shaped laser pulse it is given as

$$w(z) = w_0 \sqrt{1 + \frac{z^2}{z_R^2}} \quad (4.4)$$

where z_R is the *Rayleigh length*. The amplitude of the vector potential $a(z)$ evolves anti-proportionally to the beam size $w(z)$:

$$a(z) = a_0 \frac{w_0}{w(z)}.$$

Furthermore, the analytical solution of the adiabatic matched beta function (dash-dotted red; Eq. 4.3) and the tracked solution are depicted. The analytically matched beta function diverge dramatically if $K(\xi)$ is close to zero. It can be observed in Fig. 4.10. Instead a numerically tracked solution delivers a reasonable result. The strategy to find the solution is to calculate the required beta function $\beta_{m,0}$ at the focus of the laser and then subsequently tracking the electron distribution stepwise backwards out of the plasma. For the tracking the transfer matrix from Eq. 2.18 has been used. For each step the focus strength K and the corresponding transfer matrix have been calculated depending on the laser beam waist and vector potential. The plasma phase $k_p \xi$ in this particular solution has been chosen to be equivalent to $-\pi/2$ at the laser focus. According to Fig. 2.4 this is the phases of maximum focusing.

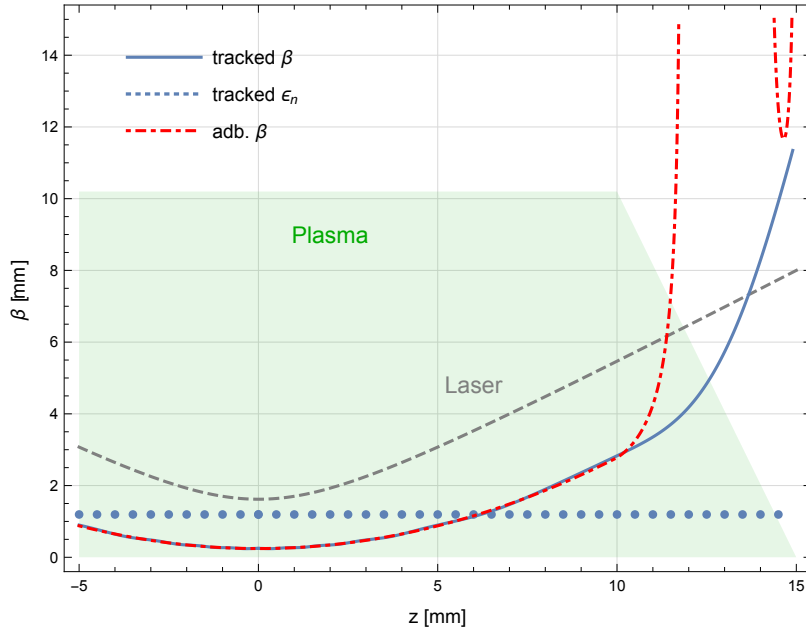


Figure 4.10: Illustration of the adiabatic injection of an electron bunch into a laser-driven plasma. The longitudinal axis is inverted. Positive z values direct upstream of the beamline. In addition to the plasma density (green) and the laser envelope (gray) two differently yielded beta functions are plotted. The analytical solution (dash-dotted red) diverges due to numerical issues. The tracked solution does not have these issues and illustrates the correct beam envelope. Furthermore the transverse beam emittance (dotted blue) has been tracked and stays constant.

4.2.2 Electron optics to focus into a plasma wakefield at REGAE

For the ASTRA simulation the standard RF and cathode laser settings as for the design simulation of REGAE, introduced in Sec. 1.1, have been used. The longitudinal electron beam focus is close to the interaction region inside the target chamber. Only the transverse optics has to be adopted to match the requirements of the external injection. This includes the focusing strength of the electrical solenoids (Sol1,23,45) as well as the position of the permanent magnetic solenoid (PMS) which can be controlled by the in-vacuum movers [10].

The aim is to achieve the optical functions obtained from the analytical tracking

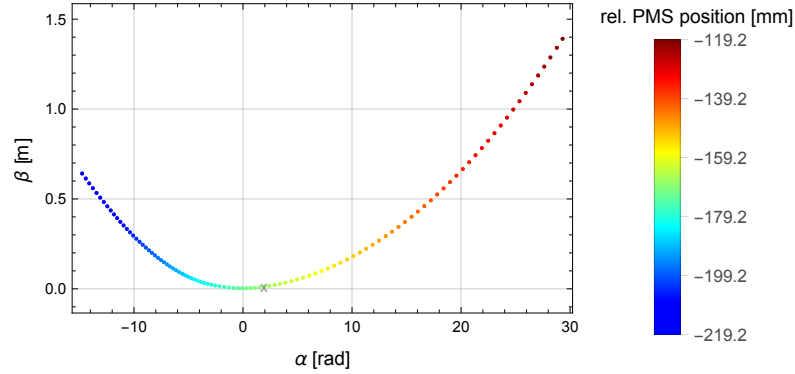


Figure 4.11: β and α function depending on PMS position. The required $\beta = 11.7$ mm and $\alpha = 1.94$ values are marked with a cross. The PMS position is given with respect to the beginning of the plasma up-ramp in Fig. 4.10 ($z_{\text{in}} = 5.519$).

of a REGAE bunch out of the plasma wakefield for the given set of laser, plasma density and electron bunch parameters introduced in Tab. 4.2. The electron beam parameters have to match at the entrance of the plasma with the results from the analytical tracking out of the plasma which are $\beta = 11.7$ mm and $\alpha = 1.94$. The focus strength of Sol1 to Sol45 has been adopted just a bit. The 'fine tuning' has been done with the position of the PMS. The scan is shown in Fig. 4.11. Related β and α pairs at the injection point of the plasma are plotted. The color code represents the PMS position relative to the injection point. The PMS position has been scanned in a range of 10 cm. The required β and α are achievable but the optical functions are quite sensitive to the PMS position. Using the found PMS position a full start-to-injection simulation with ASTRA has been done. It is shown in Fig. 4.12.

Due to the adiabatic matching scheme it is only necessary to reach the right beam parameters at the injection point which is in case of this simulation close to the center of the target chamber at $z_{\text{in}} = 5.519$ m. The achieved electron beam parameters are listed in Tab. 4.3. Because the longitudinal focus is pretty smooth and robust it is not necessary to match it exactly to the injection point, even if it fits well for this particular study. The bunch length is below the required 10 fs.

Going more into the details of the simulation illustrated in Fig. 4.12 a tremendous increase of the transverse emittance inside the PMS is observable. It is caused

Table 4.3: Electron beam parameters at injection point $z_{\text{in}} = 5.519$ m.

z_{in} [m]	5.519
z_{RMS} [$\mu\text{m}/\text{fs}$]	2.64/8.81
β_{x} [mm]	11.7
α	1.94
$\epsilon_{\text{n,x}}$ [π mm mrad]	0.0166
E_{kin} [MeV]	5.099

by the implementation of the PMS field map in Cartesian coordinates. Normally, electron bunches are tracked in canonical coordinates inside a solenoid in ASTRA. This is in case of the PMS magnetic fields not possible. In Cartesian coordinates the correlations between the transverse directions are not considered and an emittance growth is the consequence. Because the correlations vanish when the beam is leaving the solenoidal field, the emittance is correct after the solenoid. Therefore the observable emittance growth inside the PMS field is not real. This can be easily verified by calculating the 4D transverse emittance, where all correlations between the horizontal and vertical phase spaces are included. To compare the 2D and 4D emittance the squared horizontal normalized emittance $\epsilon_{\text{n},x}^2$ is used (assuming that the horizontal and vertical emittance are equal). It should be equal to the 4D normalized transverse emittance. Fig.4.13 shows the comparison of both emittances inside the PMS and around the injection point. Outside the PMS field the 4D emittance and the squared 2D emittance coincide very well. The 4D emittance shows an emittance growth inside the PMS field as well but this is expected due to the non-linear fields of the PMS.

The results of the analytical tracking out of the plasma and the ASTRA simulations can be combined to show the transition of the REGAE electron beam into the plasma wakefield. The tracked ASTRA beam as well as the analytical solution are plotted altogether in Fig. 4.14. Both solutions overlap along the adiabatic matching region. The matching of a REGAE electron bunch into a plasma wakefield is fundamentally possible using the introduced *permanent magnetic solenoids*. The experimental implementation will be still challenging. There are some circumstances which have been ignored in this study but have been done in full detail

in [10, 25]. First of all the laser overtaking of the electron bunch has to be mentioned. Due to the geometrical circumstances at REGAE it is unavoidable that the laser pulse has to overtake the electron bunch before entering the plasma target. This will of course effect the electron bunch. A detailed study can be found in [10]. Another difficulty will be the stability of all involved sources, meaning the electron as well as laser beam arrival as well as the pointing of both. [10] as well as [25] address this issue. The expected jitters are manageable and should not be a show-stopper for the external injection experiment at REGAE.

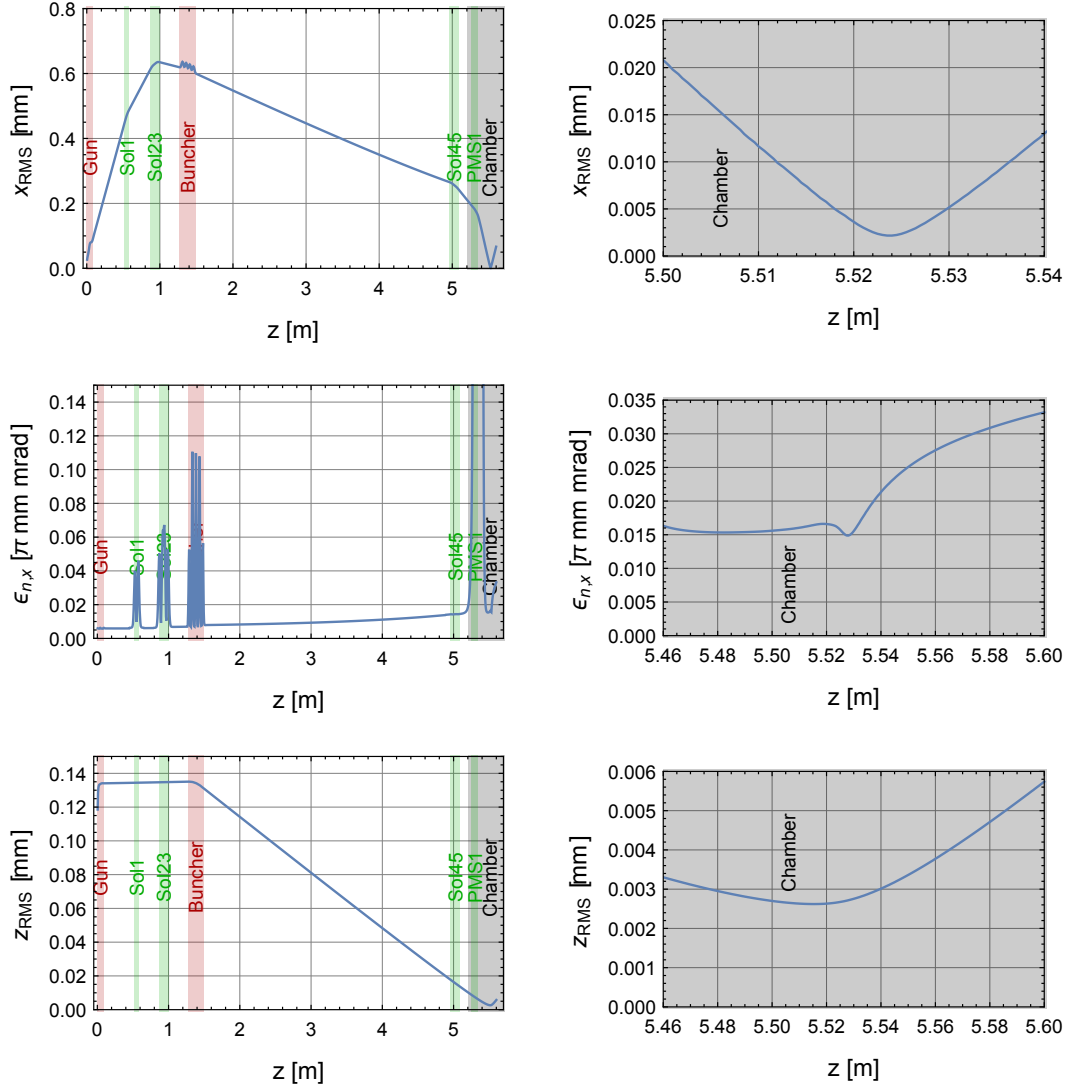


Figure 4.12: The full start-to-injection simulation is shown. The left column shows the hor. RMS beam size x_{RMS} , the hor. norm. emittance $\epsilon_{n,x}$ and the bunch length z_{RMS} from the cathode to the injection point. The right column shows the same quantities but zoomed into the injection point ($z_{\text{in}} = 5.519$ m). The PMS is placed at $z_{\text{PMS}} = 5.352$ m.

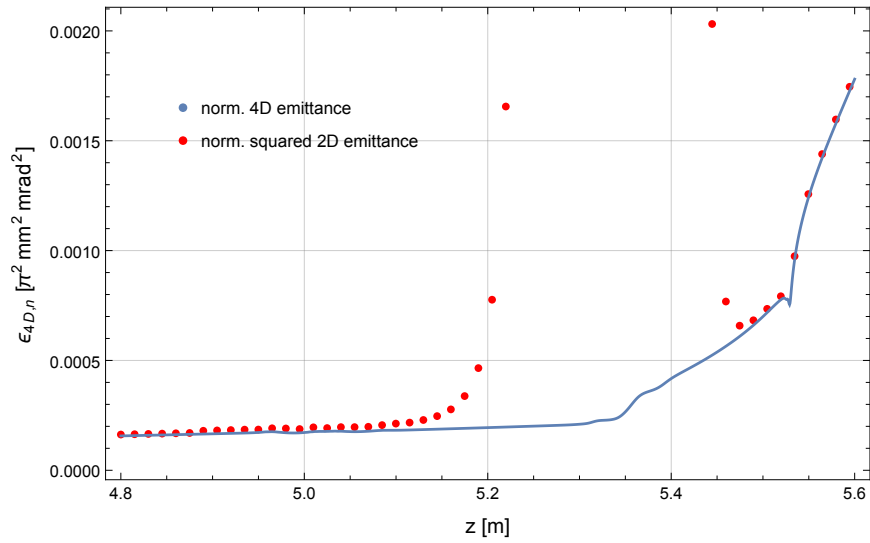


Figure 4.13: Comparison of the 4D normalized emittance (solid blue) and the squared 2D normalized emittance (dotted red) inside the PMS and around the focus position. The influence on the 2D emittance due to the PMS is clearly visible. The PMS is centered at $z = 5.352$ m.

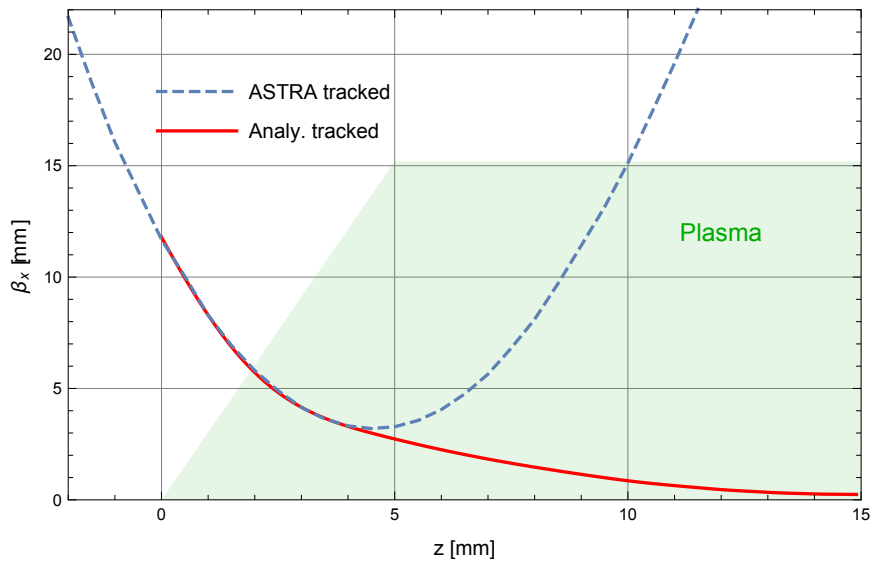


Figure 4.14: Tracked β_x with ASTRA (dashed blue) and the analytically determined matched $\beta_{x,m}$ (solid red) at the injection point. Here the injection point is $z_{in} = 0$.

Transverse Emittance Measurements and Simulations of a low charge electron bunch at REGAE

The results and insights into the principle difficulties of an emittance measurement using the magnet scan method (Sec. 2.1.4) have been discussed in the former chapters and can now be used for the emittance measurements at REGAE to perform highly precise measurements. Some results have been already published in [82,83]. The following sections demonstrate the capabilities, on one side of the developed image post-processing routine and on the other side of the REGAE accelerator to meet the design parameters (Sec. 1.1). Furthermore ASTRA simulations are shown to demonstrate the great agreement of the machine setup and the simulations. It proves the validity of the measurement but as well the validity of the simulations. These results could have been achieved for fundamentally different machine or more precise gun setups. The usage of different photo cathodes in the gun cavity offers quite different electron beam parameters directly at the beginning. Different quantum efficiencies and work functions of the cathode material generate even with constant laser pulse parameters still quite different electron phase space distributions right at the cathode. Two different setups will be introduced and the achieved transverse emittances are discussed.

The last section of this chapter is dedicated to the long-term observations at RE-

GAE and is directed to the machine conditions during the measurement period. A stable machine operation and a well known machine setup as well as cathode laser parameters are required to achieve and guarantee a small emittance but they were not always given and were probably the most disturbing problems at REGAE.

5.1 Emittance measurements at REGAE

In this section different results of emittance measurements done at REGAE are presented. Due to a repaired vacuum leak of the gun cavity in 2013 only moderate field gradients up to 60 MV/m could be achieved during the period of this work. Therefore the effects of space charge and their contribution to the emittance growth inside the gun cavity as well as during the beam transport are assumingly larger compared to the design studies of REGAE. To reduce the effects of space charge a lower bunch charge has been chosen which is in terms of the beam diagnostics for the emittance measurement not a big issue but for any kind of experiments bunch charges down to a few fC are not preferred. This includes the diffraction as well as the LPA experiments.

As introduced in Sec. 2.1.4 emittance measurements based on the magnet scan method have been performed to determine the transverse beam emittance. The phase advance between a solenoid and the detector screen has been subsequently scanned and the transverse beam profile has been recorded accordingly. The evaluation of the taken images has been done as described in Sec. 3.2.3. The distinct beam halo is treated as an artifact of the detector system and is consequently ignored for the calculation of the RMS beam size of the electron beam.

Besides measurements with the usual machine setup, measurements with a varying setup, including a different cathode and the application of the beam collimators, are presented and discussed. So far, the last setup achieved the best results at REGAE.

5.1.1 Standard measurement via a solenoid scan

An exemplary emittance measurement is shown in Fig. 5.1. The measured mean beam energy was $E_{\text{kin}} = 2.45 \text{ MeV}$. The bunch charge was equal to $Q_{\text{bunch}} = 37.6(6) \text{ fC}$. The results of the least-square fit are shown in Tab. 5.1. The goodness of the fit is estimated by the *reduced chi-squared* $\tilde{\chi}^2$ (introduced in Eq. 2.39) which

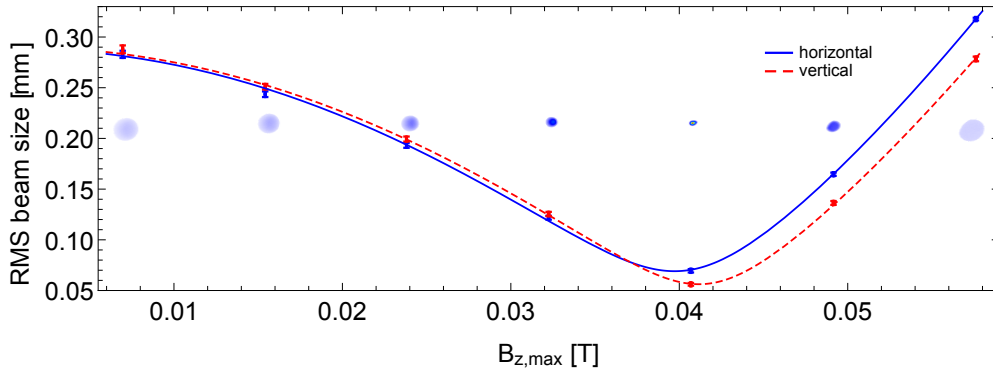


Figure 5.1: Measured beam size at D1 detector in dependence on the maximum magnetic field $B_{z,\max}$ of solenoid Sol67. Solid lines represent least-square fits which have been done with the introduced method in Sec. 2.1.4. The 2D-beam profile of each data point is depicted in the background.

should tend to one.

As mentioned in Sec. 3.1 the spatial resolution of the the D1 detector system is good enough for the purposes at REGAE. The presented measurement shows one of the smallest beam sizes ($\sim 50 \mu\text{m}$) which has been achieved at the position of D1. Due to the distances between the solenoids and the detector the spatial resolution of D1 is sufficient for almost every machine setup and beam parameter set. This observation can be analytically verified. The minimal achievable RMS beam size at a position z can be derived directly from the envelope equation of a drift

$$x_{\text{RMS}}^2 = x_{0,\text{RMS}}^2 + 2x_{0,\text{RMS}}(x_{0,\text{RMS}})'z + \left(\frac{\epsilon_x^2}{x_{0,\text{RMS}}^2} + (x_{0,\text{RMS}}')^2 \right) z^2 \quad (5.1)$$

which can be found by introducing the transfer matrix of a drift (Eq. 2.19) into the fundamental envelope equation (Eq. 2.22). Here, the initial parameters $x_{0,\text{RMS}}$ and $(x_{0,\text{RMS}})'$ represent the beam parameters directly behind a solenoid. The solenoid itself is approximated by the thin lens approximation (Eq. 2.20). Hence, $x_{0,\text{RMS}}$ is the ingoing as well as outgoing beam size of the solenoid. Whereas $(x_{0,\text{RMS}})'$ is defined by the focus strength of the solenoid. The envelope equation of a drift has been taken for its simplicity. Of course this consideration can be extended by the transfer matrix of a solenoid. But here this simple consideration of a drift is sufficient. Differentiating Eq. 5.1 with respect to $(x_{0,\text{RMS}})'$ and set the result equal

5 Transverse Emittance Measurements and Simulations of a low charge electron bunch at REGAE

to zero yields the specific initial envelope slope $(x_{0,\text{RMS}})'_{\text{min}}$ to achieve the minimal beam size $x_{\text{RMS},\text{min}}$ at a position z . For the REGAE case the position z can be replaced by the shortest distance of a solenoid to D1 which is Sol67 to D1 and will be called l_D .

$$\left. \frac{\delta x_{\text{RMS}}^2}{\delta (x_{0,\text{RMS}})'} \right|_{z=l_D} = 0 \quad \Rightarrow \quad (x_{0,\text{RMS}})'_{\text{min}} = -\frac{x_{0,\text{RMS}}}{l_D}. \quad (5.2)$$

Introducing this result into the envelope equation Eq. 5.1 yields:

$$x_{\text{RMS},\text{min}} = \frac{\epsilon_x}{x_{0,\text{RMS}}} l_D. \quad (5.3)$$

The minimal beam size at a certain position depends on the initial beam size $x_{0,\text{RMS}}$, the distance between the solenoid and the detector l_D and the emittance ϵ_x . A small emittance or distance as well as large initial beam size cause a small beam size. Eq. 5.3 has been used to generate the curves of Fig. 5.2 which supports the observed minimal beam size at REGAE's D1 detector. Only for an ultra low emittance and under certain initial beam parameters the spatial resolution of the detector system is not sufficient. But it is important to notice that large beam sizes, which would be required to undercut the detector resolution, are unwanted at the position of the solenoid. Because the non-linearity of the solenoidal field is causing an emittance growth depending on the beam size. Usual beam sizes at the solenoids are in the range of a few hundred μm .

Going back to the presented measurement of Fig. 5.1 the fit results of the mea-

Table 5.1: Least-square fit parameters and uncertainties of a solenoid scan at REGAE.

fit parameters	horizontal	vertical
ϵ_n [π mm mrad]	0.0271(7)	0.0209(8)
$\mathbf{x}_{0,\text{rms}}$ [mm]	0.244(1)	0.231(1)
$(\mathbf{x}_{0,\text{rms}})'$ [μrad]	12.8(3)	17.7(3)
$\tilde{\chi}^2$	2.7	1.2

surement in Tab. 5.1 show small errors and $\tilde{\chi}^2$ is at least in the vertical direction close to one. The errors are a consequence of the introduced errors to the fit model. For the calculation of the errors, on the one side the statistical errors of the beam size determination and on the other side the machine setting based errors (like

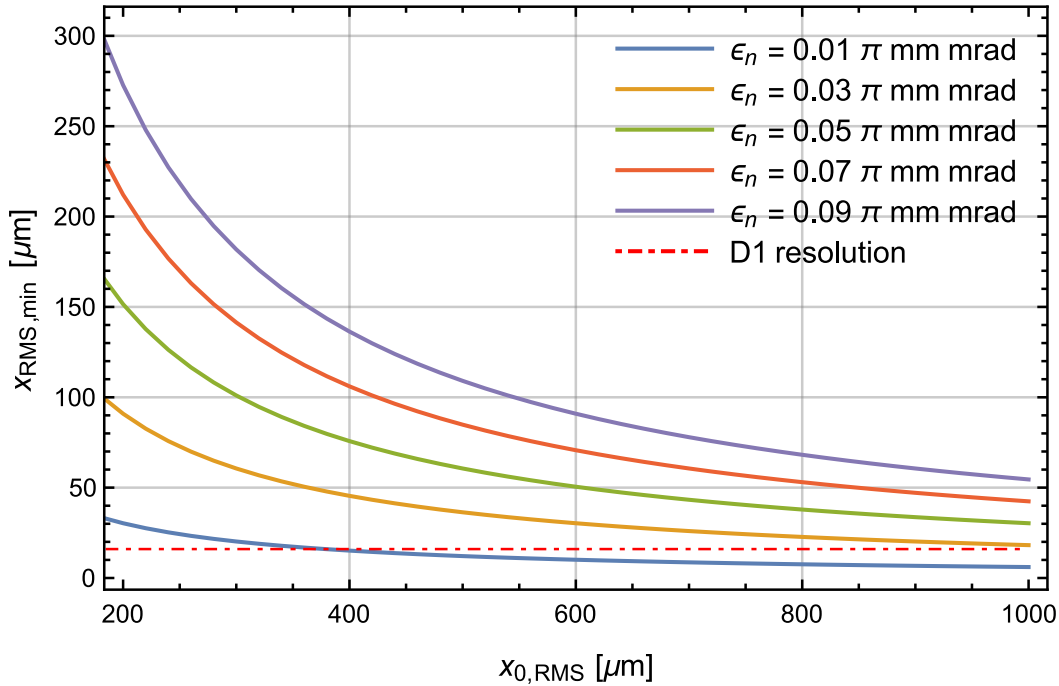


Figure 5.2: Minimal RMS beam size $x_{\text{RMS,min}}$ depending on the initial beam size $x_{0,\text{RMS}}$ and the beam emittance ϵ_n at position of the D1 detector system. The exit of Sol67 has been chosen as the initial beam position. The drift distance l_D is equal to 3.52 m. In addition the red dot-dashed line marks the spatial resolution of the D1 detector system ($\sim 16 \mu\text{m}$).

solenoid current, mean beam energy) are used. The measured beam sizes coincide very well with the beam envelope model used for the least-square fit.

5.1.2 Emittance measurements of a collimated electron beam

For a period during 2015 the usually used gun cathode, made of molybdenum, has been replaced by a cesium-telluride cathode which has a much higher quantum efficiency compared to the former cathode. Bunch charges up to several pC could be achieved easily. The much higher bunch charges right at the beginning causes initially a larger transverse and longitudinal emittance at the cathode due to space charge effects. To compensate this effect in the transverse directions the beam has

been collimated strongly direct behind the gun cavity. Bunch charges down to a few fC could be achieved with the installed beam collimators at DDC1. Because the phase space distribution has been massively cut in the spatial directions the beam emittance shrinks as well. The main drawback of this method is the larger longitudinal emittance which limits the ability to focus the beam in the longitudinal direction. But for the transverse beam dynamics an overall positive effect has been observed. During this period the smallest transverse emittance could be measured.

In this context the usage of collimators and the influence on the emittance have been investigated. The reduced beam size due to the collimator causes a reduced emittance as well (Eq. 2.9). The resulting emittance from different collimator diameters is shown in Fig. 5.3. At the same time as the beam size and consequently the bunch charge are reduced, space charge effects are reduced as well. Hence, the reduced emittance is probably not a pure effect of the beam size reduction. Nevertheless the smallest normalized transverse emittance has been achieved with the described machine setup at REGAE. It was 9π mm mrad at a bunch charge of 13.7 fC.

Besides the small emittance another benefit occurs intrinsically. Collimators with a smaller aperture could be used. That reduces the transported dark current generated at the gun to a minimum. This instantly increases the signal-to-noise ratio at the detector and made it possible to perform an emittance scan with just 13.7 fC - that is almost the lower resolution limit of the installed charge monitor DaMon. For experiments which do not require the shortest possible bunch, this setup is a good alternative to the usual machine setup. In addition the electron beam quality just slightly depends on the cathode laser pulse parameters. For the standard machine setup the beam quality is defined right from the beginning by the laser pulse at the cathode. Therefore a good control of the laser needs to be achieved. This could not be guaranteed at REGAE in the past. So that during the period of using the cesium-telluride cathode a high reliability of the electron beam parameters could be achieved.

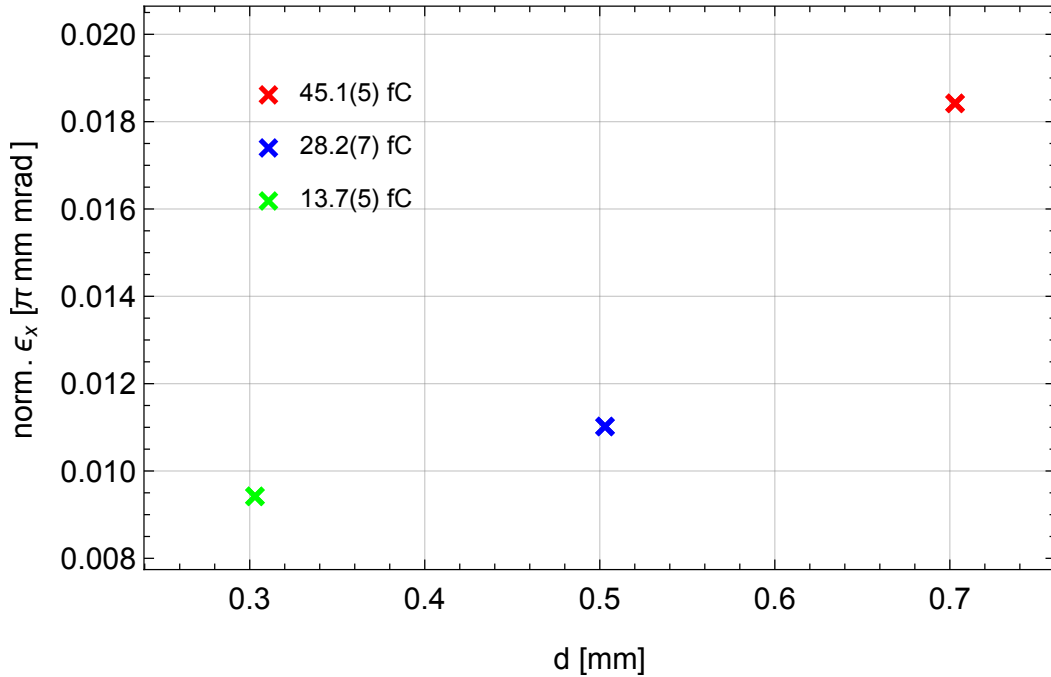


Figure 5.3: The normalized transverse emittance in dependence on the collimator diameter d . The different bunch charges are labeled in the plot legend.

5.2 Comparison of ASTRA simulations and an emittance measurement

The comparison of an emittance measurement at REGAE and an ASTRA simulation offers the opportunity to verify the results of the measurement. If the results of the measurement as well as the simulation coincide, the measurement as well as the simulation itself are confirmed. Although ASTRA is a widely used and confirmed tracking code not each and every beam optical device at REGAE necessarily has to be modeled correctly in ASTRA. Therefore the comparison of the measurement and the simulation can verify the REGAE model of ASTRA as well.

But to integrate the REGAE machine parameters into ASTRA it is necessary to do some preparations. The conversion of the electrical currents of the solenoids into the maximum longitudinal magnetic field $B_{z,\text{max}}$ has to be done as well as the correct gradients and phases of the cavities have to be determined. Because this measurement has been performed during a period a cesium-telluride cathode

was installed the collimators at DDC1 have been used. Hence the original charge generated at the cathode is unknown an ASTRA scan is required to determine it. A similar problem occurs for the measured mean beam energy which cannot be directly used because the dipole spectrometer is placed after the buncher cavity. So that both cavities can contribute to the mean beam energy of the electron bunch. If the machine is set up ideally, the buncher does not contribute, meaning it is not accelerating or decelerating, the electron beam is injected at the bunching phase which is exactly the zero crossing of the accelerating field. But this cannot be guaranteed and has to be checked.

The emittance reached in this scan is common for REGAE during the period of this thesis. A normalized emittance of $24.8(3) \pi \mu\text{m mrad}$ and $23.5(3) \pi \mu\text{m mrad}$ for the transverse directions has been measured, respectively. The details of the measurement will be presented in the last subsection as well as the comparison with the ASTRA simulation. The correct machine setup is topic of the first subsection. The second subsection is dedicated to the beam transfer to solenoid Sol67 which has been used for the emittance measurement.

5.2.1 Machine setup

To determine the correct RF parameters of the gun and the buncher calibration measurements have to be performed. The gun phase can be determined independently from the other parameters. A charge-phase scan has been performed, meaning a scan of the accelerated charge depending on the gun phase. The onset phase, meaning charge gets accelerated, is well correlated to the phase of maximum energy gain. The dependency of the output energy of the gun on the phase is plotted in Fig. 5.4, right. The specific phase has to be adjusted for each gun gradient but is not highly sensitive. A small misadjustment of the phase varies the output mean beam energy of the gun just slightly but is still a source of error. The phase of rising charge from the charge-phase scan and the rising left edge in the right plot of Fig. 5.4 are equivalent. This indirect adjustment of the maximum energy phase of the gun is necessary because the energy of the gun can not directly be measured due to the coupled cavities at REGAE.

The measured mean beam energy of the electron beam at the dipole spectrometer is the consequence of the various contributions of the gun and buncher. First of all the relation between cavities' gradient and the energy gain has to be determined. E.g. the gun gradient is well correlated to the energy gain. They are linearly

correlated according to the left plot of Fig. 5.4 for gradients above 30 MV/m and assuming the phase of maximum energy gain. A similar correlation can be found for the buncher gradient. After adjusting the gun phase the gradients of both cavities and in principle the buncher phase can be calibrated with an energy-buncher phase scan at the dipole spectrometer. Measuring the mean beam energy depending on the arbitrary buncher phase yields calibrations for the gun and buncher gradient as well as the buncher phase. The procedure is the following: If the gun phase and gradient is kept constant during the scan and the buncher gradient is normalized for the scan - due to the functionality of the phase shifters the buncher gradient cannot be kept constant while changing the buncher phase - a sinusoidal dependency of the mean beam energy and buncher phase can be measured. Fitting the measured data with a simple sinusoidal model yields the wanted calibrations. This calibration is valid as long as the RF system and all connected subsystems have not been changed and can be applied to the read-back gradients of the cavities. In Tab. 5.2 the corrected gradients are listed.

Because the time of flight of the electrons between gun and buncher changes the

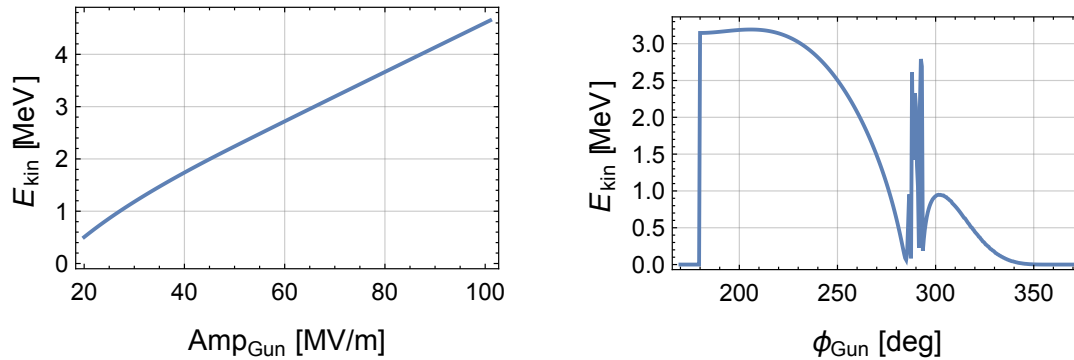


Figure 5.4: **Left:** Shown is the mean beam energy E_{kin} depending on the gun gradient Amp_{Gun} . Above 30 MV/m the dependency is in good approximation linear. **Right:** The output mean beam energy E_{kin} depending on the gun phase ϕ_{Gun} . The phase of maximum energy gain depends on the gradient. Here, the gun gradient is 70 MV/m and a maximum mean beam energy of 3.19 MeV can be achieved.

absolute buncher phase strongly, the buncher phase is strongly influenced by the gun RF parameters. A different gun setting makes a new buncher phase calibration necessary. Therefore it is more sufficient to determine the buncher phase by means

of the mean beam energy. An ASTRA scan of the energy gain of the buncher depending on the buncher phase can be used to correct the measured buncher phase. Using the calibrated gun phase and gradient yields the contribution of the gun to the mean beam energy. The difference is caused by the buncher. Assuming that the buncher gradient is well calibrated the buncher phase has to be adjusted in a way that the measured mean beam energy is reached. The phase of the buncher is normally adjusted close to the bunching, meaning zero-crossing, phase. In ASTRA this phase corresponds to -90° . A scan taking all measured and calibrated RF parameters into account has been performed with ASTRA. The scan (Fig. 5.5) yields for this measurement a phase of -104.7° which is pretty far off the aimed bunching phase. Unfortunately an experimental and more reliable determination of the bunching phase was not available and therefore the phase has not been corrected for this measurement and is taken for the ASTRA simulation.

Because the charge has been drastically cut to a much smaller amount by the collimators the measured bunch charge and the geometry of the collimators can be used to determine the 'real' charge at the cathode. An estimation of the laser spot size has been done just shortly before the considered emittance measurement. The laser spot size is directly introduced to ASTRA and a scan of the emitted charge at the cathode has been performed. The gun has been set up in ASTRA with the determined phase and gradient from above. Furthermore the collimator has been introduced to the simulation as an aperture with the used collimator diameter of 1.1 mm at position of DDC1. The bunch charge after the collimator depends on the generated charge at the cathode (see Fig. 5.6). The scan yields a generated charge of 37.6 pC.

The last machine parameters which has to be converted are the electrical currents of the solenoids. For the conversion the introduced calibrations of the single as well as the double solenoids from Sec. 2.1.2 can be used. The results are listed in Tab. 5.2 as well. All obtained results can now be introduced to a full start-to-end ASTRA simulation which will be presented in the following.

Table 5.2: Machine and ASTRA setup for the presented emittance measurement. Listed are the required machine devices to set up a ASTRA simulation. Beside the solenoid settings the measured cavity amplitudes (Gun and Bun), charge (DaMon) and energy are depicted. The energy has been determined by use of the dipole spectrometer. Therefore the energy has been yielded after passing both cavities. The contribution of each cavity depends on the adjusted phases. For the solenoids it is necessary to convert the currents to the maximum longitudinal magnetic field $B_{z,\max}$. Due to the usage of the first collimator *Coll1* the bunch charge measured at *DaMon* is not the charge at the cathode which is required for the ASTRA simulation. Hence, scans for the buncher phase as well as charge at position of the cathode needs to be done and are presented in Fig. 5.5 and Fig. 5.6. The laser beam parameters ($x_{\text{RMS},l}$, $y_{\text{RMS},l}$ and $t_{\text{RMS},l}$) had been measured recently and can be directly put into the ASTRA simulation.

Device	Set value machine	Set value ASTRA
Sol1	1.00 A	21.7 mT
Sol23	4.19 A	88.9 mT
Sol45	off	0.0 mT
Sol67	0.3 A to 2.7 A	6.8 mT to 57.4 mT
Coll1 [mm]	1.1	1.1
$x_{\text{RMS},l}$ [mm]	0.314	0.314
$y_{\text{RMS},l}$ [mm]	0.255	0.255
$t_{\text{RMS},l}$ [ps]	0.5	0.5
Gun Ampl [MV/m]	60.30(3)	60.30
Bun Ampl [MV/m]	11.60(1)	11.60
DaMon [pC]	0.0376(6)	0.0376
E_{kin} [MeV]	2.45	2.45

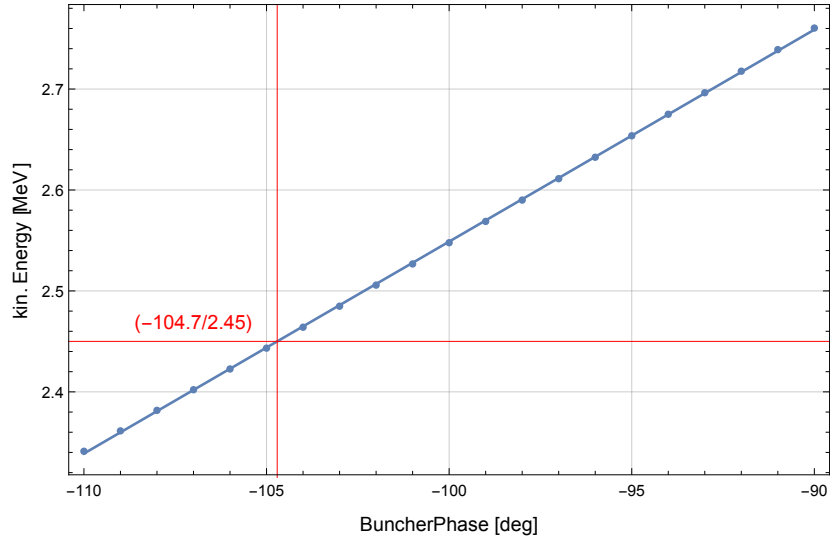


Figure 5.5: Buncher phase scan to determine the correct phase and to gain the measured average kin. energy of $E_{\text{kin}} = 2.45$ MeV. The red cross marks the right phase.

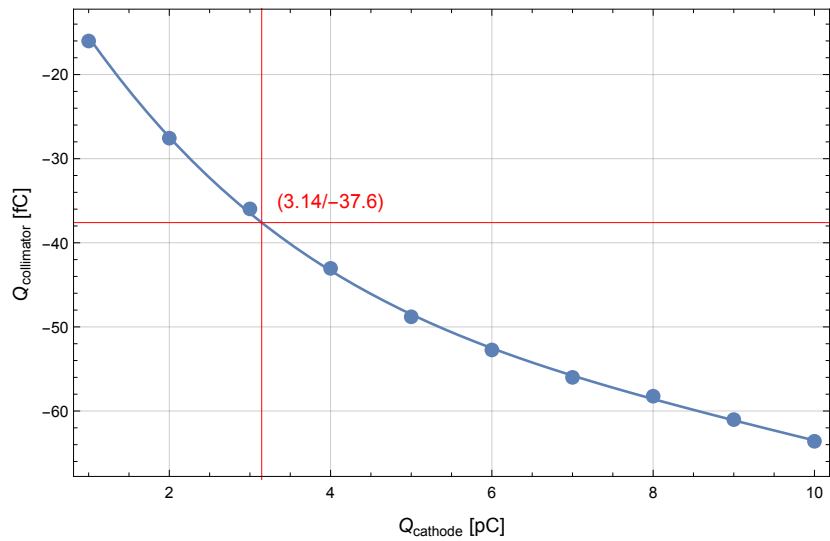


Figure 5.6: Remaining charge $Q_{\text{collimator}}$ after the collimator ($d_{\text{Coll}} = 1.1$ mm) depending on laser intensity or respectively the generated charge Q_{cathode} at position of the cathode. The red cross marks the right charge at the cathode. This value is needed for the ASTRA simulation. The negative sign of $Q_{\text{collimator}}$ is caused by the species (electrons) which has been used for the ASTRA simulation and is not relevant.

5.2.2 Beam transport

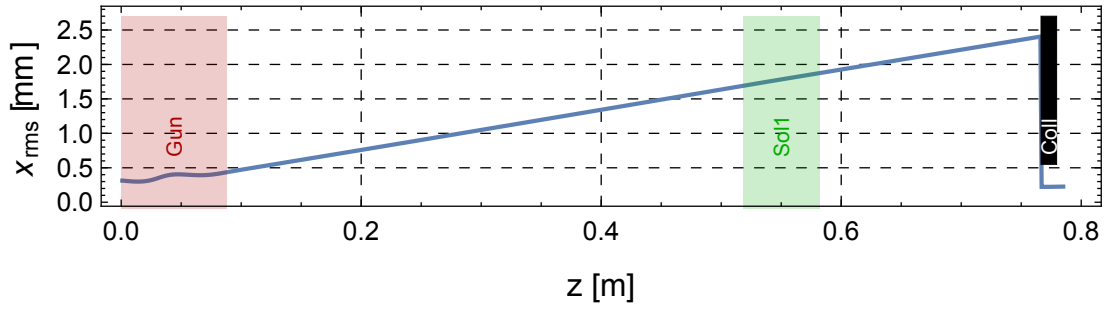
The tracking of the electron beam from the photo cathode to the detector screen is divided into three sections. The first two describe the transport from the cathode to the solenoid used for the magnet scan. The magnet scan is discussed in the last subsection.

Starting with the transport of the electron bunch from the cathode through the collimator. In Fig. 5.7 the beam envelope as well as the transverse emittance and the bunch length are depicted. The relevant beam optics and apertures are illustrated as colored blocks in the line plots. The influence of solenoid Sol1 direct in front of the collimator is almost negligible. Due to the collimator the beam size decreases almost by an order of magnitude and so the emittance. In contrast the bunch length seems to increase due to the collimator. But this is just a statistical effect. The collimator is cutting off electrons at the transverse periphery of the bunch but these electrons are located closer to the longitudinal center of the bunch. The elongation of the bunch is therefore just caused by the statistical calculation. Direct behind the collimator the measured bunch charge is reached. Downstream of the beam line there are no further apertures which could cause a charge loss. Furthermore the emittance has been almost reached its final value as well. The horizontal emittance which will be used for comparison with the simulated, is $24.8 \pi \mu\text{m mrad}$.

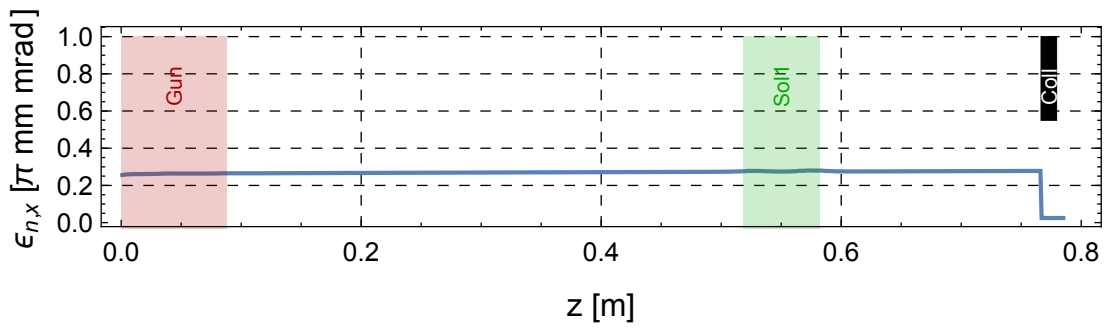
The beam transport from the collimator to solenoid Sol67 is pretty much straight forward (Fig. 5.9). Because of the wrong phase of the buncher and more important because of the small gradient of the buncher the electron bunch is longitudinally not bunched at all.

Normally, the buncher imprints a negative longitudinal energy correlation [13]. Electrons at the head of the bunch are decelerated and electrons in the tail are accelerated. The longitudinal energy correlation causes a velocity difference of the head and tail of the bunch. During the following drift the electron bunch gets compressed. Because an energy correlation is imprinted this scheme only works for low relativistic electrons. For high relativistic electrons the energy correlation is just weakly transformed into a velocity difference and the bunch does not get compressed. The energy correlation of the incoming electron bunch is positive - the reason why the bunch gets longer in front of the buncher. If the applied field gradient inside the buncher is too low the bunch elongation is just reduced but not reverted. Due to the high charge at the cathode a space charge induced

a)



b)



c)

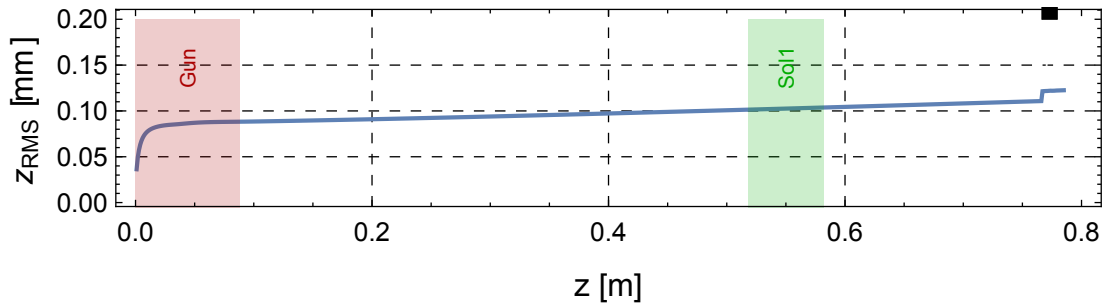


Figure 5.7: Tracking from the cesium-telluride through the collimator ($d = 1.1$ mm): **a)** RMS beam size, **b)** norm. RMS emittance, **c)** RMS bunch length. The horizontal direction is plotted representatively. The various beam optics relevant elements are indicated by colored blocks. Cavities are *red*, solenoids are *green* and collimators are *black*. Their width is correctly scaled to the real objects dimension.

larger positive energy correlation is generated already in the gun and the buncher gradient has been too low to compensate it. That can be observed in this particular simulation. The bunch length growth is consequently just reduced. But due to the former determined buncher phase and gradient the measured mean beam energy is correctly adjusted and illustrated in Fig. 5.8.

Going back to Fig. 5.9 it can be observed that the emittance stays constant along

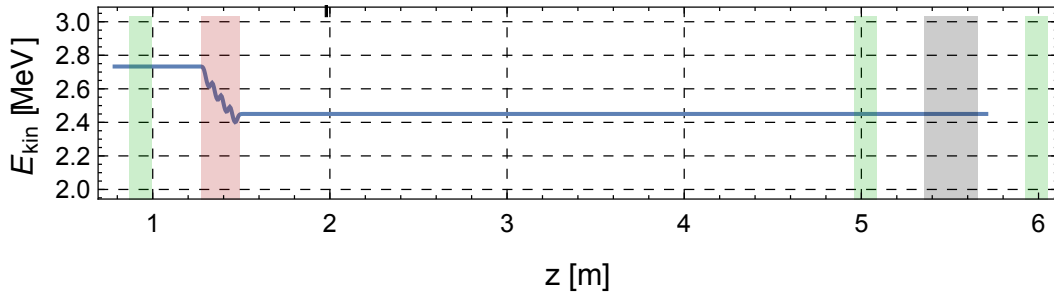


Figure 5.8: Tracking the kinetic energy E_{kin} from the collimator to solenoid Sol67. The various beam optics relevant elements are indicated by colored blocks. Cavities are *red*, solenoids are *green* and collimators are *black*. Their width is correctly scaled to the real objects.

the beamline up to solenoid Sol67. Only inside solenoid Sol23 and the buncher cavity small changes are visible which are just a numerical fluctuations and can be ignored.

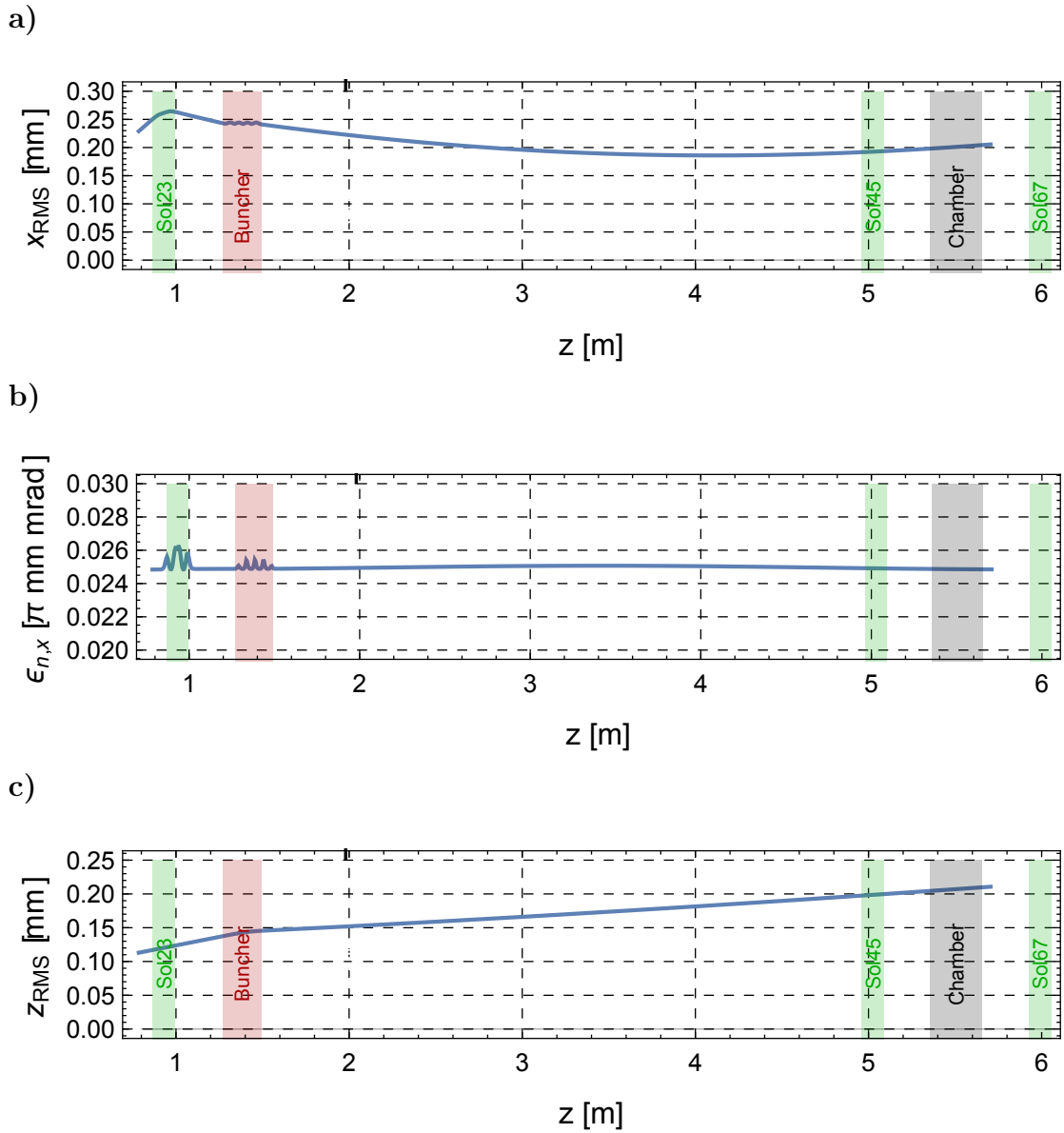


Figure 5.9: Tracking from the collimator to solenoid Sol67: **a)** RMS beam size, **b)** norm. RMS emittance, **c)** RMS bunch length. The horizontal direction is plotted representatively. The various beam optics relevant elements are indicated by colored blocks. Cavities are *red*, solenoids are *green* and collimators are *black*. Their width is correctly scaled to the real objects.

5.2.3 Magnet scan

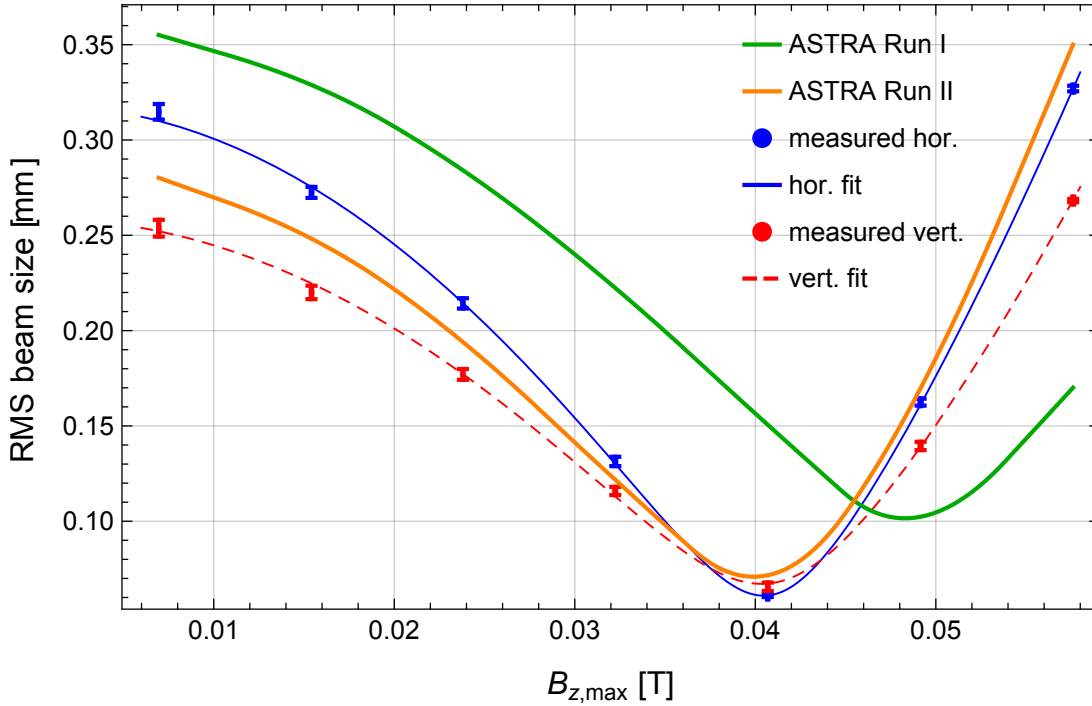


Figure 5.10: Emittance scan at D1 detector with solenoid Sol67. Comparison between simulations (green/orange line) and measurement (red and blue dots). In addition the fitted model is plotted (solid/dashed lines).

Solenoid Sol67 has been used to perform the scan and detector D1 to record the transverse beam profiles. The scan is shown in Fig. 5.10 (blue and red dots). Besides the measured beam size depending on the magnetic field of the solenoid, the results of the fitted model are illustrated by the solid/dashed blue/red lines. The results of the fits are listed in Tab. 5.3. In order to compare the measurement with the simulation the simulated **ASTRA** electron beam of the previous described beam transport from the gun to solenoid Sol67 has been taken to simulate a magnet scan - as well in **ASTRA**. The RMS beam sizes obtained by introducing the magnetic field strength setting of Sol67 to the simulation have been plotted as well in Fig. 5.10 (green line, **ASTRA Run I**) and the initial beam parameters have been extracted from the simulation in order to compare them to the measurement. The

trend of the simulation and the measurement are comparable but not matching well enough to neglect the discrepancy which can easily occur due to uncertainties in the machine setup in ASTRA.

The measured and the simulated normalized emittance are coincide within the

Table 5.3: Comparison of the achieved simulated beam parameters on the one side and the determined parameters from the measurement on the other side. The normalized emittance of the ASTRA simulation corresponds to the depicted average emittance in Fig. 5.12, left. Respectively the horizontal as well as vertical results measured at REGAE are presented.

Parameter	ASTRA Run I	REAGE measurement
Q [fC]	37.1	37.6(6)
E_{kin} [MeV]	2.45	2.45
$x_{0,\text{RMS}}$ [μm]	209	262.0(5)/212.0(7)
$(x_{0,\text{RMS}})'$ [μrad]	22.6	17.4(1)/12.7(1)
$\epsilon_{\text{n,x}}$ [$\pi \mu\text{m mrad}$]	25.2(3)	24.8(3)/23.5(3)
$\tilde{\chi}^2$	-	1/1.5

error estimation of the measurement. As well as the remaining parameters match quite good. This indicates that the observable difference between the simulation and measurement are just a matter of the initial beam parameters at the entrance of Sol67. To estimate the discrepancy of the measured and simulated initial beam parameters - namely $x_{0,\text{RMS}}$ and $(x_{0,\text{RMS}})'$ - another ASTRA run has been performed with a modified initial particle distribution which matches with the measured beam sizes at D1. Unfortunately the fitted initial beam parameters from the measurement - introduced to ASTRA - do not fully reconstruct the measurement. Therefore a first conclusion is that the simplified analytical model (Eq. 2.22) is probably sufficient but does not fully describe the beam dynamics for this case. Especially the thin lens approximation (Eq. 2.20) is probably insufficient for a ~ 2.5 MeV electron beam. Further variations of the initial beam parameters yield that a comparably small change of the initial envelope slope $(x_{0,\text{RMS}})'$ reproduces the measured scan. The initial beam size $x_{0,\text{RMS}}$ is comparable to the measured. A different variation of the initial beam parameters can potentially reconstruct the measurement as well

but this simple variation illustrates already the small deviations between measurement and simulation.

The modification has been implemented in the following way: the originally simulated distribution has been stretched to yield the same RMS beam size. The envelope slope of the distribution has then been optimized in order to achieve the best agreement with the measured scan. The original and modified particle distributions are shown in Fig. 5.11, the comparison of the beam parameters between the measurement and the second ASTRA simulation are listed in Tab. 5.4. The normalized emittance as well as the initial beam size are almost identical only the initial envelope slopes are differ a bit. The difference of $\sim 25 \mu\text{rad}$ are explainable by the uncertainties of the RF parameters which are given by the difficulties of the calibration at REGAE (Sec. 5.2.1). Small discrepancies between the simulated and real RF parameters of the two cavities can lead to strong variations of the beam parameters (x_{RMS} and $(x_{\text{RMS}})'$) at the position of Sol67. The emittance should not be influenced by the uncertainties of the RF parameters which is indeed the case in the presented measurement.

Another interesting question is: Does the emittance is conserved during the scan

Table 5.4: Comparison of the modified ASTRA beam parameters on the one side and the measured parameters from REGAE on the other side. In contrast to Tab. 5.3 the initial distribution (Fig. 5.11, green) has been modified (orange) to reproduce the measured results (Fig. 5.10).

Parameter	ASTRA Run II	REAGE measurement
Q [fC]	37.1	37.6(6)
E_{kin} [MeV]	2.45	2.45
$\mathbf{x}_{0,\text{RMS}}$ [μm]	263	262.0(5)/212.0(7)
$(\mathbf{x}_{0,\text{RMS}})'$	-10.0	17.4(1)/12.7(1)
$\epsilon_{\mathbf{n},\mathbf{x}}$ [$\pi \mu\text{m mrad}$]	25.5(7)	24.8(3)/23.5(3)
$\tilde{\chi}^2$	-	1/1.5

and is the simple analytical model sufficient? The dependency of the emittance on the solenoid setting during the scan is depicted in Fig. 5.12, left. The emittance decreases consequently and reaches its minimum at the minimal beam size. The non-linearities imprinted into the phase space by the beam optics - the solenoids

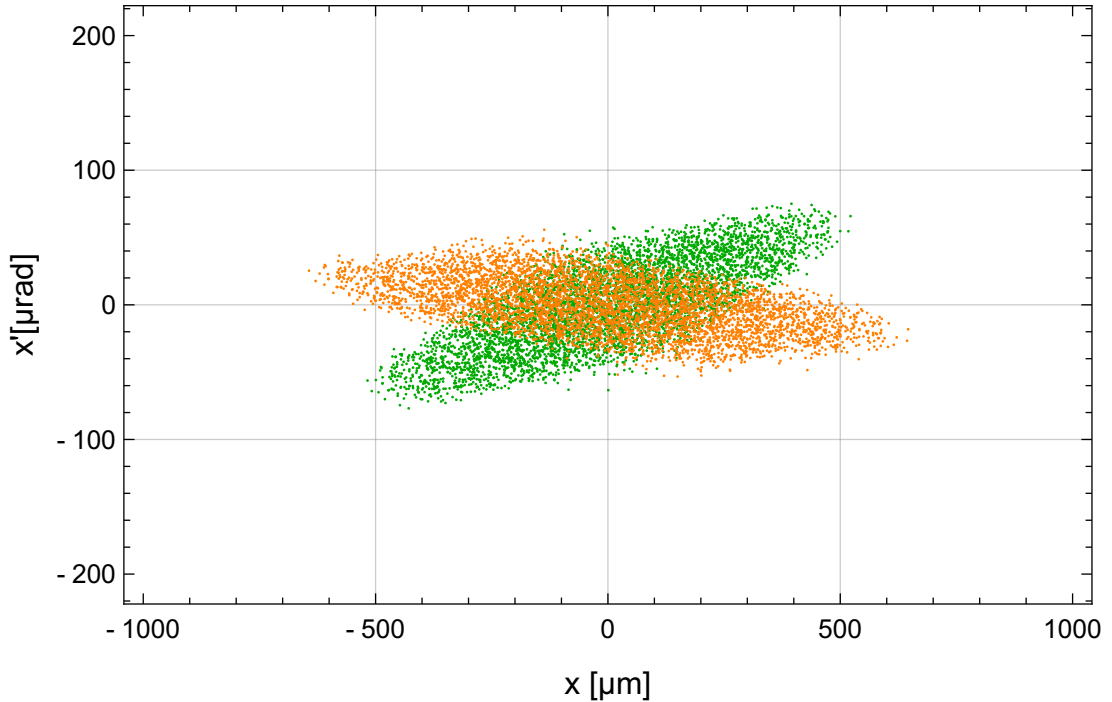


Figure 5.11: Initial phase space distribution of simulated electron bunch at position of Sol67 (green distribution). The distribution is extracted from a start-to-end ASTRA simulation. It corresponds to the emittance scan, labeled **ASTRA Run I**, showed in Fig. 5.10. The second, overlaid distribution (orange) is a modified version of the green distribution. It is modified in a way that the best agreement with the measurement has been achieved. In Fig. 5.10 it is called **ASTRA Run II**.

have a linear field just in first approximation - are partly compensated by the solenoid used for the scan. This non-linearity can be noticed as a curvature of the phase space which increases the RMS emittance. It is exemplarily illustrated in Fig. 5.12, right. Two phase space distributions of the simulated solenoid scan are depicted (smallest and largest emittance). The correlation of position and divergence $\langle xx' \rangle$ has been subtracted and each direction (x and x') of the phase space has been normalized to the corresponding RMS value. The distribution with the smaller emittance ('yellow' distribution) occupies a smaller area and it does not show additional 'features' compared to the 'blue' distribution. The correct

solenoidal field can compensate the phase space curvature and reduce the emittance. But the variation of the emittance during the scan is small and the mean has been taken for comparison with the measurement.

The accordance of the simulation and the measurement is excellent considering

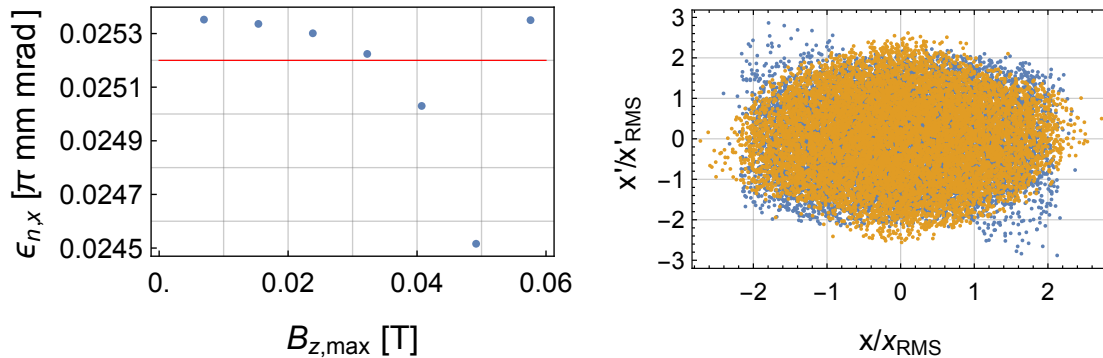


Figure 5.12: Left: Normalized horizontal emittance depending on the different solenoid settings of Sol67. The red line marks the average normalized emittance of $25.2(3) \pi \mu\text{m mrad}$. **Right:** Compares the uncorrelated and normalized phase space of the electron distribution at the minimal beam size (yellow dots) and the last data point (blue dots) of the scan. The correlation $\langle xx' \rangle$ of the horizontal position x and the horizontal divergence x' has been subtracted. Furthermore the distributions has been normalized in both directions of the phase space to their corresponding RMS values. Corresponding to the emittance difference shown in the left plot, the occupied area of the 'blue' distribution is larger. Moreover the 'blue' distribution has a distinct curvature noticeable by the additional 'wings' which illustrates the non-linearities imprinted on the distribution. The 'yellow' distribution does not have these features.

the different assumptions and afterwards considerations which had to be made to determine the correct machine parameters for the simulation. The whole comparison of measurement and simulation relies on the valid model of the REGAE linac in ASTRA. This includes the correct calibration of the magnetic fields of the solenoids, the calibration of the cavity gradients and phases, a correct energy measurement and a correct charge measurement which has been used to set up the correct conditions inside the gun. The small differences between measurement

and simulation regarding the magnet scan can be explained by the sum of all these small deviations of the model from the real machine as well as the simple beam transfer model used for the magnet scan. Especially the phases and gradients of the cavities can cause easily changes in the transverse beam optics which result in the observed deviations. The overall agreement of the measurement and the simulation are fantastic and they prove the validity of the measurement on the one side and the ASTRA model of REGAE on the other side.

5.3 Long-term observations

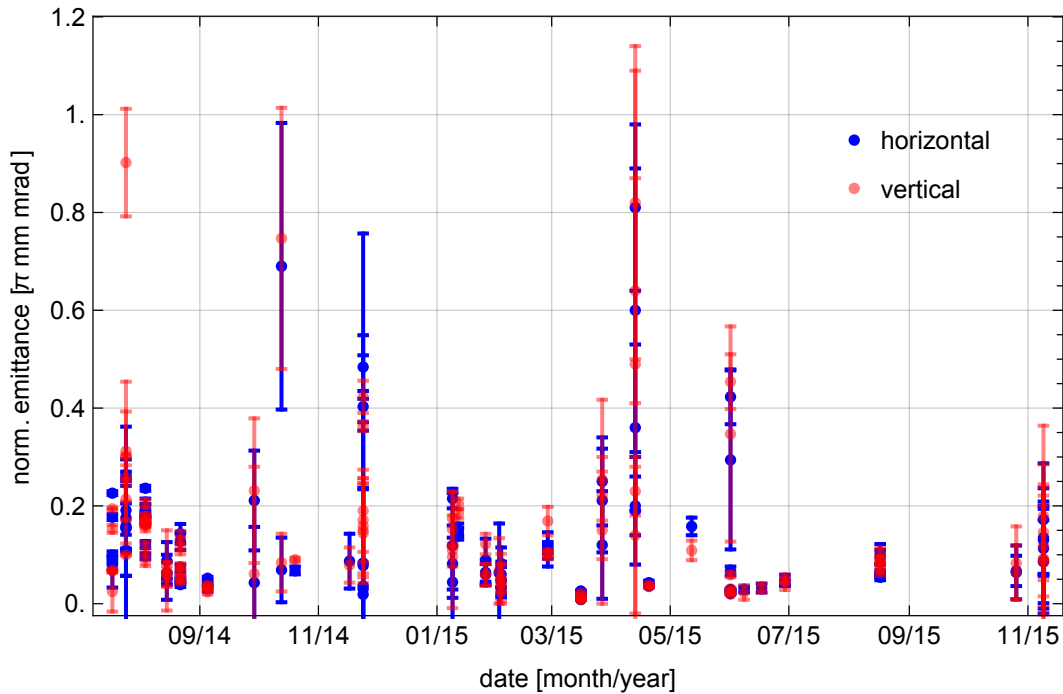


Figure 5.13: Long-term emittance measurements at REGAE over a period of 14 months.

During the course of this work emittance measurements have been constantly performed. In this section the results of a period from August of 2014 to October of 2015 are presented (Fig. 5.13). This period can be divided in two sections. In January of 2015 a cesium-telluride cathode has been inserted in the gun. Before a molybdenum cathode was installed. In principle it is possible to compare the different setups of the machine but unfortunately there are not any big difference

between these two periods. With the collimator setup indeed the smallest emittance could be measured. A principle trend to smaller emittances is however not observable. Successful and trustworthy measurements have always relied on a stable machine. The dark current level varies due to the application of the collimators between both setups but it could be shown that the dark current is a fundamentally manageable disturbance (Sec. 3.2). It surely effects emittance measurements at very low bunch charges. Therefore measurements down to ~ 10 fC could only be performed for conditions with a very low dark current contribution. Because the quantum efficiencies of the used cathode varies quite strong the electron density right at the cathode varies strongly. As a consequent a larger portion of the dark current can be blocked by the collimators and still a reasonable amount of bunch charge can be transported if the cesium-telluride cathode is inserted. But measurements down to a few femtocoulomb are only interesting from a beam dynamical and technical point of view. It is outstanding that a measurement at such a low bunch charge is possible and delivered reasonable results but there is no experimental use for, so to say, 'ultra-ultra' low-charged bunches at REGAE. Every experiment relies on a good signal-to-noise ratio - the diffraction experiments as well as the planed plasma wakefield experiments. Therefore a high beam quality has to be achieved at higher bunch charges.

In this context it is worth to sort the emittance measurement results by their mean beam energy and bunch charge. These are the most direct quantities to influence, or more preciously, to maintain the beam quality. A low bunch charge as well as a high mean beam energy reduce the space charge effects and reduce the emittance growth. Fig. 5.14 tries to illustrate the correlation of the transverse beam emittance depending on the kinetic energy and the bunch charge. Nevertheless the largest influence is still given by the laser pulse parameters at the cathode. And because the laser parameters are not the same for all measurements a clear correlation between the three quantities (emittance, energy, charge) could not be demonstrated. Furthermore the charge not only indicates the reduction of the bunch charge right at the cathode but instead it can be obtained by a charge cut due to the collimators. But this is equivalent to a reduction of the phase space volume as well.

The chosen measurements have been selected by their credibility, meaning measurements with a good fitness value $\tilde{\chi}^2$ have been taken. Only a trend for the charge dependency is observable which can be explained by the former mentioned

5 Transverse Emittance Measurements and Simulations of a low charge electron bunch at REGAE

use of collimators. A real correlation with the kinetic energy is not noticeable. As already mentioned a repaired gun was in operation at REGAE during the period of these measurements. The field gradient was limited because a huge amount of dark current could be observed at higher gradients (> 60 MV/m) and the whole RF system gets unstable. Measurements at higher gun gradients always yielded flawed results.

An always accompanying problem has been the unknown laser parameters at the

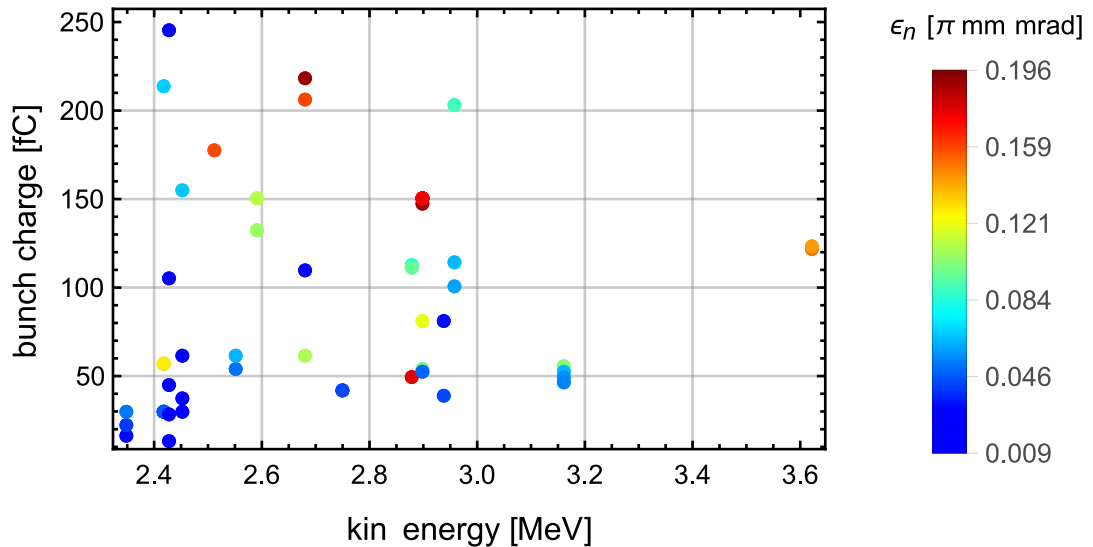


Figure 5.14: Emittance measurements at REGAE illustrated in dependence on the kinetic energy and the bunch charge. The emittance is indicated by a color code.

photo cathode as well as the reliability of the laser. The laser spot size could not be measured reliably during the operation. The procedure was time consuming and hence, not often performed. Furthermore the design parameters of a $7 \mu\text{m}$ spot size has never been reached and it is questionable if it is possible due to the given geometry. The distance between the focusing lens and the photo cathode is too long. The adjustment of the pulse length occurs as a similar problem. The laser system is constructed to produce short laser pulses in the range of 100 fs or even less. But for the ballistic bunching scheme at REGAE (Sec. 1.1) a pulse of 500 fs is preferred because a consequently longer electron bunch can be longitudinally focused tighter.

Nevertheless, it could be shown that a small transverse emittance can be achieved at REGAE even at a comparably low mean beam energy. The detector system D1 (Sec. 3.1) has demonstrated its reliability and its high charge sensitivity. Furthermore the introduced post-processing routine (Sec. 3.2) could be integrated in daily operation and yielded reliable and reasonable results for the emittance determination. If the design energy of 5 MeV is established in a stable operation, a higher charge can be accelerated without loss of beam quality due to the reduced space charge effects. The experiments at REGAE would benefit from this development.

6

Conclusion and Outlook

The main topic of this work to develop a high precision emittance measurement as a preparation of the plasma wakefield injection experiment has been achieved. Starting with a commonly used method to determine the emittance several issues, resulting from the existing conditions at the REGAE linac, had to be overcome to reach the goal. Challenging technical difficulties - especially due to the ultra low bunch charge down to a few fC - have arisen. Its generation and transport to the target and the detector is not a fundamental problem or challenge, but a precise detection is definitely challenging.

Consequently the first section of Chap. 3 is dedicated to this issue. REGAE's detector system, used for the emittance measurements, has been presented and discussed in detail. The combination of a high light yield and a still reasonable spatial resolution has been realized by a Fiber Optic Scintillator (FOS) and a high charge-sensitive EMCCD camera. This detector could give proof of its potential in context of various applications. The capability of the detector could be verified by a detector efficiency measurement which means a determination of the conversion and collection efficiency of the detector from the moment the electrons hitting the scintillator until an image is recorded with the camera. This includes the scintillation process as well as the light optics towards the camera and the conversion efficiency of the camera itself. The found detector efficiency is in well coincidence with the theoretically approximated efficiency of the detector system. In principle the results of this measurements can be used for a charge calibration which would

consider the camera gain as well. All in all the detector meets all technical demands required to successfully perform high precise transverse beam studies. Besides the technical challenges a precise determination of the emittance has been of particular interest. The selected measurement method bases on an analytical description of the beam size development depending on the beam optics and initial beam parameters. The beam size, as a projection of the unknown phase space volume occupied by the electrons, is measured for different states of the phase space distribution. The change or transformation of the phase space is induced by the beam optics in case of REGAE this means the magnetic field of a solenoid has been successively scanned. By means of a least-square fit it is possible to draw conclusions about the phase space volume, the emittance. Essential for this method is obviously the determination of the beam size and a detailed knowledge of the beam optics. The beam optics, here the electrical solenoids at REGAE, are well known and tested. In contrast the determination of the beam size is more difficult. From a theoretical point of view the wanted beam size is a RMS quantities of the electron distribution, but often for reasons of manageability and simplicity a normal distributed electron bunch is assumed and consequently fitted. The direct calculation of the RMS quantity has a big practical disadvantage towards a simple fit method. The contribution of the noise to the RMS beam size can be enormous. With a fit these contributions are manageable or could be ignored principally. Therefore a big success of this work is a physically and mathematically profound routine to determine the RMS beam size. The routine demonstrated its robust and reliable nature in daily operation at REGAE and furthermore the fundamental description of the noise which belongs to each and every image offers the opportunity to automatically define profound intensity cuts. A further reflection of the induced errors of this method helped to understand the mechanisms of this approach on the one side and helped to find adequate cut values on the other side.

An obstacle of this studies were the discovery of a really distinct beam halo which occurs on every single image taken with the detector system D1. For a long period it has been treated as a beam feature. The other beam monitors do not have the same sensitivity as the D1 detector. Therefore it was not possible to cross-check the observation of a distinct but still low-intense beam halo with another beam monitor. Because the beam emittance was consequently much larger than expected, investigations could show that the halo is not a real beam feature but instead an artifact of the detector system. First measurements tackling this issue

could not clarify the origin of the halo. Beam based measurements at REGAE indicates clearly that the halo could not be a part of the electron beam which leads to investigations regarding the detector system itself. Setting up the D1 setup in the laboratory and performing measurements with different β^- -emitter yielded again not a conclusive result. The sources were too weak or the energy spectrum was too broad to make a clear statement. Finally particle shower simulations with EGS5 of the installed FOS support an explanation of the origin of the halo. Due to the special composition of the FOS used at REAGE's detector system electrons are back scattered from the Fiber Optic Plate (FOP) where the actual scintillator is grown on. The back scattered electrons produce scintillation light which overlaps with the original signal of the 'real' beam. The back scattered electrons are detected as the distinct halo. The simulations could be compared to measurements from D1 and showed a good agreement even if the measured halo intensity is higher than the simulated. The assumed scintillator and FOP model are simplified but still the principal mechanism of the halo generation could be demonstrated. Therefore it is well reasoned to treat the beam halo as an artifact and cut it off.

The artifact generated by the screen can be handled in respect of the emittance measurements and for any other applications like the diffraction experiments the halo is not an issue. The specific beam sizes are not of particular interest for these kind of experiments. Nevertheless the scintillator introduces an uncertainty which is predicable but could be avoided as well. Right now we are aware of the problem and deals with it.

The characterization of the detector system as well as the profound determination of the RMS beam size could then be used to perform highly accurate emittance measurements. The presented results of Chap. 5 could verify the emittance to be as low as expected from the REGAE design studies. The measurements have small errors and the least-square fit possess a high likeliness. For lower charges down to 10 fC a transverse emittance of just $9.0(2) \pi \mu\text{m mrad}$ could be measured. 10 fC is at the lower resolution limit of the charge diagnostic at REGAE but even these ultra low bunch charges could not only be detected with the introduced detector system, a magnet scan could be performed, the RMS beam size precisely determined and the emittance obtained from the least-square fit is reasonable. The measurement routine not only proved its quality, furthermore it was possible to match a measurement with an ASTRA simulation. It could be demonstrated that ASTRA simulations model REGAE well and that they can reproduce the REGAE machine

setup with the correct beam parameters. Concerning the circumstances of this matching it is a big success. In parallel a 'live' diagnostic tool has been developed. It will take all machine parameters into consideration and simulates by means of ASTRA the current beam parameters along the whole beamline. Furthermore it should help to simplify the adjustment of the on-crest gun phase depending on the current gun gradient. Especially the correct implementation of the RF parameters into ASTRA is tricky but first tests showed a great agreement between the measured mean beam energy and the simulated one for arbitrary RF parameters. The next step is the matching of the transverse beam dynamics of the simulation with real measurements.

In order to improve the transverse beam quality a setup with a cesium-telluride cathode (high quantum efficiency) and a strong beam collimation has been setup for almost one year of operation. The transverse emittance has been measured regularly and compared to the standard REGAE setup. Indeed it was possible to measure the smallest transverse emittance but a large enhancement of the beam quality could not be observed. Due to the high quantum efficiency of the cathode a huge amount of charge - by REGAE standards - could be generated and accelerated. The collimator right behind the gun cuts off the majority of the charge. Only the really inner core of the bunch 'survives'. Bunch charges of several 10 pC are collimated to 10 fC to 200 fC. Therefore the exact cathode laser parameters are not so important and just slightly influence the final beam quality. The transverse beam quality seems to benefit from this machine setup slightly. But this machine setup confines the shortest possible bunch length. Due to the huge space charge effects right at the cathode the longitudinal emittance gets worse and consequently the longitudinal focus is not as tight as for the standard machine setup. But most experiments not necessarily need the shortest possible bunch and could still gain benefits from this setup in terms of the transverse beam quality.

Summarizing the emittance measurements and studies very good results could be achieved and the huge potential of the machine could be demonstrated. There are some more studies which can be conducted with the standard REGAE setup to improve the emittance. An important study would be a scan of the cathode laser spot size at the cathode. There is an optimal spot size which yields the smallest emittance. It depends on the charge density at the cathode which is determined by the laser intensity and the cathode material. A higher density causes stronger

space charge effects which counteract the principle emittance reduction due to a smaller laser spot size. Therefore, a subsequently scan of the emittance in dependence on the laser spot size is required. For the realization a full control of the laser spot size at the cathode is required.

For a photo injector like REGAE the emittance is defined right from the beginning. A reduction of the emittance at a later time is difficult. Therefore the cathode laser performance is crucial. The laser pulse parameters has to be known in order to have the full control of the electron beam parameters. This had been always an issue at REGAE. Most of the time the laser acts like a 'black box'. This is one reason for the stagnated improvement of the electron beam quality. The cathode laser was not a 'highly' reliable device. But there are ongoing developments of the cathode laser. For example a motorized lens has been installed lately right in front of the incoupling of the laser into the RF gun. Still an issue is the control of the laser pulse duration. In addition to the obvious parameters there are predictions for different laser pulse shapes, transverse and longitudinal, and their influence to the emittance conservation in the presence of space charge effects.

The accelerator itself needs some improvements as well. In terms of stability the design stability of ~ 10 fs could never be reached. The most important reason is the cross-talking of the two cavities which are fed by one modulator and klystron. Any change of the RF parameters at one cavity causes a reaction of the second one. Therefore a stability down to ~ 10 fs seems unrealistic. But this problem will be solved by the installation of a second modulator. Gradients and phases can then be adjusted independently. Another upgrade is related to the transverse diagnostic. A second detector system D2 will be integrated in the REGAE beamline. It is placed directly behind D1. It has again a FOS which is much larger and a CMOS camera. Because the CMOS camera has no internal gain device a highly sensitive image intensifier will be integrated in the light optics which contains much larger lenses compared to D1. This will increase the detector efficiency. The D2 detector offers a good opportunity to cross-check the insight obtained from the D1 detector - especially, the beam halo could be verified.

But for now I would like to come back again to the emittance measurements. Due to the matching of an ASTRA simulation and an emittance measurement the magnet scan method is reasonable. But there have been already introduced and tested methods to determine the emittance at REGAE [17, 84]. Without going too

much into details I will shortly introduce both methods. On the one side it is possible to determine the emittance from diffraction experiments. From the diffraction pattern a 90° phase advance between the target and the detection screen can be adjusted. This information can be used to calculate the emittance from the beam sizes at the target and the detector. Another method is the determination of the emittance from shadow images of a mesh. From the magnification and the acuity of the shadow image it is possible to determine the emittance. Unfortunately, these methods have never been cross-checked with the magnet scan. It is necessary to know the beam size at the target which can be just poorly determined. The geometry of the installed diagnostic at the target chamber does not allow precise measurements. The scintillator is too far away from the light collecting optic. Another interesting method to determine the emittance could be a phase space tomography [85,86]. The measurement procedure is absolutely comparable with the magnet scan technique. The measured beam profiles at the detector can be seen as the projections of the phase space depending on the phase advance introduced by the magnet. The idea is to reconstruct the phase space from its projections using a sophisticated algorithm. The detailed phase space distribution would be available which could gain even deeper insight in the beam dynamics.

In reference to the upcoming plasma experiments an emittance measurement of the outgoing electron bunch will be required. There are two easily realizable setups. The first has been presented by C. M. S. Sears et al. in [87]. It is a modification of the pepper-pot method [88]. The electron beam has to pass a slit mask. The produced beamlets are transported onto a screen. From the beamlet size, the divergence and the slit mask geometry the transverse beam emittance can be determined. Because every single beamlet has a significantly smaller charge, space charge effects are reduced and do not falsify the result anymore. But due to the large beam divergence in case of a plasma wakefield accelerated bunch a special focus has to lie on the design of the pepper-pot mask. There are two main drawbacks of this method. On the one side there is a general issue: The pepper-pot does not consider the different shearing of the beam slices in the phase space induced by the wakefield phase. Therefore only the projected phase space area of all individual slices is measured. But a benefit is that this method can be used as a single shot measurement. On the other side there is an issue which could be a specific problem at REGAE. Due to the low bunch charges it is questionable whether there will be enough signal to determine the emittance. The other proposed method is an en-

ergy resolved magnet scan [89]. R. Weingartner et al. [90] performed a quadrupole doublet scan on a laser plasma accelerated electron beam which passes a dispersive element like a dipole magnet before it has been detected on a scintillator screen. Assuming the beam is deflected in the horizontal direction the vertical phase space can still be scanned via a magnet scan and the emittance can be determined with respect to the energy. Further assuming that the energy of each longitudinal beam slice correlates with the wakefield phase, the slice emittance is accessible by this method. The beam optics at the upgraded REGAE beamline (Fig. 1.4) will be similar to the presented beam optics in [90]. This method seems to be the most promising for the LPA experiments at REGAE.

Chap. 4 is already leading to future experiments namely the plasma injection experiment at REGAE. The introduced permanent magnetic solenoids (PMS) can be used to achieve the required beta function at the injection point into the plasma. The PMS had to be assembled from wedges and needed to be characterized before they are installed at REGAE. In this context a simple analytical model and sorting algorithm have been developed in cooperation with F. Mayet. The sorting algorithm used a field quality factor based on the 4D transverse emittance to find the optimal arrangement of the wedges to maintain the field and consequently the beam quality. The assembling routine including the field quality factor has been benchmarked and demonstrated thereby its potential. The analytical model has been used in the context of the assembling as well as for the comparison with the measured magnetic field. The field measurement has been challenging due to the small apertures of the PMS and the strong field curvature. To achieve the best results for the measurements a 3D Hall probe with a high sensitivity and a small active volume has been bought. By using a post-processing correction on the measured field an excellent agreement between the measured magnetic field and the predicted field from the simple analytical model has been accomplished. The assembling and characterization of the PMS have been a great success. The second half of Chap. 4 covers the feasibility of reaching the required beam parameters to match the REAGE electron beam into the plasma wakefield. There are already really detailed studies on this topic in [10, 25]. In this thesis only the feasibility of the PMS to cope the requirements of the external injection is presented. An analytical description of the external injection into a plasma wakefield in the linear regime has been used to determine the electron beam requirements

for the given REGAE plasma wakefield parameters. ASTRA simulations could be used to demonstrate the feasibility to reach the requirements at the injection point for a standard REGAE beam. The alignment procedure of the PMS will be an issue but can be only solved in operation. All necessary equipment will be installed. On the one side there are the in-vacuum movers [10] which carry the PMS and the plasma target, respectively. The relative alignment of both should be feasible due to the degrees of freedom and precision of the movers. On the other side a beam size measurement for even μm small bunches will be installed. This is realized by a knife edge scan of the tightly focused bunch [65].

The LPA experiments at REGAE will be challenging in all point of views. It begins with the correct alignment of all required components relative to the high power laser. This includes the plasma target, the PMS and of course the electron beam. Besides the transverse overlap of the laser and electron beams the temporal alignment and its control will be a crucial issue. Two independent systems, the high power laser and the REGAE linac, has to be synchronized and each system needs a high stability in terms of all relevant subsystems. All these requirements have been demonstrated to be realizable in several studies of the involved team. Almost all components are ready to be integrated at REGAE, so that the first experiments can start hopefully in the near future.

This work contributed the tools and routines to perform highly precise and reliable electron beam diagnostics for the transverse phase space of ultra low charge bunches at the REGAE linac. And furthermore a transverse beam optics has been introduced to fulfill all requirements for a successful matching into the laser-driven plasma wakefield.

List of Figures

1.1	Illustration of the injector part of the REGAE accelerator including the cavities (gun, buncher), beam optics, the diagnostic crosses (DDC1/2) and the cathode load-lock system.	4
1.2	Illustration of the current REGAE beamline including all relevant machine devices. The center positions of each device along the beamline are depicted as well. Sol: Solenoid, DC: Diagnostic Cross, DDC: Double Diagnostic Cross, D: Detector system, DaMon: Dark current Monitor.	5
1.3	Tracking different beam parameters from the cathode to the detector <i>Det:</i> a) RMS beam size, b) norm. RMS emittance, c) RMS bunch length. The horizontal direction is plotted representatively. The various beam optics relevant elements are indicated by colored blocks. Cavities are <i>red</i> , solenoids are <i>green</i> and collimators are <i>black</i> . Their width is correctly scaled to the real objects dimension.	7
1.4	Overview of the REGAE beamline adapted to the LPA experiment. Up to the buncher cavity the beamline is unchanged. Sol45 is slightly shifted upstream and Sol67 a bit further downstream. The <i>interaction chamber</i> is new and houses beside the new gas target for the LPA experiment new beam optics devices - the permanent magnetic solenoids (PMS). In addition to the conventional electrical solenoids a quadrupole doublet will be installed to cope with higher energy electrons accelerated during the LPA process. The dipole spectrometer is shifted from its original place, close behind the buncher, to the end of the LAOLA@REGAE beamline section. The in- as well as out-coupling of the high power ANGUS laser is depicted as well. (Figure by courtesy of B. Zeitler, from [10])	10

2.1	Schematic phase space ellipse and illustration of the related beam parameters and optical functions, respectively. The particle distribution is depicted by the blue dots.	22
2.2	Energy band structure of an activated crystalline scintillator. (From G. F. Knoll [44])	29
2.3	Schematic illustration of a metal-oxide-semiconductors (MOS) capacitors. N_A denotes the density of the acceptors and p the density of the holes. In the depletion layer are no holes, whereas in the bulk $N_A = p$. Figure originates from [46].	31
2.4	Illustration of plasma wakefield. components close to the longitudinal axis. The laser pulse is at $k_p \xi = 0$ but not illustrated in these plots.	34
3.1	Layout of the REGAE detector. Figure adapted from [49].	37
3.2	Quantum efficiency of an Andor iXon3 888 back-illuminated EMCCD (green curve (BV, BVF)). Figure originates from [48].	38
3.3	Left: Schematic layout of CCD chip and register transfer as well as gain/multiplication register. Right: Schematic of the iXon3 vacuum head including CCD chip and TE cooler. Figures originate from [48].	39
3.4	Left: Schematic composition of a Hamamatsu Fiber Optic Scintillator (FOS). Right: Schematic structure of a Fiber Optic Plate (FOP). Figures originate from [47].	41
3.5	Vapour-deposited column-shaped CsI(Tl) scintillation crystals of very smooth structure. Diameter $\sim 3 \mu\text{m}$, length $> 0.5 \text{ mm}$. Figure originates from [51].	42
3.6	Schematic illustration of light guiding inside a fiber optic. The acceptance angle θ_{max} is defined by the refraction indices n_1 and n_2 , which defines the critical angle θ_c of a total reflection inside a fiber. Figure originates from [52].	44
3.7	Left: Spectrum of the scintillation light of CsI(Tl) and CsI(Na). Right: Light output depending on temperature for CsI(Tl) and CsI(Na). Figures originate from [53].	44
3.8	Relation between material density and refractive index for different glass compositions. Plot is based on [54]. Figure originates from [55].	45
3.9	Stopping power of CsI. Curves base on data from [57].	47

3.10 Light optic of D1. Where $a = 150 \mu\text{m}$ is the thickness of the CsI scintillator; $b = 3 \text{ mm}$ is the thickness of FOP. s_{0-2} are the distances between the FOS, lenses and the EMCCD; $s_0 = 400 \text{ mm}$, $s_1 = 350 \text{ mm}$, $s_2 = 300 \text{ mm}$. Focal lengths f_1 and f_2 of the lenses L_1 and L_2 are identical with the distances s_0 and s_2 . The lenses' diameter is $d = 2''$. 48

3.11 Extrapolation of the ungained intensity of the signal detected by the Andor iXon3 888. The Real-Gain mode has been used and shows a linear behavior. The fit (red, solid curve) yielded: Tot. pixel count = $-39529.6 + 567419 \times \text{EM-gain}$ 50

3.12 In the **first row** are noise images (left, middle) of the Andor iXon 888 camera shown. The camera is cooled down to -70°C . The images contain all kind of noise caused by the camera itself. The right image shows the difference of the first two. The **second row** is similar to the first. Here are two real background images shown. The 'signal' is *dark current*. The right image shows again the difference of the left and middle. The remaining structure is *shot noise* caused by the dark current. In the **third row** the left plot shows an artificial normal distributed beam profile. The right plot shows the histograms of the Gaussian distribution as well as of the two difference plots of the first and second row. 53

3.13 Shown are PMFs for different pairs of λ_1 and λ_2 for $k_S \in \mathbb{Z}$. (The lines are not indicate continuity.) 55

3.14 Histogram of pixel intensity (blue dots). Red dotes were used for double Gaussian fit. The green line marks the cut-off value k_{cut} (90 %-cut). 56

3.15 **Left:** Background image from Fig. 3.12 has been added to an artificial Gaussian beam profile. **Right:** Same beam profile after applying whole post-processing routine. 58

3.16 **Left:** $C_4(q)$ (blue) plotted for whole interval $(0, 1)$ of the relative integrated noise intensity q . The minimal \mathbf{q}_{min} can be numerically determined. It is marked by the red vertical line and is approximately **0.6451**. **Right:** The optimal relative integrated noise intensity q_{opt} depending on SNR. 63

3.17 The relative RMS error (x_{RMS}/σ_x) for afew specific values of the relative intensity noise cut q depending on *signal-to-noise-ratio* (SNR). 64

3.18	Measured beam profile at REGAE - projections and 2D-colored profile. Double Gaussian fits (solid lines) has been applied.	65
3.19	Left: Measured 2D-beam profile at REGAE. Right: Same beam profile after applying an intensity cut-off. RMS calculation and Gaussian fit results in Tab. 3.5.	67
3.20	Horizontal and vertical beam profile (dots) and fitted double Gaussians (solid) at D1.	69
3.21	Backtracking of the peaked and broad Gaussian distribution from Sol67 to the collimator ($d = 1.1$ mm) at DDC2 using the fit results from Tab. 3.6. The black vertical line indicates the collimator position and its radius.	70
3.22	Beam size scan and fit of the peaked (left) and of the broad (right) Gaussian beam part.	71
3.23	Experimental setup of the FOS measurement with a β^- -source.	73
3.24	Upper: A theoretical profile of an imaged edge (solid green) and an approximation with an error-function (solid blue). In addition the derivatives of the solid lines are depicted (dashed lines). The vertical gray line marks the position of the half-height of the error-function/intensity profile and the maximal slope of the error-function. The red dashed line indicates the ramp's width rt . Lower Row: The left plot shows the 2D profile taken in the laboratory using the ^{137}Cs source. The right plot shows the integrated profile (solid blue) and a fit using the introduced model (dashed red). The intensity profile is obtained by averaging over 10 pixel columns of the left profile.	75
3.25	Left: Beam profile of a 30 s exposed FOS to a ^{90}Y β^- -source. Right: Horizontal and vertical beam projections (dots) fitted with a double Gaussian (solid/dashed lines).	77
3.26	Schematic of energy transfer and deposition for an EGS simulated FOS screen. The scattering process at the different layers is divided in three segments (I-III).	78
3.27	Relative energy absorption of CsI ($d = 150$ μm) as function of the incident energy E_{kin} . Simulated with EGS5 and calculated with the stopping power $P(E_{\text{kin}})$ (Eq. 3.1).	80

3.28	Energy spectrum of β^- -emitter ^{90}Y . E_{kin} is equivalent to T in Eq. 3.28.	83
3.29	Left: Energy spectrum of electrons leaving the CsI layer. Pertaining to Fig. 3.26 the integral of this spectrum is equivalent to $E_{out,I}$. Right: Energy spectrum of back scattered electrons from FOP. The integral of this spectrum is equivalent to $E_{ref,II}$. Both: 'Counts' is an arbitrary relative unit and has only a qualitative character for each plot.	84
3.30	Total transmitted electron energy in forward direction (solid, blue) depending on incident electron energy $E_{kin,in}$ for a 150 μm thick CsI scintillator. As well the original total energy distribution of ^{90}Y (red, dashed) is shown.	85
3.31	Accumulated transverse profile of ^{90}Y β^- -source after passing the CsI layer ($d = 150 \mu\text{m}$).	85
3.32	Energy spectrum of the forward moving electrons (left) as well as photons (right). $E_{kin,in} = 2.5 \text{ MeV}$	86
3.33	Upper, left: Beam profile of back scattered electrons from FOP. Upper, right: Beam projections horizontal and vertical are shown and had been fitted with a double Gaussian function. The pixel size is 50 μm and the fitted standard deviations of the profiles are equal in both directions. $\sigma_{x,1} = 0.03 \text{ mm}$ and $\sigma_{x,2} = 1.2 \text{ mm}$. Lower: Energy spectrum of back scattered electrons from FOP.	89
3.34	Upper Row: On the left hand side the comparison of a scattered (at all layers of the FOS) and unscattered (or incident) Gaussian REGAE beam profile. The original beam size (unscattered beam) is $\sigma = 71.9 \mu\text{m}$. Due to the scattering the distinct halo is visible. On the right hand side a fit with a double Gaussian function of the same scattered beam profile is shown. Lower: Scattered beam profile from EGS simulation compared with a measured profile at REGAE.	90
4.1	CST simulation of two radially magnetized rings (blue) and the conceptual wedge-based design. The relevant dimensions of the PMS are illustrated.	95
4.2	Current loops model of a flawed wedge with a tilted magnetization.	97

4.3	Deviation of the second field integral F_{2,N_L} from $F_{2,300}$ depending on the number of current loops N_L per wedge.	99
4.4	Upper: Convergence of the normalized field quality $\hat{\chi}$ depending on the step width δz along a magnetic field line for various arbitrarily chosen PMS assemblies. Lower: Convergence of the normalized field quality difference $\Delta(\hat{\chi}_i - \hat{\chi}_1)$ with respect to a certain PMS assembly depending on the step width δz along a magnetic field line. Shown are two different magnifications.	101
4.5	Convergence of the normalized field quality $\hat{\chi}$ depending on the number of magnetic field lines for various arbitrarily chosen PMS assemblies. Shown are two different magnifications.	102
4.6	Left: Growth of normalized 4D emittance for different PMS assemblies. The PMS's center is placed at $z = 5.33$ m. Right: Correlation between the field quality χ used for the numerical sorting algorithm and the normalized 4D emittance tracked with ASTRA.	103
4.7	Left: 3D-Hall probe calibration of the absolute magnetic field measurement versus a NMR Teslameter measurement. The red dashed line shows the linear regression of the taken data. Right: Relative magnetic field measurement accuracy depending on the absolute magnetic field. The relative accuracy has been determined from 100 data points per adjusted magnetic field.	104
4.8	Upper: Measured and simulated on-axis longitudinal magnetic field $B_{z,0}(z)$. Lower: Field difference of measured and simulated field (solid blue) and relative field deviation (dashed red) of the measured field with respect to the simulated field.	108
4.9	Measured and simulated off-axis ($y = 0$, $x = 1$ mm) transverse magnetic field $B_{y,1}(z)$	109

4.10	Illustration of the adiabatic injection of an electron bunch into a laser-driven plasma. The longitudinal axis is inverted. Positive z values direct upstream of the beamline. In addition to the plasma density (green) and the laser envelope (gray) two differently yielded beta functions are plotted. The analytical solution (dash-dotted red) diverges due to numerical issues. The tracked solution does not have these issues and illustrates the correct beam envelope. Furthermore the transverse beam emittance (dotted blue) has been tracked and stays constant.	113
4.11	β and α function depending on PMS position. The required $\beta = 11.7$ mm and $\alpha = 1.94$ values are marked with a cross. The PMS position is given with respect to the beginning of the plasma up-ramp in Fig. 4.10 ($z_{\text{in}} = 5.519$).	114
4.12	The full start-to-injection simulation is shown. The left column shows the hor. RMS beam size x_{RMS} , the hor. norm. emittance $\epsilon_{n,x}$ and the bunch length z_{RMS} from the cathode to the injection point. The right column shows the same quantities but zoomed into the injection point ($z_{\text{in}} = 5.519$ m). The PMS is placed at $z_{\text{PMS}} = 5.352$ m.	117
4.13	Comparison of the 4D normalized emittance (solid blue) and the squared 2D normalized emittance (dotted red) inside the PMS and around the focus position. The influence on the 2D emittance due to the PMS is clearly visible. The PMS is centered at $z = 5.352$ m.	118
4.14	Tracked β_x with ASTRA (dashed blue) and the analytically determined matched $\beta_{x,m}$ (solid red) at the injection point. Here the injection point is $z_{\text{in}} = 0$	118
5.1	Measured beam size at D1 detector in dependence on the maximum magnetic field $B_{z,\text{max}}$ of solenoid Sol67. Solid lines represent least-square fits which have been done with the introduced method in Sec. 2.1.4. The 2D-beam profile of each data point is depicted in the background.	121

5.2	Minimal RMS beam size $x_{\text{RMS},\text{min}}$ depending on the initial beam size $x_{0,\text{rms}}$ and the beam emittance ϵ_n at position of the D1 detector system. The exit of Sol67 has been chosen as the initial beam position. The drift distance l_D is equal to 3.52 m. In addition the red dot-dashed line marks the spatial resolution of the D1 detector system ($\sim 16 \mu\text{m}$).	123
5.3	The normalized transverse emittance in dependence on the collimator diameter d . The different bunch charges are labeled in the plot legend.	125
5.4	Left: Shown is the mean beam energy E_{kin} depending on the gun gradient Amp_{Gun} . Above 30 MV/m the dependency is in good approximation linear. Right: The output mean beam energy E_{kin} depending on the gun phase ϕ_{Gun} . The phase of maximum energy gain depends on the gradient. Here, the gun gradient is 70 MV/m and a maximum mean beam energy of 3.19 MeV can be achieved.	127
5.5	Buncher phase scan to determine the correct phase and to gain the measured average kin. energy of $E_{\text{kin}} = 2.45 \text{ MeV}$. The red cross marks the right phase.	130
5.6	Remaining charge $Q_{\text{collimator}}$ after the collimator ($d_{\text{Coll}} = 1.1 \text{ mm}$) depending on laser intensity or respectively the generated charge Q_{cathode} at position of the cathode. The red cross marks the right charge at the cathode. This value is needed for the ASTRA simulation. The negative sign of $Q_{\text{collimator}}$ is caused by the species (electrons) which has been used for the ASTRA simulation and is not relevant.	130
5.7	Tracking from the cesium-telluride through the collimator ($d = 1.1 \text{ mm}$): a) RMS beam size, b) norm. RMS emittance, c) RMS bunch length. The horizontal direction is plotted representatively. The various beam optics relevant elements are indicated by colored blocks. Cavities are <i>red</i> , solenoids are <i>green</i> and collimators are <i>black</i> . Their width is correctly scaled to the real objects dimension.	132
5.8	Tracking the kinetic energy E_{kin} from the collimator to solenoid Sol67. The various beam optics relevant elements are indicated by colored blocks. Cavities are <i>red</i> , solenoids are <i>green</i> and collimators are <i>black</i> . Their width is correctly scaled to the real objects.	133

-
- 5.9 Tracking from the collimator to solenoid Sol67: **a)** RMS beam size, **b)** norm. RMS emittance, **c)** RMS bunch length. The horizontal direction is plotted representatively. The various beam optics relevant elements are indicated by colored blocks. Cavities are *red*, solenoids are *green* and collimators are *black*. Their width is correctly scaled to the real objects. 134
- 5.10 Emittance scan at D1 detector with solenoid Sol67. Comparison between simulations (green/orange line) and measurement (red and blue dots). In addition the fitted model is plotted (solid/dashed lines). 135
- 5.11 Initial phase space distribution of simulated electron bunch at position of Sol67 (green distribution). The distribution is extracted from a start-to-end ASTRA simulation. it corresponds to the emittance scan, labeled **ASTRA Run I**, showed in Fig. 5.10. The second, overlaid distribution (orange) is a modified version of the green distribution. It is modified in a way that the best agreement with the measurement has been achieved. In Fig. 5.10 it is called **ASTRA Run II**. 138
- 5.12 **Left:** Normalized horizontal emittance depending on the different solenoid settings of Sol67. The red line marks the average normalized emittance of $25.2(3) \pi \mu\text{m mrad}$. **Right:** Compares the uncorrelated and normalized phase space of the electron distribution at the minimal beam size (yellow dots) and the last data point (blue dots) of the scan. The correlation $\langle xx' \rangle$ of the horizontal position x and the horizontal divergence x' has been subtracted. Furthermore the distributions has been normalized in both directions of the phase space to their corresponding RMS values. Corresponding to the emittance difference shown in the left plot, the occupied area of the 'blue' distribution is larger. Moreover the 'blue' distribution has a distinct curvature noticeable by the additional 'wings' which illustrates the non-linearities imprinted on the distribution. The 'yellow' distribution does not have these features. 139
- 5.13 Long-term emittance measurements at REGAE over a period of 14 months. 140

5.14 Emittance measurements at REGAE illustrated in dependence on the kinetic energy and the bunch charge. The emittance is indicated by a color code.	142
--	-----

List of Tables

1.1	Relevant design parameters for the REGAE accelerator including machine, laser and electron beam parameters. All parameters are extracted from the REGAE <i>design run</i> . The laser parameters are given at the photo cathode. The electron beam parameters are given at the target position at $z = 5.5$ m.	8
3.1	Characteristics of Andor iXon3 885/888 EMCCD cameras. Data originates from [48].	40
3.3	Properties of the FOP contained in the FOS used at REGAE. The refractive indices n_1 and n_2 are defined like in Fig. 3.6. P.F. means 'packing fraction'. Data originates from [47].	42
3.2	Comparison of NaI(Tl) and CsI(Tl). Data originates from [44].	43
3.4	Theoretical and post-processed barycenter (1 st moment) and RMS (2 nd central moment) of a Gaussian beam profile (Fig. 3.15). The moments are given in pixel.	58
3.5	RMS beam size evaluations of a post-processed typical beam image (Fig. 3.19). The left plot shows the average of 10 beam signal images and 10 subtracted background images. Three different methods are used to evaluate the RMS. 1. A double Gaussian fit has been applied to the beam projections. $\{\sigma_1, \sigma_2\}$ are listed. The beam signal is represented by σ_1 . 2. The RMS of the whole image has been calculated. 3. From the Gaussian fit in 1. the integrated intensity I_{cut} of the halo has been used to apply a cut. The resulting beam profile is shown in the right plot.	67
3.6	Emittance fit results of the peaked (upper) and the broad (lower) profile part.	72
3.7	¹³⁷ Cs decay including all subsequent decays. Strongly unlike decay channels are ignored. Data received from DESY's radiation safety group D3.	74

3.8	Characteristics of the β -decay of ^{90}Sr and ^{90}Y . Data received from DESY's radiation safety group D3.	76
3.9	Constants required for Fermi's golden rule of ^{90}Y β -decay.	82
3.10	Energy transmission and deposition of a ^{90}Y β^- -spectrum passing a FOS screen.	83
3.11	Energy balance of a REGAE-like electron beam of 2.5 MeV hitting the FOS scintillation screen. Chronological relative energy loss/transmission of the two layers CsI and FOP. Photon production and energy deposition is neglected.	87
3.12	Comparison of the simulated transverse profile with EGS and a measured beam profile at REGAE. The profiles are shown in Fig. 3.34. Listed are results from a fit of the profiles. The double Gaussian function of Eq. 3.24 has been used. Besides the amplitudes a_1 , a_2 and the standard deviations σ_1 , σ_2 the integrated intensities I_1 , I_2 and their ratio I_2/I_1 are listed.	88
4.1	Comparing fit results for both PMS assemblies as well as for the ideal solenoid model with flawless wedges.	107
4.2	Relevant design parameters for the external injection experiment at REGAE. Table originates from [10], only the electron beam parameters has been adapted.	110
4.3	Electron beam parameters at injection point $z_{\text{in}} = 5.519\text{m}$	115
5.1	Least-square fit parameters and uncertainties of a solenoid scan at REGAE.	122

5.2 Machine and ASTRA setup for the presented emittance measurement. Listed are the required machine devices to set up a ASTRA simulation. Beside the solenoid settings the measured cavity amplitudes (Gun and Bun), charge (DaMon) and energy are depicted. The energy has been determined by use of the dipole spectrometer. Therefore the energy has been yielded after passing both cavities. The contribution of each cavity depends on the adjusted phases. For the solenoids it is necessary to convert the currents to the maximum longitudinal magnetic field $B_{z,max}$. Due to the usage of the first collimator *Coll1* the bunch charge measured at *DaMon* is not the charge at the cathode which is required for the ASTRA simulation. Hence, scans for the buncher phase as well as charge at position of the cathode needs to be done and are presented in Fig. 5.5 and Fig. 5.6. The laser beam parameters ($x_{RMS,l}$, $y_{RMS,l}$ and $t_{RMS,l}$) had been measured recently and can be directly put into the ASTRA simulation. 129

5.3 Comparison of the achieved simulated beam parameters on the one side and the determined parameters from the measurement on the other side. The normalized emittance of the ASTRA simulation corresponds to the depicted average emittance in Fig. 5.12, left. Respectively the horizontal as well as vertical results measured at REGAE are presented. 136

5.4 Comparison of the modified ASTRA beam parameters on the one side and the measured parameters from REGAE on the other side. In contrast to Tab. 5.3 the initial distribution (Fig. 5.11, green) has been modified (orange) to reproduce the measured results (Fig. 5.10).137

Bibliography

- [1] T. Tajima and J. M. Dawson. Design considerations for table-top, laser-based VUV and X-ray free electron lasers. *Phys. Rev. Lett.*, 43(267):267–270, February 1979.
- [2] Satomi Shiraishi. *Investigation of Staged Laser-Plasma Acceleration*. Dissertation, University Chicago, Chicago, USA, 2015.
- [3] D. Panasenko, A. J. Shu, C. B. Schroeder, A. J. Gonsalves, K. Nakamura, N. H. Matlis, E. Cormier-Michel, G. Plateau, C. Lin, C. Toth, C. G. R. Geddes, E. Esarey, and W. P. Leemans. Staging laser plasma accelerators for increased beam energy. In *Proceedings, 13th Advanced Accelerator Concepts Workshop*, Santa Cruz, USA, 2008.
- [4] F. Grüner, S. Becker, U. Schramm, T. Eichner, M. Fuchs, R. Weingartner, D. Habs, J. Meyer ter Vehn, M. Geissler, M. Ferrario, L. Serafini, B. van der Geer, H. Backe, W. Lauth, and S. Reiche. Design considerations for table-top, laser-based VUV and X-ray free electron lasers. *Applied Physics B*, 86:431–435, February 2007.
- [5] Benno Zeitler, Irene Dornmair, Tim Gehrke, Mikheil Titberidze, Andreas R. Maier, Bernhard Hidding, Klaus Flöttmann, and Florian Grüner. Merging conventional and laser wakefield accelerators. In *Proc. SPIE*, volume 8779, 2013.
- [6] Julia Grebenyuk, Timon Mehrling, Frank S. Tsung, Klaus Flöttman, and Jens Osterhoff. Simulations of laser-wakefield acceleration with external electron-bunch injection for REGAE experiments at DESY. In *AIP Conference Proceedings*, volume 1507, page 688, December 2012.
- [7] S. P. D. Mangles, C. D. Murphy, Z. Najmudin, A. G. R. Thomas, J. L. Collier, A. E. Dangor, E. J. Divall, P. S. Foster, J. G. Gallacher, C. J. Hooker, D. A. Jaroszynski, A. J. Langley, W. B. Mori, P. A. Norreys, F. S. Tsung,

- R. Viskup, B. R. Walton, and K. Krushelnick. Monoenergetic beams of relativistic electrons from intense laser-plasma interactions. *Nature*, 431:535–538, September 2004.
- [8] C. G. R. Geddes, C. S. Toth, J. van Tilborg, E. Esarey, C. B. Schroeder, D. Bruhwiler, C. Nieter, J. Cary, and W. P. Leemans. High-quality electron beams from a laser wakefield accelerator using plasma-channel guiding. *Nature*, 431:538–541, September 2004.
- [9] J. Faure, Y. Glinec, A. Pukhov, S. Kiselev, S. Gordienko, E. Lefebvre, J.-P. Rousseau, F. Burgy, and V. Malka. A laser-plasma accelerator producing monoenergetic electron beams. *Nature*, 431:541–544, September 2004.
- [10] Benno Zeitler. *Phase Space Linearization and External Injection of Electron Bunches into Laser-Driven Plasma Wakefields at REGAE*. Dissertation, Universität Hamburg, Hamburg, Germany, 2016.
- [11] I. Dornmair, C. B. Schroeder, K. Flöttmann, B. Marchetti, and A. R. Maier. Plasma-driven ultrashort bunch diagnostics. *Phys. Rev. Accel. Beams*, 19(062801), June 2016.
- [12] Klaus Flöttmann and Valentin V. Paramonov. Beam dynamics in transverse deflecting RF structures. *Phys. Rev. ST Accel. Beams*, 17(024001), February 2014.
- [13] Benno Zeitler, Klaus Flöttmann, and Florian Grüner. Linearization of the longitudinal phase space without higher harmonic field. *Phys. Rev. ST Accel. Beams*, 18(120102), December 2015.
- [14] Frank Mayet. Simulation and characterization of the RF system and global stability analysis at the REGAE linear electron accelerator. Master’s thesis, Universität Hamburg, Hamburg, Germany, 2013.
- [15] M. Hoffmann, H. Kay, U. Mavric, H. Schlarb, C. Schmidt, W. Jalmuzna, T. Kozak, and A. Piotrowski. Precision LLRF controls for the S-band accelerator REGAE. In *Proceedings, 4th International Particle Accelerator Conference*, Shanghai, China, 2013.
- [16] Klaus Flöttmann. Design and performance of printed circuit steering magnets for the flash injector. In *IPAC’10*, Kyoto, Japan, 2010.

- [17] Shima Bayesteh. *Transverse electron beam diagnostics at REGAE*. Dissertation, Universität Hamburg, Hamburg, Germany, 2014.
- [18] Shima Bayesteh, Hossein Delsim-Hashemi, and Klaus Flöttmann. Beam profile monitors at REGAE. In *Proceedings, 2nd International Beam Instrumentation Conference*, Oxford, UK, 2013.
- [19] Shima Bayesteh and Hossein Delsim-Hashemi. Diagnostics of femtosecond low-charge electron bunches at REGAE. In *Proceedings of IPAC'11*, San Sebastián, Spain, 2011.
- [20] Hossein Delsim-Hashemi, Klaus Flöttmann, Michael Seebach, and Shima Bayesteh. Charge monitors at the relativistic electron gun for atomic exploration - REGAE. In *Proceedings, 2nd International Beam Instrumentation Conference*, Oxford, UK, 2013.
- [21] D. Lipka, J. Lund-Nielsen, and Michael Seebach. Resonator for charge measurement at REGAE. In *Proceedings, 2nd International Beam Instrumentation Conference*, Oxford, UK, 2013.
- [22] Jason R. Dwyer, Christoph T. Hebeisen, Ralph Ernstorf, Maher Harb, Vatche B. Deyirmenjian, Robert E. Jordan, and R. J Dwayne Miller. Femtosecond electron diffraction: 'making the molecular movie'. *Philosophical Transactions of the royal society A*, 364:741–778, January 2006.
- [23] Stephanie Manz, Albert Casandruc, Dongfang Zhang, Yinpeng Zhong, Rolf A. Loch, Alexander Marx, Taisuke Hasegawa, Lai Chung Liu, Shima Bayesteh, Hossein Delsim-Hashemi, Matthias Hoffmann, Matthias Felber, Max Hachmann, Frank Mayet, Julian Hirscht, Sercan Keskin, Masaki Hada, Sascha W. Epp, Klaus Flöttmann, and R.J. Dwayne Miller. Mapping atomic motions with ultrabright electrons: Towards fundamental limits in space-time resolution. *Faraday Discuss.*, 177:476–491, January 2015.
- [24] Julian Hirscht. *Femtosecond Electron Diffraction: Next generation electron sources for atomically resolved dynamics*. Dissertation, Universität Hamburg, Hamburg, Germany, 2015.

- [25] Irene Dornmair. *Advanced Beam Dynamics and Diagnostics Concepts for Laser-Plasma Accelerators*. Dissertation, Universität Hamburg, Hamburg, Germany, 2016.
- [26] Klaus Flöttmann. ASTRA - a space charge tracking algorithm. <http://www.desy.de/~mpyf1o/>, March 2017. [Online; accessed July 07, 2017].
- [27] Klaus Flöttmann. Generation of sub-fs electron beams at few-MeV energies. *Nuclear Instruments and Methods in Physics Research A: Accelerators, Spectrometers, Detectors and Associated Equipment*, 740:34–38, March 2014.
- [28] Tim Gehrke. Design of permanent magnetic solenoids for REGAE. Master's thesis, Universität Hamburg, Hamburg, Germany, 2013.
- [29] Mikheil Titberidze. *Pilot Study of Synchronization on a Femtosecond Scale between the Electron Gun REGAE and a Laser-Plasma Accelerator*. Dissertation, Universität Hamburg, Hamburg, Germany, 2016.
- [30] J. Buon. Beam phase space and emittance. In S. Turner, editor, *CERN accelerator school*, volume 91-04. CERN, 1990.
- [31] Klaus Flöttmann. Some basic features of the beam emittance. *Phys. Rev. ST Accel. Beams*, 6(034202), March 2003.
- [32] Joseph Liouville. Sur la théorie des équations transcendentes. *Journal de Mathématiques Pures et Appliquées*, 3:337–354, 1838.
- [33] J. Rossbach and P. Schmüser. Basic course on accelerator optics. In *CAS - CERN Accelerator School : 5th General Accelerator Physics Course*, volume CERN-94-01, pages 17–88, 1992.
- [34] F. Willeke and G. Ripken. Methods of beam optics. In *US Particle Accelerator School*, New York, USA, 1988.
- [35] Max Hachmann. Transverse emittance measurement at REGAE via a solenoid scan. Diploma thesis, Universität Hamburg, Hamburg, Germany, 2013.
- [36] Klaus Flöttmann. Beam dynamics in RF guns and injectors. Draft Version 25.01.2011, January 2011.

- [37] E. D. Courant and H. S. Snyder. Theory of the alternating-gradient synchrotron. *Annals of Physics*, 3:1–48, 1958.
- [38] Simon Jolly. Focusing properties of a solenoid magnet. UK Neutrino Factory R&D at Imperial College meeting, May 2005.
- [39] John Rees and Lenny Rivkin. On measuring emittances and sigma matrices. *SLAC-PUB-3305*, March 1984.
- [40] M.G. Minty and F. Zimmermann. *Measurements and Control of Charged Particle Beams*. Springer-Verlag Berlin Heidelberg New York, 2003.
- [41] Carl Friedrich Gauss. *Methode der kleinsten Quadrate*. P. Stankiewicz’ Buchdruckerei, Berlin, 1887.
- [42] Philip R. Bevington. *Data reduction and error analysis for the physical sciences*. McGraw-Hill book company, 1969.
- [43] Frank J. Sacherer. RMS envelope equations with space charge. In *4th IEEE Particle Accelerator Conference, Chicago, IL, USA, 1-3 Mar 1971*, pages 1105–1107, 1970.
- [44] Glenn F. Knoll. *Radiation Detection and Measurement*. John Wiley & Sons, 4 edition, 2010.
- [45] W. S. Boyle and G. E. Smith. Charge coupled semiconductor devices. *Bell Labs Technical Journal*, 49:587–593, April 1970.
- [46] User:Brews ohare. Metal-oxide-semiconductor structure on p-type silicon. https://en.wikipedia.org/wiki/MOSFET#/media/File:MOS_Capacitor.svg, February 2010. [Online; accessed July 07, 2017].
- [47] Hamamatsu Photonics K.K. Fiber Optical Scintillator j6677 (FOS). <http://www.hamamatsu.com/jp/en/J6677.html>, July 2016. [Online; accessed July 07, 2017].
- [48] Andor Technology Ltd. iXon EMCCD cameras. <http://www.andor.com/cameras/ixon-emccd-camera-series>, 2017. [Online; accessed July 07, 2017].

- [49] Hossein Delsim-Hashemi. Single shot transversal profile monitoring of ultra low charge relativistic electron bunches at REGAE. In *Proceedings, 5th International Beam Instrumentation Conference*, Barcelona, Spain, 2016.
- [50] Donal J. Denvir and Emer Conroy. Electron-multiplying ccd: the new iccd. In *Proc. SPIE*, volume 4796, 2003.
- [51] Michael Overdick. Detectors for X-ray imaging and computed tomography - advances and key technologies. In Gerhard Spekowius and Thomas Wendler, editors, *Advances in Healthcare Technology - Shaping the Future of Medical Care*, volume 6, chapter 4. Springer, 2006.
- [52] User:User A1. A multi-mode fiber of index n_1 with cladding of index n_2 . https://en.wikipedia.org/wiki/Numerical_aperture#/media/File:Optic_fibre-numerical_aperture_diagram.svg, December 2007. [Online; accessed July 07, 2017].
- [53] Saint-Gobain Crystals. CsI(Tl) Thallium activated Cesium Iodide. <http://www.crystals.saint-gobain.com/products/csitl-cesium-iodide-thallium>, 2016. [Online; accessed July 07, 2017].
- [54] Alexander Flügel. Global model for calculating room-temperature glass density from the composition. *Journal of the American Ceramic Society*, 90(8):2622–2625, August 2007.
- [55] Alexander Flügel. Relation between density and refractive index, silicate and borosilicate glasses. http://glassproperties.com/refractive_index/density-nd.GIF, 2017. [Online; accessed July 07, 2017].
- [56] R. Gwin and R. B. Murray. Scintillation process in CsI(Tl). I. Comparison with activator saturation model. *Phys. Rev.*, 131(2):501, July 1963.
- [57] NIST National Institute of Standards and Technology. ESTAR: stopping-power and range tables for electrons. <http://physics.nist.gov/PhysRefData/Star/Text/ESTAR.html>, 2017. [Online; accessed July 07, 2017].
- [58] W. Schottky. Über spontane Stromschwankungen in verschiedenen Elektrizitätsleitern. *Annalen der Physik*, 361, Issue 23:541–567, 1918.

-
- [59] J. G. Skellam. The frequency distribution of the difference between two poisson variates belonging to different populations. *Journal of the Royal Statistical Society Series A*, 109(3):296, March 1946.
- [60] Youngbae Hwang, Jun-Sik Kim, and In So Kweon. Difference-based image noise modeling using skellam distribution. *IEEE Transactions on Pattern Analysis and Machine Intelligence*, 34, July 2012.
- [61] Florian Löhl. Measurements of the transverse emittance at the VUV-FEL. Diploma thesis, Universität Hamburg, 2005.
- [62] Michele Comunian. *Emittance Measurements in Compact Linear Collider Test Facility*. Draft version of the phd thesis, Università degli studi di Padova, 1994.
- [63] H. Hirayama, Y. Namito, A. F. Bielajew, S. J. Wilderman, and W. R. Nelson. The EGS5 code system. <http://rcwww.kek.jp/research/egs/egs5.html>, January 2016. [Online; accessed July 07, 2017].
- [64] Enrico Fermi. *Nuclear Physics*. Midway Reprint, 1950.
- [65] Konstantin Krausert. Development of measurement methods for transverse beam profiles in the micrometer range at the REGAE beamline. Master's thesis, Universität Hamburg, Hamburg, Germany, 2015.
- [66] S. Agostinelli and et al. GEANT4 - a simulation toolkit. *Nuclear Instruments and Methods in Physics Research A: Accelerators, Spectrometers, Detectors and Associated Equipment*, 506:250–303, July 2003.
- [67] S. Agostinelli and et al. GEANT4 - a simulation toolkit. <http://geant4.cern.ch/>, June 2017. [Online; accessed July 07, 2017].
- [68] G. Rakowsky. A simple model-based magnet sorting algorithm for planar hybrid undulators. In *IPAC'10*, Kyoto, Japan, 2010.
- [69] T. C. Fan, C. S. Hwang, C. H. Chang, Ch. Wang, and J. R. Chen. Magnet sorting algorithms for the SRRC EPU5.6. In *European Particle Accelerator Conference*, Bristol, UK, 1998.

- [70] Max Hachmann, Klaus Flöttmann, Frank Mayet, and Tim Gehrke. Design and characterization of permanent magnetic solenoids for REGAE. In *Proceedings, 6th International Particle Accelerator Conference*, Richmond, USA, 2015.
- [71] Max Hachmann, Klaus Flöttman, Tim Gehrke, and Frank Mayet. Design and characterization of permanent magnetic solenoids for REGAE. *Nuclear Instruments and Methods in Physics Research A: Accelerators, Spectrometers, Detectors and Associated Equipment*, 829:270–273, September 2016.
- [72] Peter Campbell. *Permanent Magnet Materials and Their Application*. Cambridge University Press, 1994.
- [73] Computer Simulation Technology GmbH. CST - Computer Simulation Technology. <https://www.cst.com/>, 2018. [Online; accessed January 15, 2018].
- [74] S. Kirkpatrick, C. D. Gelatt, and M. P. Vecchi. Optimization by simulated annealing. *Science*, 220(4598):671–680, May 1983.
- [75] B. Faatz and J. Pflueger. Magnet Sorting for the TTF-FEL Undulator using Simulated Annealing. TESLA FEL Report, 1999-01.
- [76] Metrolab Technology SA. Three-axis Magnetometers THM1176 and TFM1186: User’s manual. <http://www.metrolab.com/products/thm1176/>, October 2016. [Online; accessed July 07, 2017].
- [77] Metrolab Technology SA. PT 2025 - NMR Teslameter: User’s manual. <http://www.metrolab.com/products/pt2025/>, September 2003. [Online; accessed July 07, 2017].
- [78] T. Mehrling, J. Grebenyuk, K. Flöttmann F. S. Tsung, and J. Osterhoff. Transverse emittance growth in staged laser-wakefield acceleration. *Phys. Rev. ST Accel. Beams*, 15(111303), November 2012.
- [79] Klaus Flöttmann. Adiabatic matching section for plasma accelerated beams. *Phys. Rev. ST Accel. Beams*, 17(054402), May 2014.
- [80] I. Dornmair, K. Floettmann, and A. R. Maier. Emittance conservation by tailored focusing profiles in a plasma accelerator. *Phys. Rev. ST Accel. Beams*, 18(041302), April 2015.

- [81] M. Migliorati, A. Bacci, C. Benedetti, E. Chiadroni, M. Ferrario, A. Mostacci, L. Palumbo, A. R. Rossi, L. Serafini, and P. Antici. Intrinsic normalized emittance growth in laser-driven electron accelerators. *Phys. Rev. ST Accel. Beams*, 16(011302), January 2013.
- [82] Max Hachmann and Klaus Flöttmann. Transverse emittance measurement at REGAE. In *Proceedings, 6th International Particle Accelerator Conference*, Richmond, USA, 2015.
- [83] Max Hachmann and Klaus Flöttmann. Measurement of ultra low transverse emittance at REGAE. *Nuclear Instruments and Methods in Physics Research A: Accelerators, Spectrometers, Detectors and Associated Equipment*, 829:318–320, September 2016.
- [84] Shima Bayesteh, Hossein Delsim-Hashemi, and Klaus Flöttmann. Transverse emittance measurement at REGAE. In *Proceedings, 5th International Particle Accelerator Conference*, Dresden, Germany, 2014.
- [85] O. R. Sander, G. N. Minerbo, R. A. Jameson, and D. D. Chamberlin. Beam tomography in two and four dimensions. In *Proceedings, Linear Accelerator Conference*, New York, USA, 1979.
- [86] G. Asova, S. Khodyachykh, M. Krasilnikov, F. Stephan, K. Floettmann, D. J. Holder, and B. Muratori. Design considerations for phase space tomography diagnostics at the pitz facility. In *Proceedings, 8th European Workshop on Beam Diagnostics and Instrumentation for Particle Accelerators*, Venice, Italy, 2007.
- [87] Christopher M. S. Sears, Alexander Buck, Karl Schmid, Julia Mikhailova, Ferenc Krausz, and Laszlo Veisz. Emittance and divergence of laser wakefield accelerated electrons. *Phys. Rev. ST Accel. Beams*, 13(092803), September 2010.
- [88] Min Zhang. Emittance formula for slits and pepper-pot measurement. FERMILAB-TM-1988, Fermi National Accelerator Laboratory, 1988.
- [89] Eduard Prat and Masamitsu Aiba. Ultralow emittance electron beams from a laser-wakefield accelerator. *Phys. Rev. ST Accel. Beams*, 17(032801), March 2014.

- [90] R. Weingartner, S. Raith, A. Popp, S. Chou, J. Wenz, K. Khrennikov, M. Heigoldt, A. R. Maier, N. Kajumba, M. Fuchs, B. Zeitler, F. Krausz, S. Karsch, and F. Grüner. Ultralow emittance electron beams from a laser-wakefield accelerator. *Phys. Rev. ST Accel. Beams*, 15(111302), November 2012.

Acknowledgments

I'd like to thank various people who supported this work and contributed to it.

First of all I'd like to thank **Dr. Ralph Aßmann** who gave me the opportunity to successfully continue my work at the REGAE project as part of my Ph.D. thesis and beyond the work of my diploma thesis. But as well I'd like to thank him for his supervision during my Ph.D.

As well I want to thank **Prof. Dr. Dwayne Miller** and **Prof. Dr. Florian Grüner** for their support during the last month of my work.

Many thanks I owe **Dr. Klaus Flöttmann** for his continuous support and advice. For the uncountable questions I've asked and he always could answer and his unshakeable positive attitude.

Furthermore there are all the people who realized and kept REGAE running, I'd like to thank. **Dr. Hossein Delsim-Hashemi** for his support regarding the detector system and all other systems which tended to stick from time to time. **Dongfang, Rolf** and **Yinpeng** who took care of the laser over the years. **Stephanie** as a fellow operator who shared all the suffering from machine downtimes and malfunctions. And of course all the people from the various DESY groups like **Matthias Hoffmann** (MSK), **Andreas Labudda** (MCS), **Yorck Holler** and **Jörg Ludwig** (MEA; for their help during the field measurements of the PMS), **Stefan Weisse** (ZEU) who supported REGAE and helped to fix various problems.

There are some colleagues I'd like to thank for their fruitful discussion and conversations sometimes REGAE related but not always: **Frank Mayet, Mikheil Titberidze, Benno Zeitler, Irene Dornmair, Paul Winkler, Jun Zhu** and **Ulrich Dorda**.

And last but definitely not least I'd like to thank my friends and family. **Marvin, Eike, Holger, Kathi, JP, Andreas, Fabian**...some of you shared the same fate but all of you always supported me during this period of my life and I really appreciate your good company. Finally and ultimately I'd like to thank my parents, my sister and the rest of my incredible family for their ceaseless believe in me. **Thank you, everyone!**

Eidesstattliche Versicherung

Hiermit versichere ich an Eides statt, die vorliegende Dissertationsschrift selbst verfasst und keine anderen als die angegebenen Hilfsmittel und Quellen benutzt zu haben.

Die eingereichte schriftliche Fassung entspricht der auf dem elektronischen Speichermedium.

Die Dissertation wurde in der vorgelegten oder einer ähnlichen Form nicht schon einmal in einem früheren Promotionsverfahren angenommen oder als ungenügend beurteilt.

Hamburg, den 10. Juli 2017

Max Hachmann